Title
Tunable RF Front-End Circuits for Advanced Communication Systems /

Permalink
https://escholarship.org/uc/item/1h9253jh

Author
Ko, Chih-Hsiang

Publication Date
2014

Peer reviewed|Thesis/dissertation

UNIVERSITY OF CALIFORNIA, SAN DIEGO

Tunable RF Front-End Circuits for Advanced Communication Systems

A dissertation submitted in partial satisfaction of the
requirements for the degree
Doctor of Philosophy

in

Electrical Engineering
(Electronic Circuits and Systems)

by

Chih-Hsiang Ko

Committee in charge:

Professor Gabriel M. Rebeiz, Chair
Professor James F. Buckwalter
Professor Gert Cauwenberghs
Professor Brian G. Keating
Professor Daniel F. Sievenpiper

2014

The dissertation of Chih-Hsiang Ko is approved, and it is acceptable in quality and form for publication on microfilm and electronically:

Chair

University of California, San Diego

2014

DEDICATION

To my family and all my friends.

TABLE OF CONTENTS

LIST OF FIGURES

LIST OF TABLES

ACKNOWLEDGEMENTS

This dissertation would not have been possible without the help and support of many people. First, I would like to thank my advisor, Prof. Gabriel Rebeiz for his guidance on my doctorial studies and researches in UCSD. Joining his research group is really an important point through my career. Among these years, I've learnt a lot from him not only on technical aspects but also the way of thinking to solve problems and the attitude to deal with different situations. He is very demanding and always asks to do our best in everything. However, this kind of attitude made me improve much more than I can image and help me to be successful in the future. He extremely cares about the details while keeping the big picture in mind, which will always be my personal principle in the future, no matter where I am. I also wants to appreciate Prof. Rebeiz to help me find a good job in Qualcomm. His strong recommendation is an important key to my first step towards the industry career. I know, for sure, Prof. Rebeiz will be my advisor, not only in UCSD but in the future life. It has been a great pleasure and honor working with him for the last three years, and Iąęll definitely miss him.

Next, I would like to thank my dissertation committee members, Prof. James F. Buckwalter, Prof. Daniel F. Sievenpiper, Prof. Gert Cauwenberghs and Prof. Brian G. Keating for their time, interest, and valuable comments about my research.

I want to thank my co-authors: Dr. Kevin Ming-Jiang Ho. During these years in the group, I learned a lot from him, especially how to think from fundamentals. He also shared his practical experience on PCB fabrication with me, which prevented my projects from mistakes. I would like to thank Dr. Roberto Gaddi from Cavendish Kinetics for his help and discussion on using CK RF MEMS DVCs. I also want to thank Dr. Allen Tran from Qualcomm for his support on dual-band notch filters.

I'd like to thank my grandfather, Chih-Chang Ko. He took care of me on my life, studies and behaviors. He made me become a better, independent and responsible person. Without him, my life wouldn't be so successful. He is always my goal to achieve in my life.I'd also like to thank my parents, Yueh-Hsiang Tsai and Wen-Ping Ko, for their support. I'd also like to thank my younger brother, Zheng-Xiang Ke, for his friendship and help for taking care my parents while I'm not at home.

I'd like to specially thank my girlfriend, Yu-Hsin Liu, for her understanding, encourage and taking care of my life in UCSD.

There are many people in the TICS group, who are either currently in the group or graduated, that I would like to acknowledge here for their support and friendship: Kevin Ming-Jiang Ho, Yi-Chyun Chiou, Hsin-Chang "Ken" Lin, Ozgur Inac, Samet Zihir, Jennifer Edwards, Yang Yang, Chih-Chieh Cheng, Ozan Dogan Gurbuz, Bilgehan Avser, Tumay Kanar, Chirag Patel, Fatih Golcuk, Woorim Shin, Sang Young Kim, Donghyup Shin, Bon-Hyun Ku, Hong-Ming Lee, Tao Yang, Hosein Zareie, Chenhui Niu, Yu-Chin Ou, Abdullah Al-Azemi, Hyun-Ho Yang, Young Ho Cho and Achref Yahiaoui.

Last but not least, I want to thank all my friends in Taiwan and in the US. My life wouldn't be happier without them.

The material in this dissertation is based on the following papers which are either published, or has been submitted for publication.

Chapter 2 is based on and mostly a reprint of the following paper: CH. Ko, K. M.J. Ho, and G. M. Rebeiz, "An Electronically-Scanned 1.8-2.1 GHz Base-Station Antenna Using Packaged High-Reliability RF MEMS Phase Shifters," *IEEE Trans. Microw. Theory Tech.*, vol. 61, no. 2, pp. 979-985, Feb. 2013.

Chapter 3 is based on and mostly a reprint of the following papers: CH. Ko, K. M.J. Ho, R. Gaddi and G. M. Rebeiz, "A 1.7-2.5 GHz Tunable 4-Pole Filter with Asymmetric Structure and Using Commercial 5-Bit RF MEMS Capacitors," submitted for publication in *IEEE Trans. Microw. Theory Tech.*, Jun. 2014.

Chapter 4 is based on and mostly a reprint of the following paper: CH. Ko and G. M. Rebeiz, "A 1.4-2.3 GHz Tunable Diplexer Based on Reconfigurable Matching Networks," submitted for publication in *IEEE Trans. Microw. Theory Tech.*, Aug. 2014.

Chapter 5 is based on and mostly a reprint of the following paper: CH. Ko, A. Tran and G. M. Rebeiz, "Tunable 500-1200 MHz Dual-band and Wide Bandwidth Notch Filters with RF Transformers," submitted for publication in *IEEE Trans. Microw. Theory Tech.*, Aug. 2014.

The dissertation author was the primary author of the work in these chapters, and co-authors (Prof. Gabriel M. Rebeiz, Dr. Kevin Ming-Jiang Ho, and Dr. Roberto Gaddi) have approved the use of the material for this dissertation.

VITA

2003-2007	B. S. in Communication Engineering, National Chiao-Tung University, Hsinchu, Taiwan
2007-2008	M. S. in Communication Engineering, National Chiao-Tung University, Hsinchu, Taiwan
2011-2014	Ph. D. in Electrical Engineering (Electronic Circuits and Systems), University of California, San Diego, La Jolla, California

PUBLICATIONS

CH. Ko, A. Tran, and G. M. Rebeiz, "Tunable 500-1200 MHz Dual-band and Wide Bandwidth Notch Filters with RF Transformers," submitted for publication in *IEEE Trans. Microw. Theory Tech.*, Aug. 2014.

CH. Ko and G. M. Rebeiz, "A 1.4-2.3 GHz Tunable Diplexer Based on Reconfigurable Matching Networks," submitted for publication in *IEEE Trans. Microw. Theory Tech.*, Aug. 2014.

CH. Ko, K. M.J. Ho, R. Gaddi and G. M. Rebeiz, "A 1.7-2.5 GHz Tunable 4-Pole Filter with Asymmetric Structure and Using Commercial 5-Bit RF MEMS Capacitors," submitted for publication in *IEEE Trans. Microw. Theory Tech.*, Jun. 2014.

CH. Ko, K. M.J. Ho, and G. M. Rebeiz, "An Electronically-Scanned 1.8-2.1 GHz Base-Station Antenna Using Packaged High-Reliability RF MEMS Phase Shifters," *IEEE Trans. Microw. Theory Tech.*, vol. 61, no. 2, pp. 979-985, Feb. 2013.

CH. Ko, IY. Tarn, and SJ. Chung, "A Compact Dual-band Pattern Diversity Antenna by Dual-band Reconfigurable Frequency Selective Reflectors with A Minimum Number of Switches," *IEEE Trans. Antennas Propagat.*, vol. 61, no. 2, pp. 646-654, Feb. 2013.

CH. Ko, K. M.J. Ho, R. Gaddi and G. M. Rebeiz, "A 1.5-2.4 GHz Tunable 4-Pole Filter Using Commercial High-Reliability 5-Bit RF MEMS Capacitors," in *IEEE MTT-S International Microwave Symposium*, Seattle, WA, USA, Jun. 2013.

O. Gurbuz, CH. Ko, J. M. Edwards, and G. M. Rebeiz, "Pattern Ellipticity For Silicon Lenses", in *IEEE Antennas and Propagat. Symp.*, Orlando, FL, USA, 2013.

CC. Cheng, CH. Ko, A. Morris and G. M. Rebeiz, "A Very Low Loss 1.9-2.1 GHz RF MEMS Phase Shifter," in *IEEE MTT-S International Microwave Symposium*, Montreal, Canada, pp. 1-3, Jun. 2012.

ABSTRACT OF THE DISSERTATION

Tunable RF Front-End Circuits for Advanced Communication Systems

by

Chih-Hsiang Ko

Doctor of Philosophy in Electrical Engineering
(Electronic Circuits and Systems)

University of California, San Diego, 2014

Professor Gabriel M. Rebeiz, Chair

This thesis presents tunable RF front-end circuits for advanced communication systems by using packaged RF MEMS (Micro-Electro-Mechanical-Systems) devices or varactor diodes. First, a low-loss reflective phase shifter using commercial RF MEMS SPDT (Single-Pole-Double-Throw) switches is presented. The phase shifter can provide phase shifting of 0-123.75^{o} with a step of 11.25^{o} at 1.8-2.1 GHz. The measured average loss is $\sim$0.83 dB and the measured IP3 is $>$ 65 dB. The 4-element dipole phase array is also presented, which can scan up to 9^{o} with a measured gain of 8.6-8.3 dB at 2 GHz. The array is capable of handling 5-10 W of power with no distortion and suitable for base-station applications.

The second project presents a 1.7-2.5 GHz asymmetric 4-pole tunable filter using the Cavendish Kinetics RF MEMS capacitors. The MEMS capacitors are fabricated and fully packaged using a 0.18 μm CMOS standard process with integrated high voltage drivers and SPI control logic and with reliability in the billions of cycles. The filter results in insertion loss $<$ 3 dB for 8% FBW (fractional bandwidth), a power handling of at least 25 dBm, a second and third harmonic generation of $<$ -110 dBc at 20 dBm, and an IIP3 $>$ 46 dBm. The measured ACPR (adjacent channel power ratio) for a 5-MHz Wideband CDMA signal is at least 54 dB at 25 dBm input power. The project also discusses the requirements on RF MEMS capacitors in order to achieve high performance filters for wireless systems and the effect of ENIG (Electroless Nickel Immersion Gold) on resonator quality factor and filter loss.

Next, an idea for implementing reconfigurable matching networks to realize a tunable diplexer is investigated and demonstrated. The reconfigurable matching networks ensure that the rejection band impedance of every filter is transformed to an open circuit over a wide range of frequencies, allowing two tunable filters to be connected together to form a tunable diplexer without affecting each other. The tunable diplexer is built using Schottky diodes and combline resonators on Duroid substrates, and can operate from 1.4-2.3 GHz with a closest frequency separation of 110 MHz. Measurements show virtually no difference in the frequency response between a stand-alone filter and a filter placed in the tunable diplexer. The work shows that a wideband tunable diplexer can therefore be realized using tunable bandpass filters and reconfigurable matching networks.

Finally, a novel tunable dual-band bandstop filter based on doubly-tuned RF transformers is presented. This design results in two distinct notch frequencies in a single resonator using silicon varactor diodes. The 2-pole tunable dual-band bandstop filters are implemented using PCB transformers and air-coil transformers. With PCB transformers, the lower frequency can be tuned at 513-845 MHz while the higher frequency can be tuned at 715-1151 MHz with a notch level $>$ 16 dB. With air-coil transformers, a single-band 2-pole notch filter with wide rejection bandwidth is achieved. The design results in 604-982 MHz tuning with a 20-dB rejection bandwidth of 27-45 MHz. Also, by implementing a series varactor in a transformer, the separation between two coupled

frequencies can be changed. The topology can be easily extended to higher-order filters and design equations are presented.

Chapter 1

Introduction

1.1 Tunable Passive RF Front-End

With the rapid development of the modern communication system, there is an increasing demand on communication bandwidth for mobile entertainment. To satisfy people's demanding, more and more bands crowd into the limited spectrum (Fig. 1.1). However, increasing bands in the limited spectrum is not enough to support the required operating bandwidth. As a result, in the latest 4G system (LTE : Long-Term Evolution), Multiple-Input-Multiple-Output (MIMO) and carrier aggregation [2] technologies are applied to get more data throughput out of the crowded radio frequency (RF) spectrum. MIMO can divide high-speed data into several pre-coded low-speed data and transmit at the same time through multiple antennas (Fig. 1.2), and therefore, high-speed communication can be achieved without requiring wider RF bandwidth. However, it requires multiple antennas and increases the size of the devices. Carrier aggregation uses multiple bands to transmit and receive signals simutaneouly in the existing communication systems to increase data throughput. Comparing to MIMO, it doesn't require several antennas and therefore, the cost and size of the devices doesn't increase much. There are three modes of carrier aggregation (Fig. 1.3): 1) intra-band: contiguous carriers; 2) intra-band: non-contiguous carriers; 3) inter-band aggregation.

In order to reduce noise and interference, multiple sets of RF components (bandpass filters, bandstop filters and switches, etc.) are required for each individual bands. However, this makes the whole RF chain more complicated, expensive and larger. To

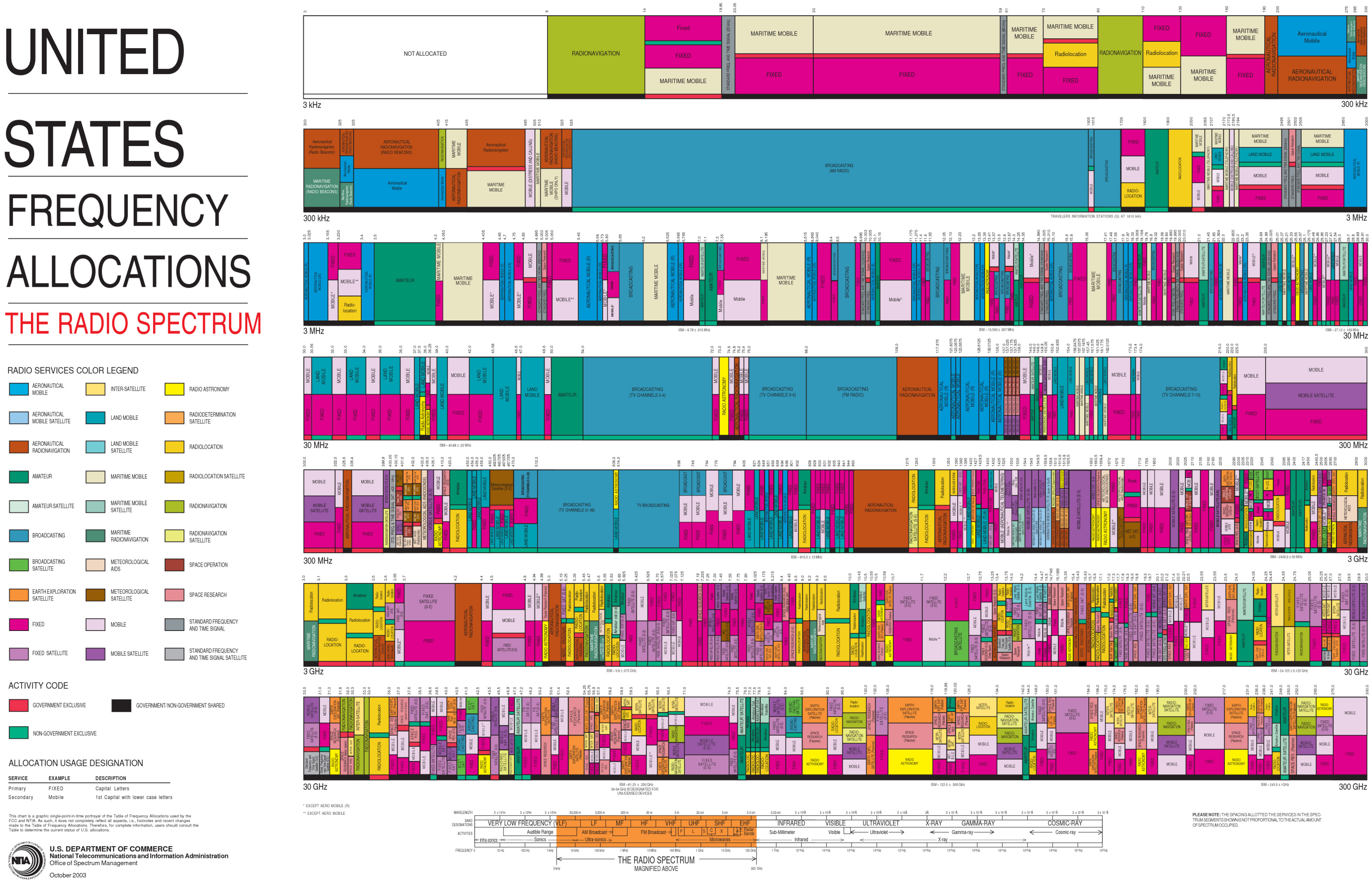

Figure 1.1: RF spectrum in the United States of America.

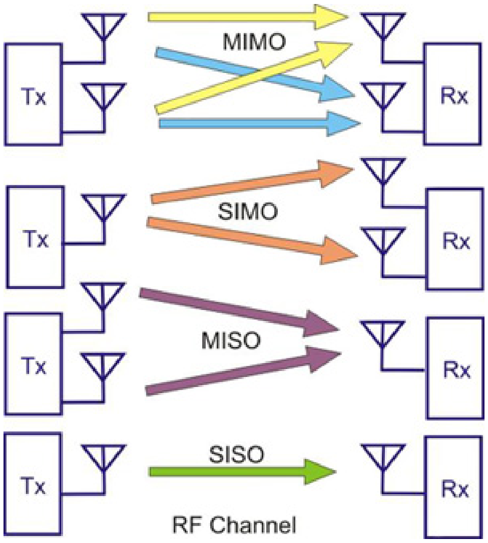

Figure 1.2: The operating fundamentals of the MIMO system.

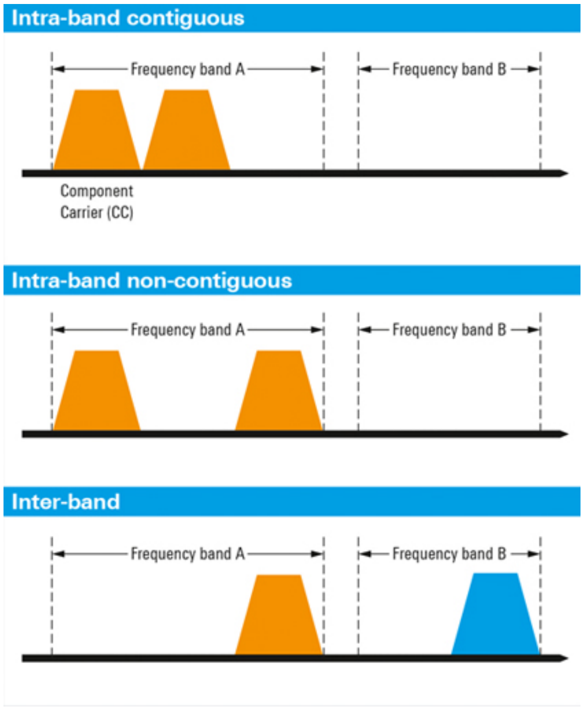

Figure 1.3: Three types of the carrier aggregation.

reduce the system complicity, cost and size, tunable RF front-end circuits draw lots of attention (Fig. 1.4). For example, a tunable bandpass filter can replace a SPNT (Single-Pole-N-Throw) switch and a fixed bandpass filter bank.

Recently, there are lots of research literature about tunable RF circuits. One way to design a tunable circuit is using mechanical movement. However, it is relatively slow, bulky and expensive, which can not support the requirement of rapid switching between bands. The other way is using electrical tuning components. Ferroelectric devices [3] are investigated and used but they are relatively low Q. P-I-N diodes [4] and varactor diodes [5–13] are also commonly used since they are cheap, easy to use and have large tuning ratio. However, they suffer from high RF loss and low linearity, which de-sensitize receiver systems and waste power and generate interference for transmitter systems. Due to above disadvantages of the existing tuners, RF MEMS (Micro-Electro-Mechanical-System) devices [14] become one of the potential solutions for the tunable systems since it has the properties of low loss and high linearity.

1.2 RF MEMS Technology

RF Micro-Electro-Mechanical-Systems (MEMS) devices can provide higher performance than traditional solid-state circuits, such as low-loss, high linearity, high power handling and low power consumption. However, its reliability was one of the biggest problems to be widely used. Due to tremendous efforts on improving devices, RF MEMS can operate at least 100M cycles without any problems nowadays. There are lots of research literature about implementing RF MEMS devices on tunable circuits to show its outstanding performance [15–22]. Nevertheless, all of them were using in-house RF MEMS devices, which are not packaged, and therefore it's not easy to expand to mass production.

Recently, RF MEMS technology is entering a mature stage with commercial vendors offering packaged devices with high reliability and power handling. These include Omron and Radant MEMS for ohmic contact switches [23,24], and wiSpry and Cavendish Kinetics for capacitive switches [25,26], as shown in Fig. 1.5. These devices are well-packaged with high liability and easy to control since they are integrated with

CMOS circuits to provide required operating voltage and control. This thesis presents the first tunable circuits using commercial RF MEMS devices to demonstrate their high performance.

1.3 Contents of the Thesis

The thesis presents the first passive phase shifter and the tunable filters using commercial RF MEMS devices, the application of tunable matching networks for tunable diplexers and tunable dualband bandstop filters for modern communication systems.

Chapter 2 presents the passive reflective phase shifter using commercial RF MEMS switches. The phase shifter consists of two stages in order to achieve 123^o for a 4-element phase array with scan angle up to 10 degree. Due to the special properties of the Omron switches, 4 different switch states can be provided and therefore phase-shifting step of 11.25^o is achieved. The phase shifter shows low loss of < 1 dB and high linearity at 1.8-2.1 GHz, which is good for base-station applications. A 4-element dipole phase array is also presented. The measurement and simulation agrees well.

Chapter 3 presents the first tuanble 4-pole bandpass filter using commercial RF MEMS varactors. In this chapter, an asymmetric filter structure is introduced to enhance the passband flatness in the higher edge of the frequency tuning range. Also, the effect of electroless nickel immersion gold (ENIG) on filter loss is investigated and discussed. The fabricated 4-pole combline fitler shows the properties of low loss and high linearity and it is able to replace the fixed filter banks connected to the antennas.

Chapter 4 presents the idea of a tunable diplexer using tunable matching networks. The tunable diplexer consists of two tunable 3-pole combline filters and two tunable π matching networks. Using tunable matching networks leads to a tunable diplexer without any complicated design process. The tunable diplexer is designed and fabricated with varactor diodes to verify the idea.

Chapter 5 presents the tunable dual-band bandstop filters. The filter is composed of RF transformers within resonator elements. Due to the coupling between two inductors in a transformer, two coupled resonant frequencies can be generated in a single

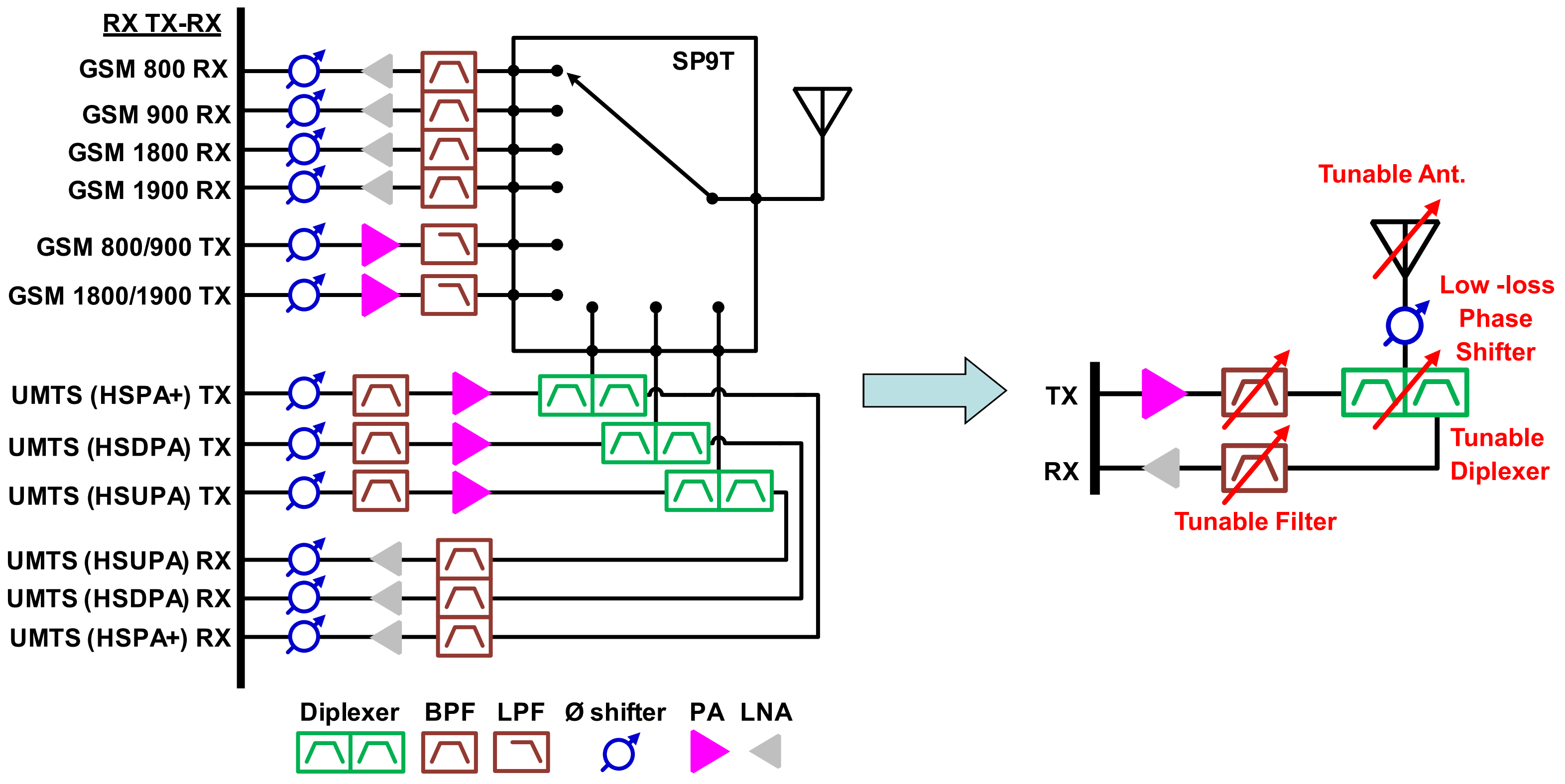

Figure 1.4: Using tunable RF circuits reduce the complexity of modern communication systems.

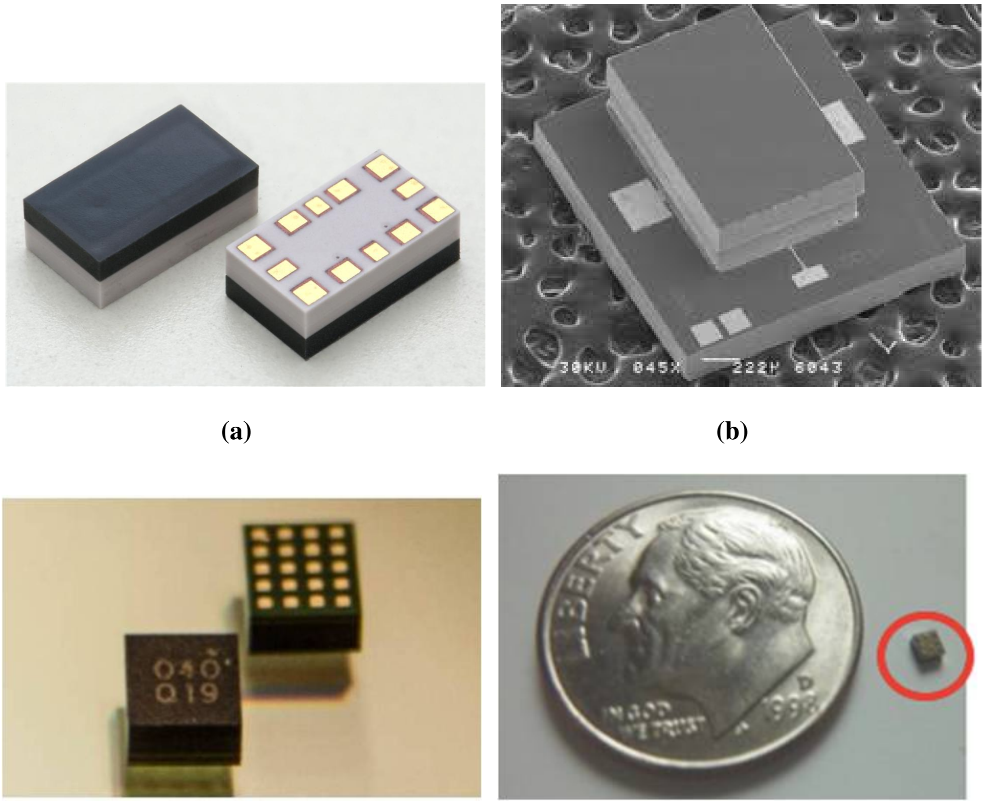

(a) (b)

(c) (d)

Figure 1.5: (a) Schematic of an ideal dual-band resonator and its frequency responses when (b) $K_{xfmr} = 0.332$ and (c) $K_{xfmr} = 0.15$.

resonator. The analysis and simulations of a resonator with a transformer agree very well with each other. Due to the different magnetic coupling level of the RF transformers, a dual-band bandstop filter or a single-band bandstop filter with wide rejection bandwidth are designed and measured. In addition, a tunable dual-band bandstop filter with tunable notch frequency separation is also introduced.

Chapter 6 concludes the works and presents the idea of future works.

Chapter 2

An Electronically-Scanned 1.8-2.1 GHz Base-Station Antenna Using Packaged High-Reliability RF MEMS Phase Shifters

2.1 Introduction

RF MEMS (radio frequency micro-electro-mechanical-systems) phase shifters have been extensively researched since 1996 for phased array applications [27]. Several topologies have been demonstrated, such as reflect-line [28–31], switched LC and true-time delay networks [32–36], and wideband loaded lines [37–40]. The designs are based on different types of RF MEMS devices: metal-contact switches, capacitive switches (capacitance ratio, C_r = 20-50) and switched-capacitors (C_r = 5-8). Also, most of the work has concentrated on 8 to 100 GHz demonstrations where RF MEMS phase shifters has shown much better performance as compared to GaAs FET or p-i-n diode implementations, but recently, Cheng et al. also demonstrated a low loss RF MEMS phase shifter at 2 GHz with 1.1 dB average insertion loss [30].

Base-station antennas, which are built using a 3 or 4-element linear antenna array, are typically mounted on a high platform such as a building or a tower and therefore require an angular tilt in their pattern for best coverage (Fig. 2.1). This is achieved using either a one-time mechanical tilt or using mechanical phase shifters at each antenna element for vertical pattern adjustment vs. time and location. The phase shifters must have low-loss and extremely low distortion, and cannot create any additional harmonics or cause spectral re-growth. The reason is that they are placed after the power amplifier and harmonic filter, and therefore, any spurious response from the phase shifters is radiated by the antennas. They also need to handle 2-5 W for low-power designs and up to 20-50 W for high-power base-stations.

Currently, base-station phase shifters are implemented using stepper motors, which are expensive, add weight to the antenna structure and are not suitable for the new generation of miniature base stations. However, being of a mechanical design, they have a low loss of 0.3-0.5 dB at 2 GHz and can handle $>$ 10 W of power with no distortion [41,42]. RF MEMS switches offer a perfect solution for base-station antennas with 5-10 W of radiated power, which are becoming prevalent in micro and pico base stations. They also result in low-loss phase shifters, can handle 1-5 W with high reliability (depending on the switch design) and are extremely linear.

This chapter combines RF MEMS switch technology, together with phase shifters and antenna design, to demonstrate the first high-performance passively-scanned 4-element phased array at 1.8-2.1 GHz. The phased array can operate between 1.8-2.1 GHz in any contiguous bandwidth of 1 MHz (CDMA), 5 MHz (W-CDMA), 5-10 MHz (LTE) and also 40-60 MHz bandwidths for covering a full allotted spectrum [2].

2.2 Characterization of the Omron Switch

The phase shifters are based on the Omron single-pole double-throw (SPDT) metal-contact switch, which is a hermetically-packaged high-reliability RF MEMS switch in a surface-mount configuration (Fig. 2.2) [23]. The switch combines two single-pole single-throw (SPST) switches in a land-grid array (LGA) package and uses the common input port to form a SPDT switch. The overall size is 5.2 mm x 3 mm x 1.85 mm.

The Omron switch was tested at UCSD for 4 continuous months and for billions of total cycles at 0.01-9 W, under cold switching conditions, and its resistance was con-

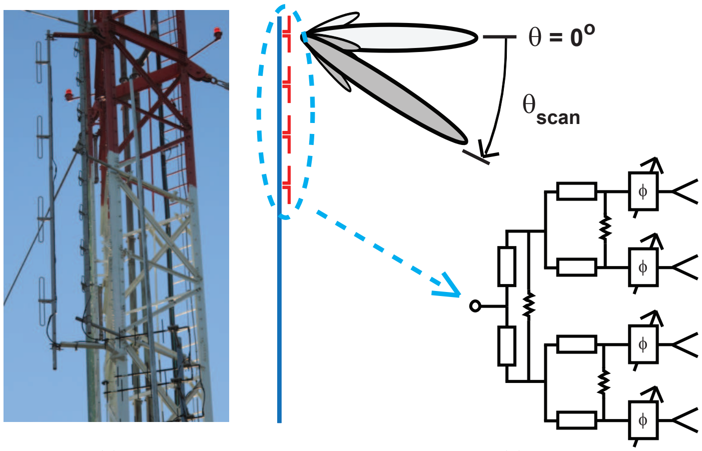

(a) (b)

Figure 2.1: (a) Picture of 4-element linear array in base stations, and (b) electronic passive vertical beam scanning with Wilkinson divider and phase shifters.

stant at 1.1±0.1 Ω (Fig. 2.3(a)). It was also tested under hot-switching conditions with an RF power of 100-300 mW, and it operated up to 100 M cycles (test stopped due to time limitations). However, at 0.5-1 W hot-switching conditions, the switch failed at $\sim$5 M cycles (Fig. 2.3(b)). It was also tested under continuous operation at 0.1-5 W (hours and days for each test) and its resistance was measured every few hours and remained constant to within ±0.1 Ω (Fig. 2.3(c)). The pull-down (28 V) and release voltage (15 V) were measured over 3 days of continuous actuation (once every hour) and no change was detected. All testing was done at 2 GHz and cycle testing was done at 1 kHz. The Omron SPDT switch has also excellent RF performance. In the on-state (thru), the measured insertion loss is $<$ 0.5 dB up to 5 GHz with $S_{11} <$ -19 dB. In the off-state (isolation), the measured isolation is $>$ 40 dB up to 5 GHz.

Since the Omron SPDT switch combines two SPDT together, it has a distinctive feature, comparing to commercial SPDT components : Four different switch states instead of two. As shown in Fig. 2.4, the four states are 1) State S1: both switches Off; 2) State S2: Switch1 On, Switch2 Off; 3) State S3: Switch1 Off, Switch2 On; 4) State S4: both switches On. For S4, the input impedance of the switch drops to half since a T-junction is formed by both switches on.

A fitted RLC model for the Omron SPDT on Rogers RO4350 substrate (ε_r = 3.66, h = 10 mils) and which is valid to 4 GHz is shown in Fig. 2.5. Note the 0.6-1 pF capacitance to ground at the input and output ports due to the large solder pads. For the phase shifter design, the Omron SPDT switch is not used in a standard 50-Ω environment, but is used to switch resonant LC loads in the reflect phase-shifter. Therefore, it is essential that an accurate circuit model be used which takes into account the packaging parasitic (Fig. 2.6). This is achieved by placing the switch in a 3-port circuit, calibrating out the connectors and transmission-lines, and measuring the S-parameters under four different switching conditions. The 3-port S-parameters are used as switch properties in the phase shifter design, but it is also important to study the equivalent circuit model so as to understand the switch parasitic especially at the common port (Fig. 2.6). It is seen that the SPDT has an effective capacitance to ground of C_S = 1-2.4 pF at 2 GHz which is dependent on the SPDT state. The effective series resistance, R_S, is very low ($<$ 1 Ω).

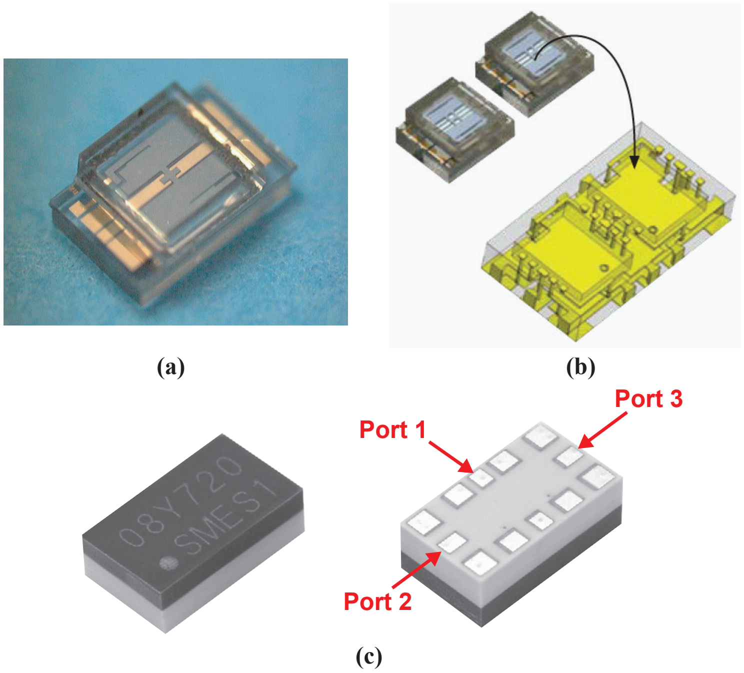

(a) (b) (c)

Figure 2.2: Omron switch : (a) SPDT switch, (b) two SPDT in a LGA package and (c) Commercially packaged SPDT switch.

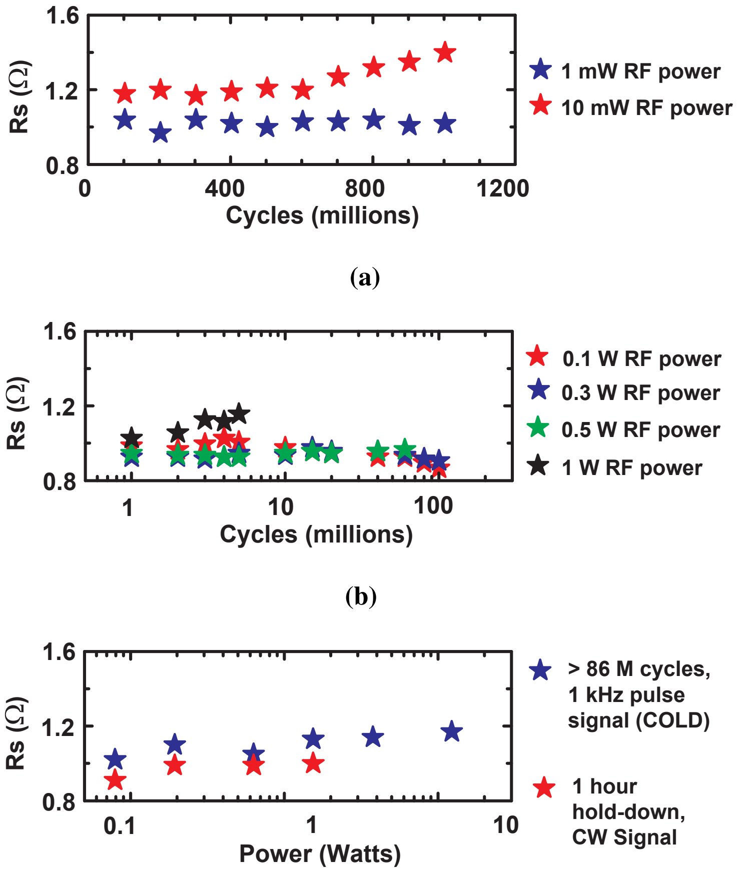

(a)

(b)

(c)

Figure 2.3: Reliability test for Omron MEMS SPDT switches : (a) cold switching, (b) hot switching, and (c) power handling.

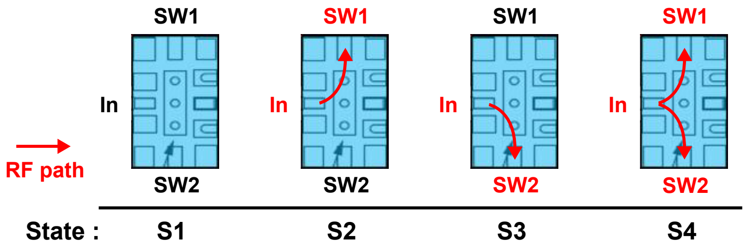

Figure 2.4: Four states of the Omron switch operation.

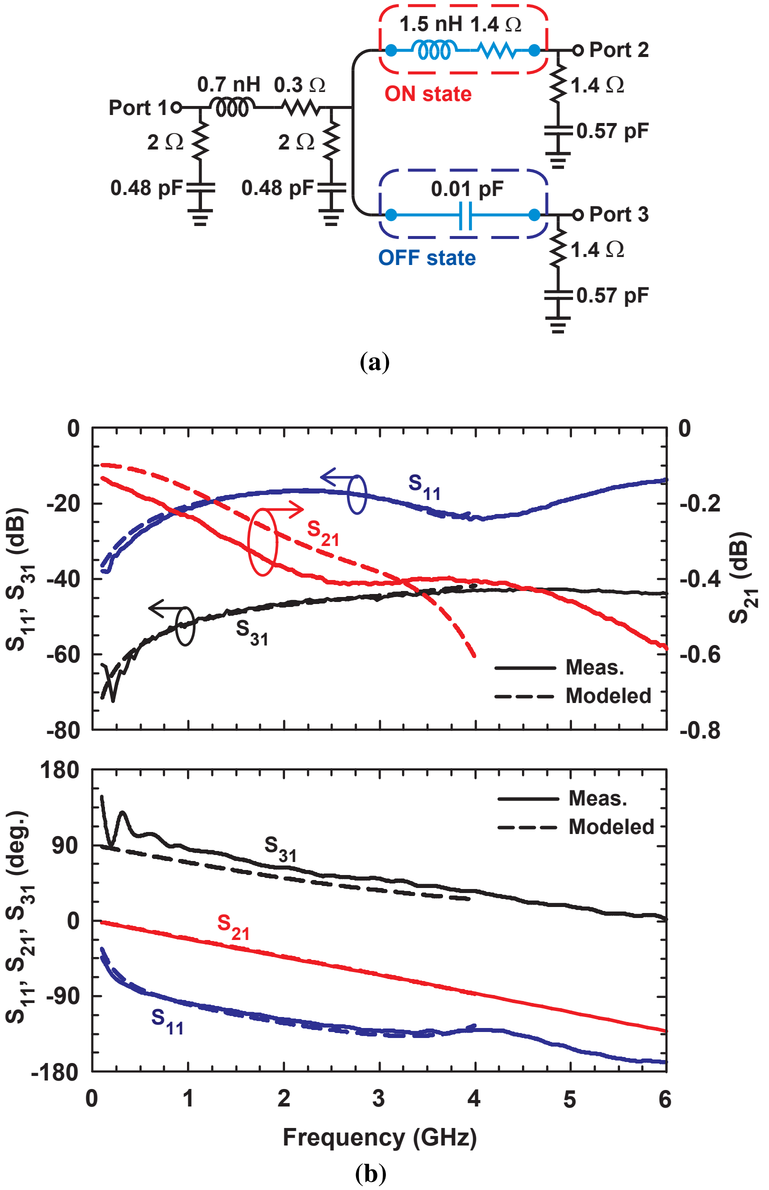

Figure 2.5: (a) Fitted lumped-element model, and (b) measured and modeled response.

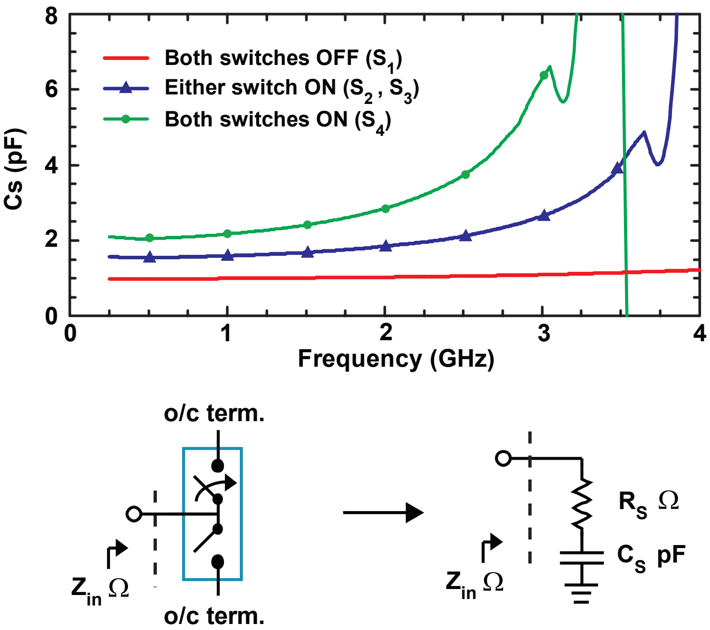

Figure 2.6: Fitted impedance at the common port for different switch states with both output ports at open termination.

2.3 Phase Shifter and Antenna Array Design

2.3.1 Phase Shifter Design

For base-station applications, the maximum phase shift is given by the 4-element array and the scan angle of 10^{o}, and is:

$$\alpha_{max} = -3kdsin\left(10^{o}\right) = -3 \times 37.5^{o} = -112.5^{o} \qquad (2.1)$$
$$(k = 2\pi/\lambda, d = 0.6\lambda)$$

Therefore, the design goal is to achieve a phase shift of up to 135^{o} with a linear phase step and very low loss. Due to the narrow band nature of the signals (1-60 MHz), the phase-difference slope vs. frequency is not critical and a constant phase shifter design is acceptable. However, the absolute phase shift of every state is linear versus frequency in order to have minimal dispersion.

A reflection-type phase shifter based on quadrature couplers and switched LC loads is shown in Fig. 2.7(a). In this design, the Omron SPDT switches are used as phase control components by switching in capacitive stubs. However, due to the relatively high input parasitic capacitance of these switches when both poles are actuated, it was impossible to achieve a 135^{o} phase shift with a linear phase step using a single coupler, and therefore a two-stage phase shifter is employed. In the two-stage phase shifter, the phase step in the first stage is chosen to be 0^{o}, 11.25^{o}, 22.5^{o} and 33.75^{o} while that of the second stage is 0^{o}, 45^{o}, and 90^{o}.

An LC reflective load is shown in Fig. 2.7(b) with an SPDT switch. In this design, 4 capacitive states can be achieved and are given by the equivalent capacitance, $C_{in} = C_{S,S1}$ for S1, $C_{in} = C_{S,S2}+C_1$ for S2, $C_{in} = C_{S,S3}+C_2$ for S3 and $C_{in} = C_{S,S4}+C_1+C_2$ for S4. As discussed above, C_S is the effective capacitance seen at the common port and its value changes depending on the switch status. Since high Q capacitors are used, R_{in} is $< 1\ \Omega$ for all switch states.

For the first stage with 0^{o}, 11.25^{o}, 22.5^{o} and 33.75^{o} phase shifts, the inherent parasitic capacitance (C_S = 1-2.4 pF) of the Omron SPDT causes difficulties in finding suitable loading capacitance, C_1 and C_2, and an additional capacitor, C_{P1}, was added in order to adjust the total capacitance range and to achieve realizable values for C_1 and

C_2. The additional capacitor, C_{P1} keeps the effective reactance of C_{in}+C_{P1} relatively constant and results in a phase shift that is stable with respect to frequency. In addition, C_{P1} also reduces the reflective loss as shown in [43]. This is explained in Fig. 2.8: Z_{in} as seen from the common port is a series RC. With a shunt capacitor, the new effective capacitor Q becomes

$$Q_{in,new} = \omega(C_{P1} + C_{eq})(R_{in}//R_{P1}) = \omega(C_{P1} + C_{eq})(\frac{R_{in}R_{P1}}{R_{in} + R_{P1}}) \tag{2.2}$$

If a high-Q shunt capacitor is added, $R_{in}//R_{P1} \sim= R_{in}$ since $R_{P1} >> R_{in}$ and therefore the total Q of load is increased, which reduces the reflective loss. The series resistance of the SPDT swith (R_s = 1-2 Ω max) causes a 0.5-0.7 dB reflection loss. However, by using C_{P1} (1.7 pF for the first stage) to increase the equivalent resistance, R_{eq}, the reflective loss is reduced to 0.2-0.5 dB.

The inductor value is also important to the phase shift bandwidth. If a large inductance is chosen, the total load reactance is dominated by the inductance which causes a large phase variation at higher frequencies, and the effective bandwidth in terms of phase shifter will be reduced. The reflective phase of a LC load is investigated based on different reactance of the series inductor. As shown in Fig. 2.9, for different reactance of the series inductor, the capacitance is chosen to achieve desired reflective phase at 2 GHz for a 4-bit 180^o phase shifter. As you can see, when the chosen reactance becomes larger, the phase errors are more severe away from the center frequency, 2 GHz. Therefore, a smaller inductance is preferred and based on the investigation, $X_L < 70\,\Omega$ should be a good guideline for choosing series inductor value.

In the first stage, L_1 = 1.65 nH (X_L = 20.7 Ω at 2 GHz) is chosen (see Table 2.1). The simulation results of the first stage are shown in Fig. 2.10(a). The insertion loss is $<$ 0.4 dB and the phase variation is $< 2.5^o$ from the nominal phase values of 0^o, 11.25^o, 22.5^o and 33.75^o at 1.7-2.5 GHz.

For the second stage with 0^o, 45^o, and 90^o phase shifts, the same topology as the first stage is used but with large loading capacitances, C_3 (0.2 pF) and C_4 (1.2 pF). Since, $C_4 >> C_3$, the final state S4 (C_3 and C_4 selected) does not result in a significant phase shift as compared to C_4 alone. As a result, only three phase shifts are available in the second stage for switch state S1 (none selected), S2 (C_3 selected) and S3 (C_4 selected) (Fig. 2.10(b)). In this case, larger phase variations against frequency are ob-

Table 2.1: Optimized LC Design Values for the 2-Stage Phase Shifter

Stage	Component	Value	Implementation Microstrip (Z_0, l) or Lumped
Stage1			
	L_1	1.65 nH	(94.7 Ω, 0.07λ_{eff})
	C_{p1}	1.7 pF	ATC capacitor
	C_1	0.1 pF	(61 Ω, 0.008λ_{eff})
	C_2	0.6 pF	(39 Ω, 0.038λ_{eff})
Stage2			
	L_2	2.55 nH	Coilcraft inductor
	C_{p2}	0.4 pF	(94.7 Ω, 0.07λ_{eff})
	C_3	0.2 pF	(61 Ω, 0.008λ_{eff})
	C_4	1.2 pF	(39 Ω, 0.038λ_{eff})

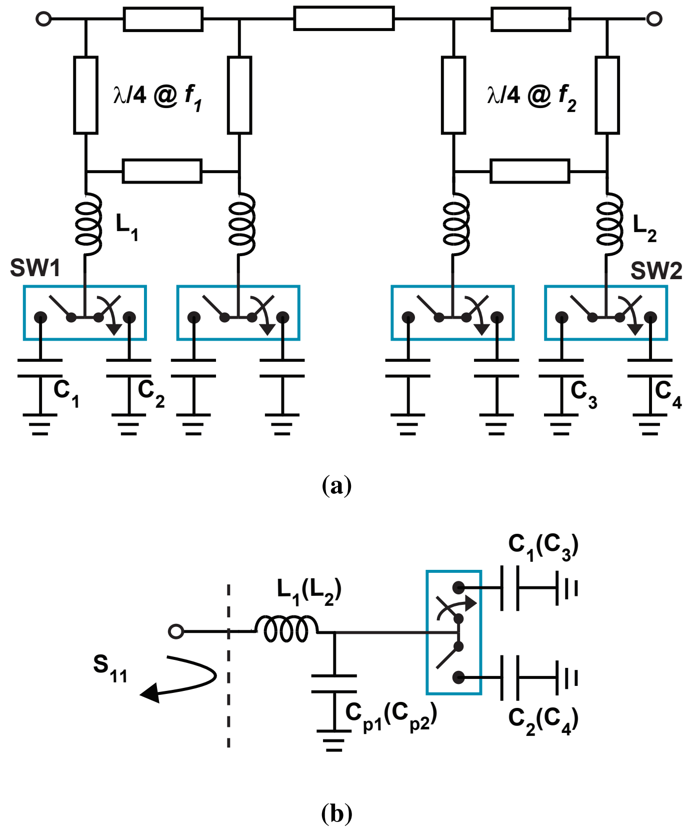

Figure 2.7: (a) Schematics of the two-stage phase shifter, and (b) detail of the switched LC load.

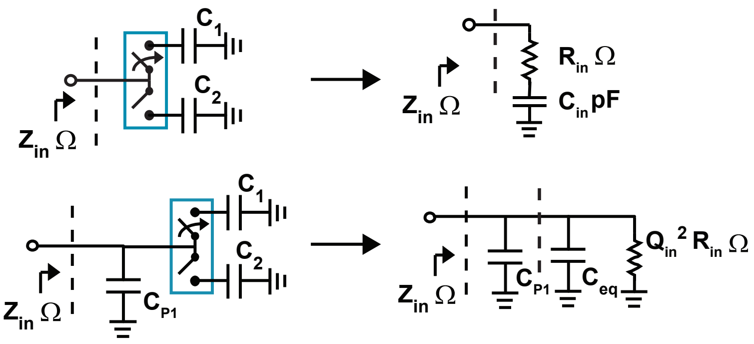

Figure 2.8: Effect of C_p on the loading network.

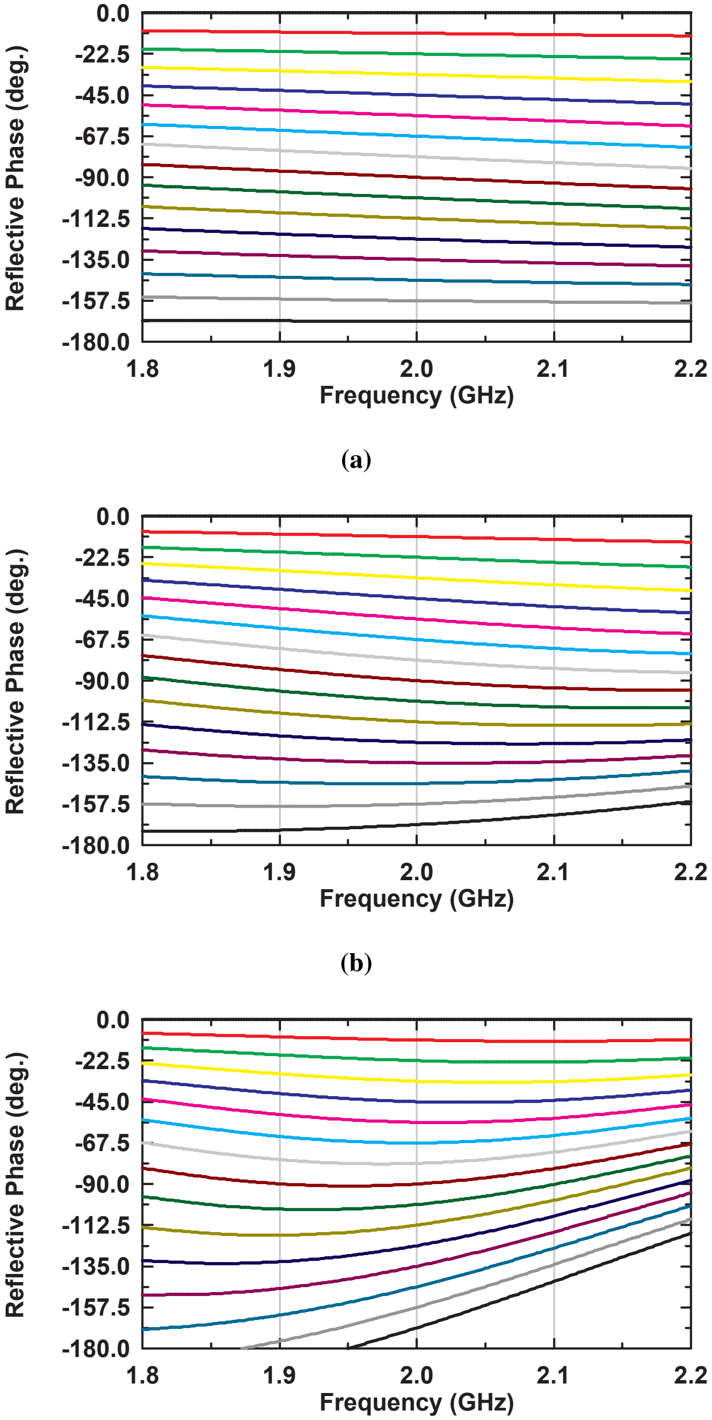

(a)

(b)

(c)

Figure 2.9: Reflective phase v.s. frequency : (a) X_L = 20 Ω, (b) X_L = 70 Ω and (c) X_L = 130 Ω.

served because of the larger inductance and capacitance ratio. In addition, the loss of the fourth state increases faster than the other three states with no phase change, and this is why state S4 is not used. Due to the relatively large capacitance of C_4, only small value of C_{P2} is required to reduce reflection loss, which is 0.4 pF.

Table 2.1 summarizes the L and C values for the phase shifter. The capacitor values were adjusted based on the effect of the parasitic capacitance from the substrate and of the actual components. In addition, 1-MΩ resistors are used for electrical discharge protection. For minimum loss, all the lumped elements with small values were replaced by low-loss microstrip lines with varying Z_0 and lengths (shown in Table 2.1), and only the large-value components are kept as lumped elements. In this design, high-Q Coilcraft Micro-Spring inductors and ATC 600S capacitors are employed both having a Q $>$ 100 at 2 GHz.

The quadrature couplers with the microstrip-line components and the pads were designed using full-wave EM simulations (Sonnet [1]). The substrate is RO4003 with $\varepsilon_r = 3.55, h = 32$ mils and $\tan\delta$ = 0.0029, with a simulated transmission-line Q of 177 for a 50 Ω line and a quadrature coupler loss of 0.22 dB at 2 GHz. The Modelithics models [44] for the Coilcraft inductors and ATC 600S capacitors were also used in ADS [45] for accurate simulations. In addition, the center frequencies of the two quadrature-coupler phase shifters are chosen to be slightly different due to different loading capacitances in order to get a wider bandwidth, and therefore, the interstage microstrip transmission-line length is optimized for minimum insertion loss (Z_0 = 50 Ω, θ = 88^o).

The phase shifter simulations (ADS+Sonnet+SPDT S-parameters) show a -10 dB input impedance bandwidth of 1.8-2.2 GHz for all phase states. The phase changes from 0^o to -123.75^o in 11.25^o steps at 2 GHz with an average insertion loss of 0.82 dB. The maximum phase error is about $\pm$3.3^o from a linear phase step, and the *rms* (root-mean-squared) gain error is $<$ 0.1 dB. As shown in Fig. 2.11, at 1 W of input power, a *rms* current of 44-146 mA passes by the Omron switches when actuated over the entire phase states. This is well within the power handling limits of the Omron switch (tested at 10 W, $\sim$0.5 A_{rms}, for $>$ 100M cycles).

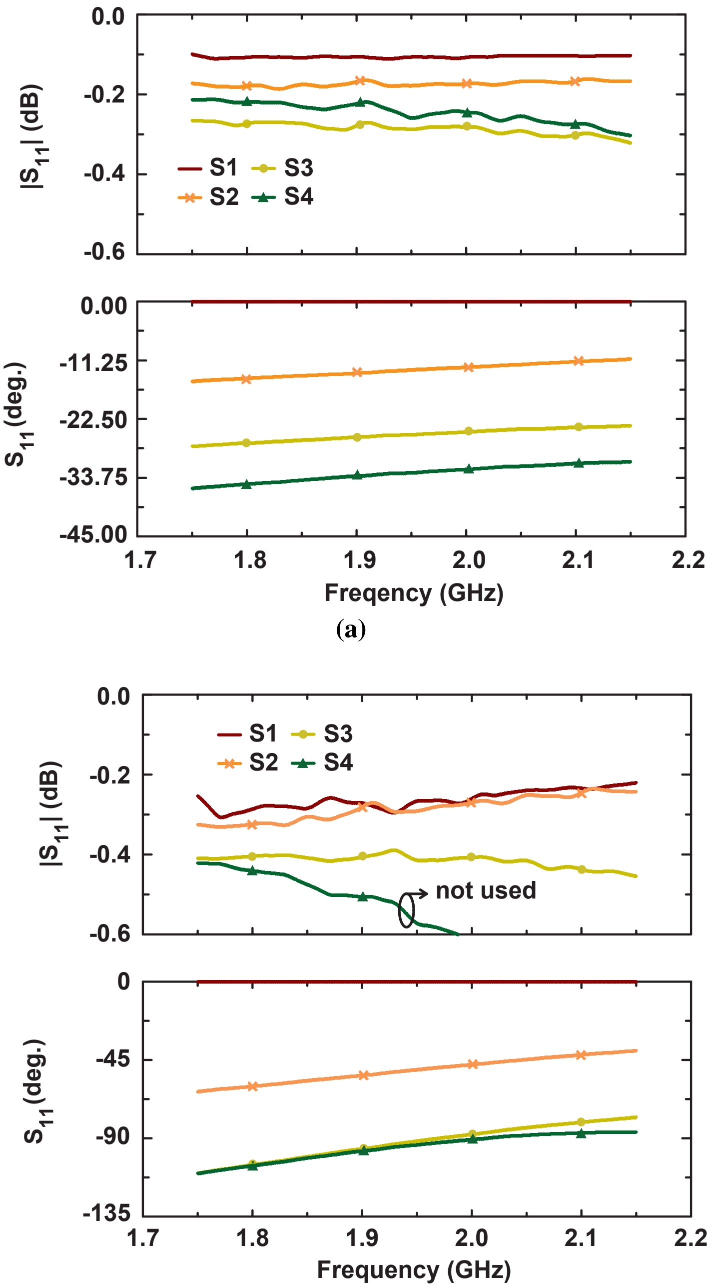

(a)

(b)

Figure 2.10: Simulated S_{11} for (a) the first stage, and (b) the second stage of the reflective phase shifter. The simulations include the 3-dB hybrid coupler.

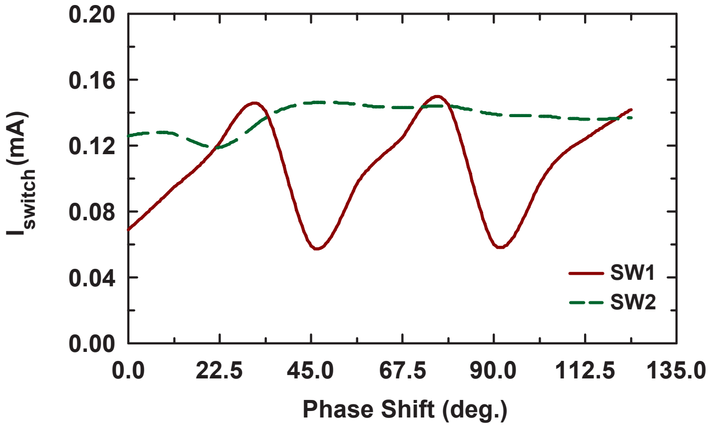

Figure 2.11: Simulated *rms* current at the common port of the SPDT switch at 2 GHz.

2.3.2 4-Element Phased Array Design

An angled-dipole antenna was chosen to result in a wide element-pattern beamwidth for minimizing the array gain reduction when scanning to 9^{o}-10^{o} [46]. Also, a 1-to-4 microstrip Wilkinson power divider is used to divide the power equally between the 4-antennas. The antenna element spacing is 0.6 λ_{o} and this results in a simulated mutual-coupling of $<$ -25 dB at 2 GHz. The 4-element phased array was simulated using HFSS [47], and the directivity is 9.8 dBi for $\theta_{scan} = 0^{o}$-9^{o}, not including the Wilkinson divider loss, transmission-line loss, and phase shifter loss. The array gain drops to 8.6 ± 0.1 dB for when all losses are included (referred to the input coaxial port).

2.4 Measurement

2.4.1 Phase Shifter

Fig. 2.12 shows the fabricated reflective-type phase shifter. The VNA is calibrated up to the connectors using a standard SOLT calibration, and Fig. 2.13 presents the measured phase shifter response for 12 different phase states. The results agree well with simulations with a measured loss of 0.83 ± 0.1 dB at 2 GHz, and an input impedance match $<$ -10 dB at 1.8-2.15 GHz. The measured phase steps are 11^{o} with a maximum absolute error of 5^{o} at 2 GHz, and the rms error is $< 5^{o}$ at 1.8-2.1 GHz (as defined in [48]). The phase shifter operates well from 1.8-2.1 GHz.

The Omron switches have very high linearity due to the low resistance ohmic contact, and therefore, the measurement setup is very critical to the accuracy of the measurement. The measurement setup is shown in Fig. 2.14(a): the isolator is used to prevent the reflection from the DUT (Device Under Test, the phase shifter in this case) and the LPF (low-pass filter) is to block any harmonics from power amplifiers. Also, the attenuation in the spectrum analyzer is important to avoid any large non-linearity component generated from itself. The measured IIP3 under all phase states show a worse case IIP3 of +65 dBm for Δf = 500 kHz to 5 MHz (Fig. 2.14(b)). The IIP3 is independent of Δf as expected from ohmic contacts. The measured second and third harmonic generation is $<$ -100 dBc at 30 dBm of input power (worse-case) and with

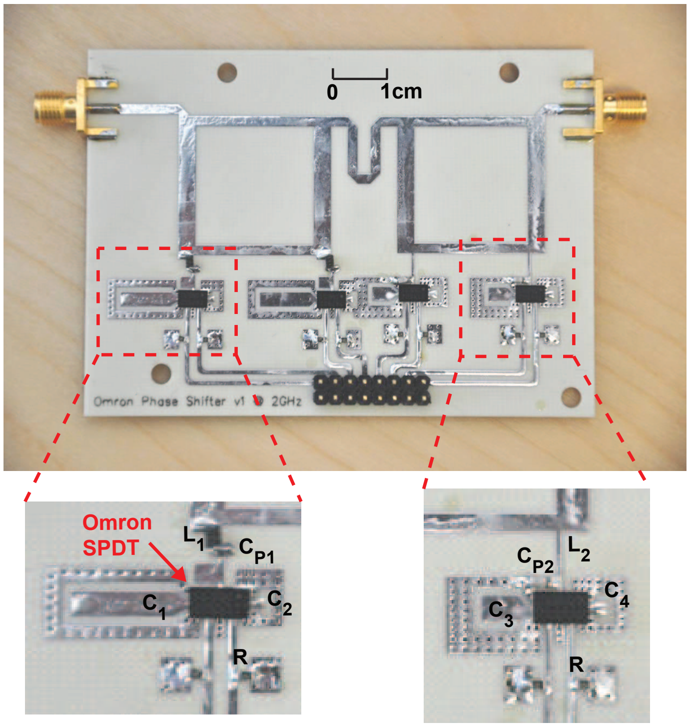

Figure 2.12: Picture of the reflective-type phase shifter.

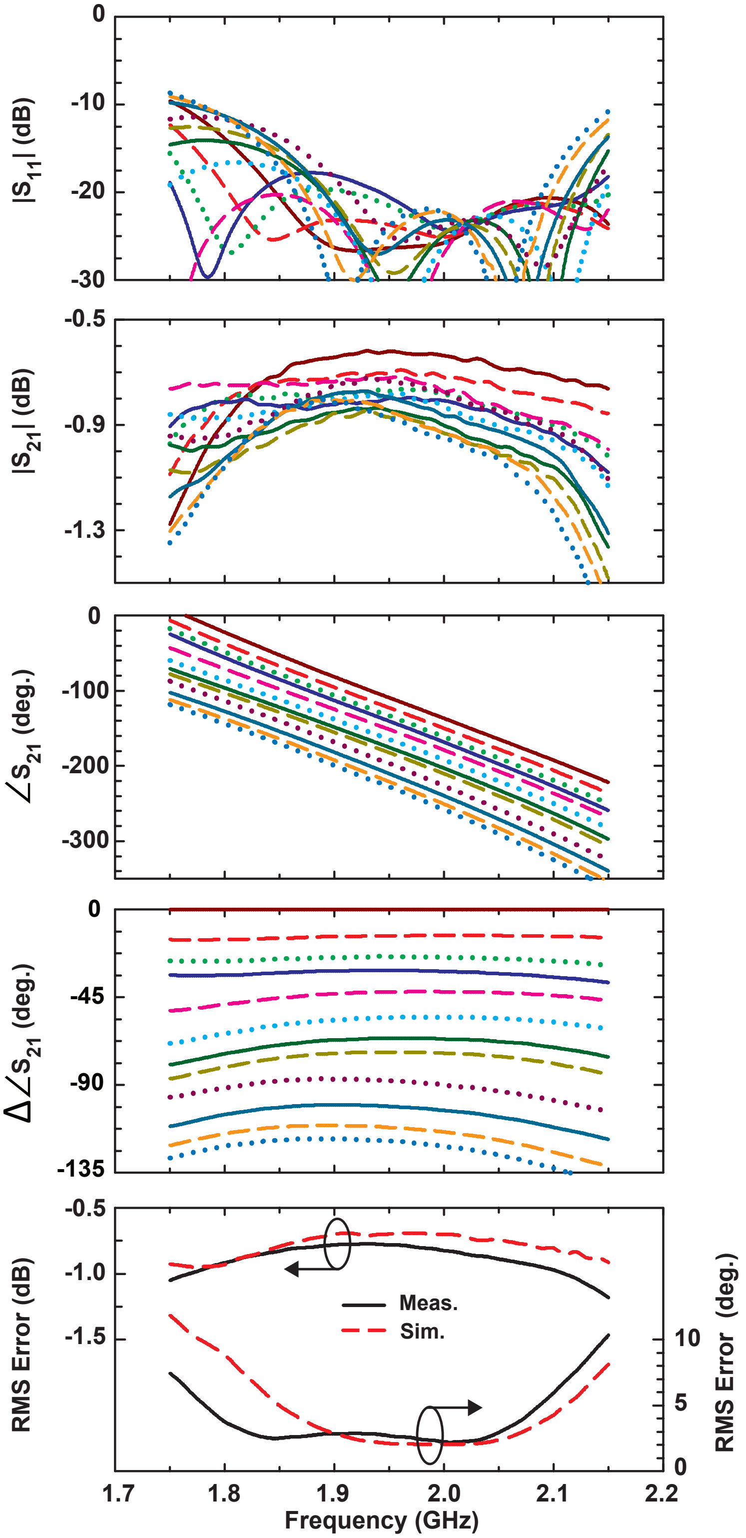

Figure 2.13: Measured 2-stage reflective phase shifter versus frequency.

several phase states being $<$ -120 dBc. The measured output spectrum is shown in Fig. 2.15 for a 30-dBm average power 5-MHz wideband CDMA signal with a peak-to-average ratio of 4. It is seen that no spectral regrowth is present at any phase state.

2.4.2 4-Element Phased Array

The linear phased array was tested in a SATIMO SG32 system [49] at Qualcomm Corp. R&D, San Diego, CA. The array gain was measured using bazooka baluns at the antennas so as not to excite any current on the Wilkinson combiners or backing ground planes (Fig. 2.16(a)). The measured input reflection coefficient is $<$ -10 dB at 1.8-2.1 GHz over all scan angles. the antenna scans in 3^o steps, at $\theta_{scan} = 0^o$, 3^o, 6^o and 9^o for an incremental phase shift on $\phi = 0^o$, -11.25^o, -22.5^o and -33.75^o with a measured gain of 8.6-8.3 dBi at 2 GHz which is very close to simulations (Fig. 2.16(b)). The 4-element phased array has a loss of $\sim$1.2 dB (0.8 dB phase shifter, 0.2 dB Wilkison divider, 0.2 dB connectors/transmission-lines) and provides $\sim$5 dB net gain over a single element. The measured E-plane patterns agree well with simulations with a 3 dB beamwidth of $\sim 16^o$ (Fig. 2.17), and the cross-polarization level is $<$ -23 dB at all scan angles.

Finally, the phased array was tested with a 10 W input power ($\sim$2.3 W per phase shifter) and no degradation was observed. The phased array was also tested using a WCDMA signal with different power levels. As with the reflective phase shifter measurements (Fig. 2.14 and 2.15), all the distortion of the WCDMA signal were due to the limitation of the power amplifier at high output power. No spectral regrowth was produced at any scan angle over the standard power amplifier spectrum.

2.5 Conclusion

A passive-scanned linear phased array is presented, using commercially available packaged RF MEMS switches for the tuning element. The presented measurements of high reliability, high power handling capabilities, and low loss properties insure that this design is an ideal candidate for base-station implementations in commercial and defense communications systems.

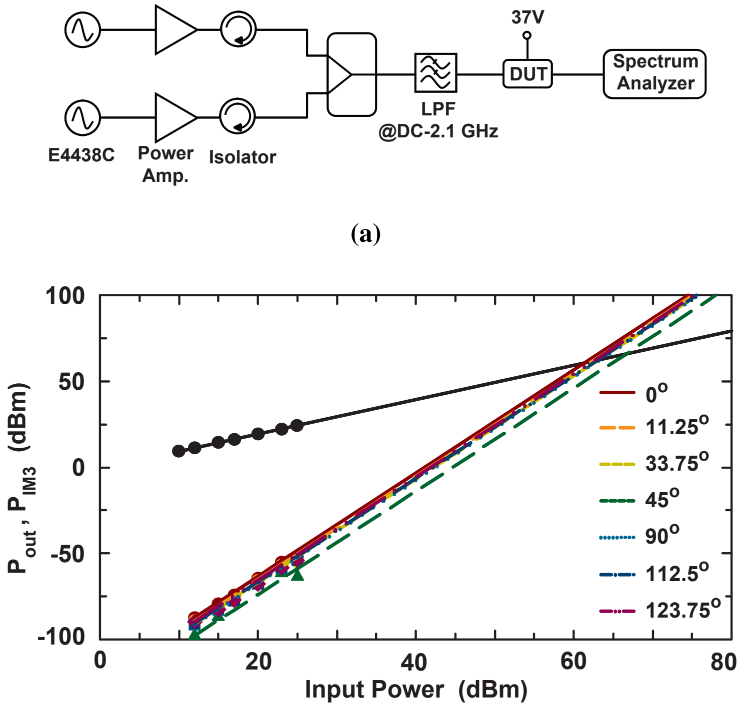

(a)

(b)

Figure 2.14: Measured IIP3 of the RF MEMS phase shifter: (a) measurement setup, and (b) measurement results at different phase states.

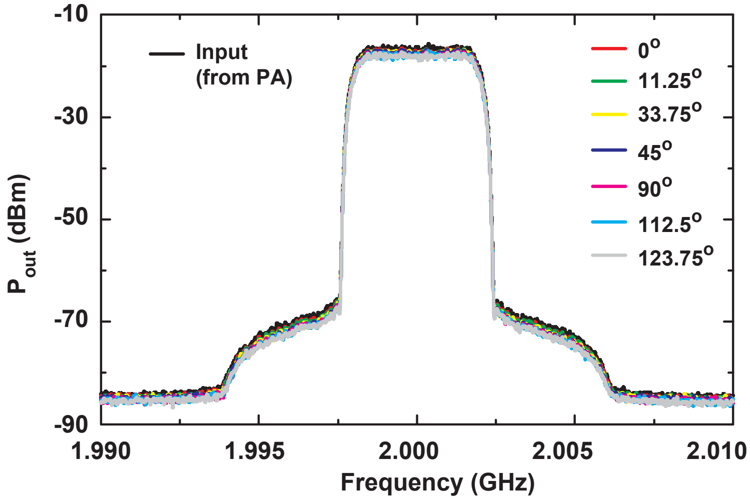

Figure 2.15: Measured linearity of the RF MEMS phase shifter: (a) IIP3, and (b) 30-dBm WCDMA signal, at different phase states.

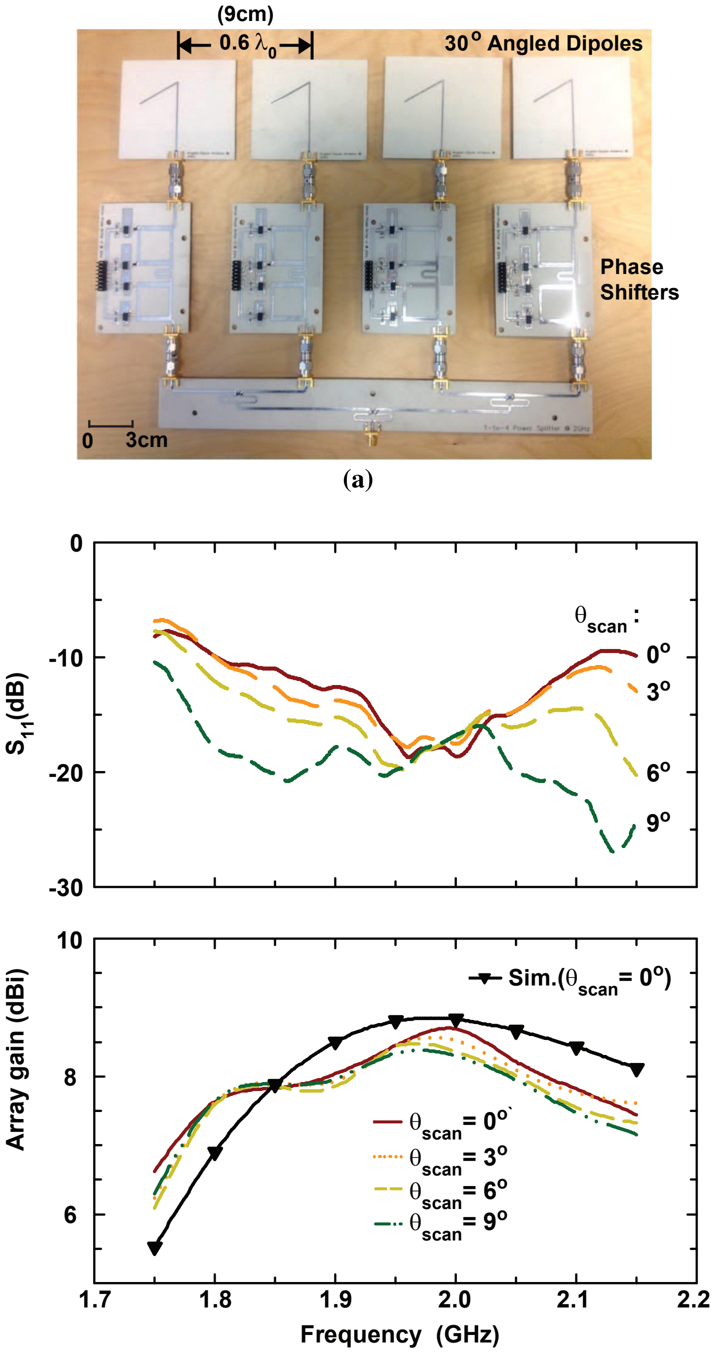

(a)

(b)

Figure 2.16: (a) Hardware realization of the 4-element phased array, and (b) measured response of phased array at various scan angles; (top) measured return loss, and (bottom) simulated and measured array gain.

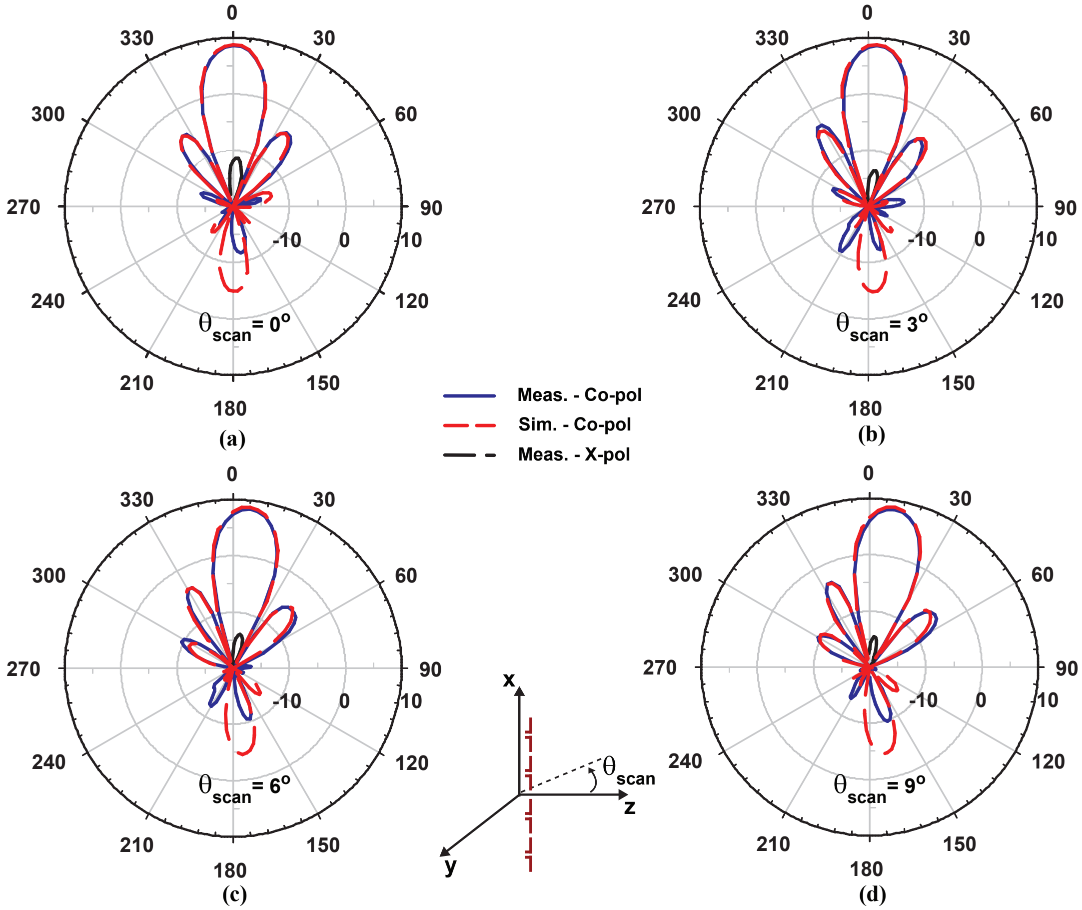

Figure 2.17: Measured and simulated radiation patterns of the antenna array at different scan angles.

2.6 Acknowledgements

The authors thank Rogers Corporation for providing the substrates, and Modelithics for providing the ADS models (CLR Library) for the surface mount passive components. The authors thank Dr. Allen Tran of Qualcomm Research and Development for the use of the Satimo chamber for the pattern measurements. Chih-Hsiang Ko and Kevin Ho thank Sansay Noimanivone and Earl Grad for their kind assistance rendered with the pattern measurements. The authors thank Siying Fu for use of the photograph in Fig. 2.1.

Chapter 2 is based on and mostly a reprint of the following paper: CH. Ko, K. M.J. Ho, and G. M. Rebeiz, "An Electronically-Scanned 1.8-2.1 GHz Base-Station Antenna Using Packaged High-Reliability RF MEMS Phase Shifters," *IEEE Trans. Microw. Theory Tech.*, vol. 61, no. 2, pp. 979-985, Feb. 2013.

Chapter 3

A 1.7-2.5 GHz Tunable 4-Pole Filter with Asymmetric Structure and Using Commercial 5-Bit RF MEMS Capacitors

3.1 Introduction

Tunable filters are an important research due to their potential to reduce the system complexity and cost for multi-standard communication systems [14]. They can be realized using Schottky diode varactors [5–13] and p-i-n diodes [4]. However, they suffer from high filter loss and low linearity, and most design cannot meet the high linearity or power handling requirement of modern communication systems. Tunable filters can also be implemented using ferroelectric devices [3], but these devices have a relatively low Q (30-50) which results in relatively high loss designs. Recently, RF MEMS (radio frequency micro-electro-mechanical-systems) devices are attracting a lot of attention due to their high-Q, high linearity, large power handling, and small size, all making them ideal elements for tunable filters in the 0.5-6 GHz range [50]. This has led to several demonstrations of tunable filters with RF MEMS devices [15–22]. However, all prior work used in-house MEMS devices, which are not packaged and suffer from reliability concerns.

RF MEMS technology is now entering a mature stage with commercial vendors offering packaged devices with high reliability and power handling. These include Omron and Radant MEMS for ohmic contact switches [23, 24], and wiSpry and Cavendish Kinetics for capacitive switches [25,26]. There are several reasons for using commercial devices, especially for switched capacitors: 1) Reliability since they are hermetically packaged, 2) uniformity between different chips since they are built in large numbers and on industrial processes and 3) ease of control since the devices have integrated voltage up-converters and SPI control.

This chapter presents the first tunable 4-pole filter built using commercial MEMS varactors, and demonstrates low loss and high linearity in modern communication bands. The work presents a new design method with an asymmetric filter structure so as to improve filter performance without adding extra tuners. An investigation of ENIG material (Electroless Nickel Immersion Gold) on top of the resonator and its effect on the resonator Q is presented. Also, comparing to the traditional symmetric combline filters, better insertion loss, linearity and power handling are shown. We also discuss the challenges and solutions required for the next generation RF MEMS devices implementing tunable filters.

3.2 Filter Design with RF MEMS Varactors

3.2.1 Device Properties

The 5-bit Cavendish Kinetics RF MEMS digital variable capacitors (DVC) are built on a 0.18 μm CMOS platform with integrated hermetic packaging and flip-chip bumps. The device includes the actual RF MEMS capacitor bank and the control circuits and a charge pump, as shown in Fig. 3.1. Due to the integration of the charge pump, the required supply voltage is only 1.8 V to operate the MEMS devices and therefore it's easily integrated into existing communication systems. There are two types of the DVCs used in this work : 32CK503S and 32CK402S [26].

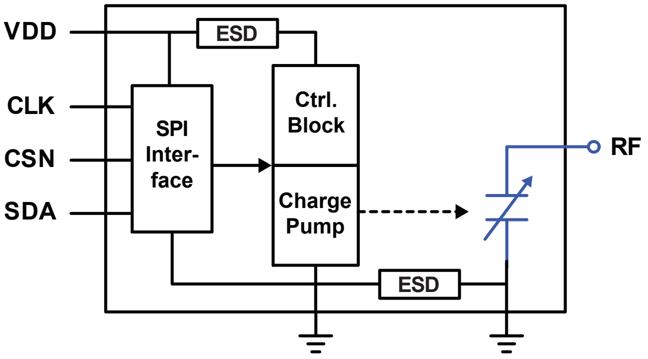

Figure 3.1: Blockdiagram of the Cavendish Kinetics RF MEMS capacitor.

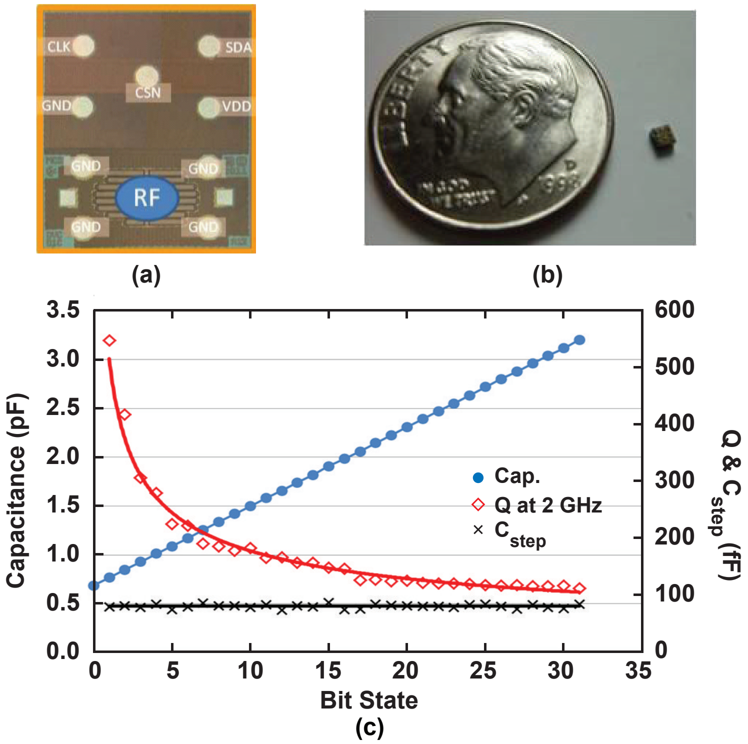

Figure 3.2: Cavendish Kinetics RF MEMS capacitor - 32CK503S : (a) the footprints, (b) the photo with the size of 1.6 x 1.35 mm^2 and (c) measured capacitance, Q and C_{step} vs. control state.

32CK503S

As shown in Fig. 3.2(b), the size of 32CK503S is 1.6 mm x 1.35 mm. The measured capacitance range and Q, referred to the board (including the bump paracitics), are shown in Fig. 3.2(c). A capacitance value of 0.6-3.3 pF is achieved over 32 states with a capacitance step of 84 fF. The measured mid-value Q is Q_{mid} = 150 at 2 GHz (C = 2 pF, X = -j40 Ω, R = 0.26 Ω). There is one interesting fact about this DVC : the DVC is not symmetrical, which means the device properties are different when looking at different nodes of the capacitor. The properties mentioned above are based on the input port of RF. However, if GND port is used as an input while grounding RF port, the Q drops dramatically even the capacitance doesn't change too much, as shown in Fig. 3.3. The measured IP3 of these devices is around +60 dBm in a 50 Ω set-up over the entire capacitance range and the maximum power handling is $\sim$36 dBm, which equals 40 V_{pp} in a 50-Ω system.

32CK402S

The structure and functionality of 32CK402S is as the same as 32CK503S but it has smaller physical size, capacitance tuning range and step size. The overall size is $<$ 1.5 mm x 1.5 mm and a capacitance value of 0.6-2 pF is achieved over 32 states with a capacitance step of 44 fF (Fig. 3.4) [51]. This smaller step-size is about half of 32CK503S and is more suitable for filter applications. The measured device Q is 400-100 at 2 GHz from state 0 to state 31. Also, the linearity has been improved comparing to 32CK503S and the measured IP3 of these devices is around 65-67 dBm in a 50 Ω set-up over the entire capacitance range.

3.2.2 Design and Measurement of Symmectric Tunable Filter

Fig. 3.5(a) presents the schematics of conventional symmetric tunable 4-pole combline filter. The shorted transmission line is loaded with a CK DVC with the model of 32CK503S in order to tune resonance frequency. The MEMS capacitors are compatible with a 1-mm-wide microstrip resonator due to their small size. The spacing between resonators can be determined by required coupling coefficient, M, which can

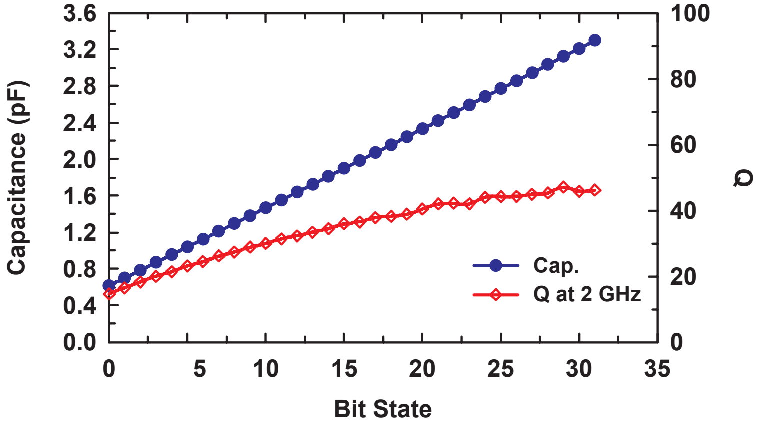

Figure 3.3: Measured capacitance and Q vs. control state of 32CK503S when the GND port used as an input.

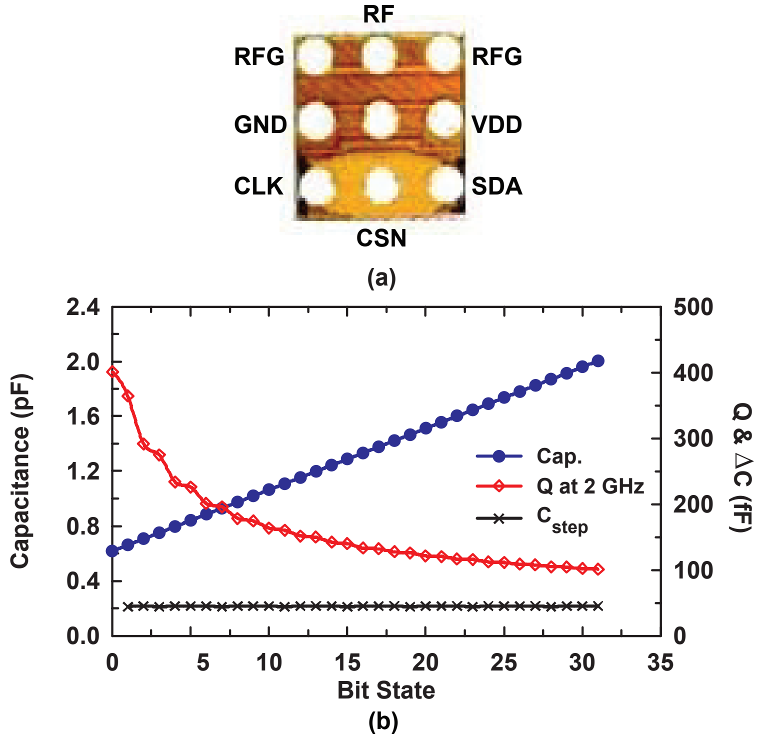

Figure 3.4: Cavendish Kinetics RF MEMS capacitor - 32CK402S : (a) the footprints of DVC with the size of 1.5 x 1.5 mm^2, used in the proposed asymmetric 4-pole tunable filters and (b) measured capacitance, Q and C_{step} vs. control state.

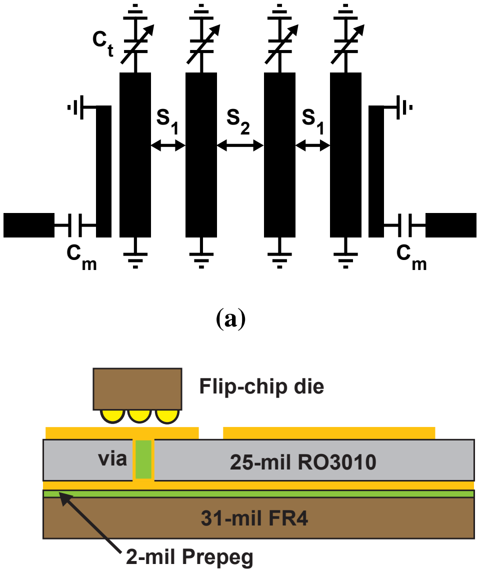

(a)

(b)

Figure 3.5: (a) Conventional symmetric tunable 4-port combline filter and (b) stack-up of circuit assembly.

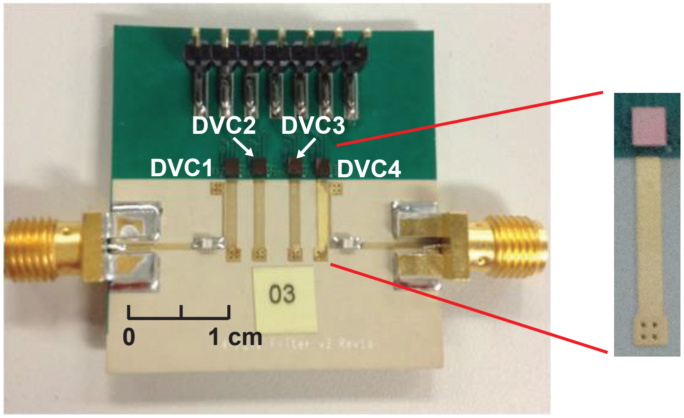

Figure 3.6: The photo of the 4-pole symmetric tunable combline filter.

be determined from [52]:

$$M_{i,i+1} = \frac{FBW}{\sqrt{g_i g_{i+1}}} \tag{3.1}$$

where g_i is the Chebychev low-pass coefficient. In order to achieve wideband matching, resonator 1 and 4 are coupled to the external ports using transmission line inverters and fixed input matching capacitors. The combline topology results in a compact layout and can be easily extended to elliptical filter topologies [53]. The filter is fabricated on 25-mil thick Rogers RO3010 with ε_r = 10.2, tanδ = 0.002 with 31-mil bare FR4 as physical support (Fig. 3.5(b)), and results in an unloaded resonator Q of $\sim$150 at 2 GHz (with surface roughness of 1.8 μm). Due to the requirement of flip-chip process for CK DVCs, an Electroless Nickel Immersion Gold (ENIG) is applied over the entire circuit (see Section 3.3 for detail). The photo of the completed symmetric 4-pole combline filter is shown in Fig. 3.6.

The measured frequency responses is shown in Fig. 3.7: the symmetric 4-pole filter operates at 1.5-2.4 GHz in 32 capacitor states and with a 1-dB fractional bandwidth of 5.9-2.8 % (89-68 MHz) and a filter loss of $\sim$6.6-5.8 dB at 1.5-2.4 GHz, respectively. The measured loss is 2.5 dB higher than simulations predict. There are the two real root causes of this higher loss being: 1. extra loss due to the ENIG finish as will be explained in Section 3.3; 2. the device to device capacitance variations that could not be fully compensated due to the use of a device with 84 fF step size resolution, which is not suitable for filters applications. Fig. 3.8(a) shows the effect of device uniformity on the frequency response at the lowest capacitance setting (f_0 = 2.4 GHz). It is seen from simulations that a loading capacitance variation of $\pm$42 fF (half of C_{step}) accurately predicts the distortion in the measured passband response at the highest frequency (DVC state = 0). The variation may not be solely from the devices, but could be from mounting the MEMS devices on the substrate and the exact placement of the bumps on the board. At higher capacitance settings and lower frequencies, it is possible to compensate this effect and improve the insertion loss by toggling some of the capacitance states by ±1 as seen in Fig. 3.8(b). For accurate filter design, it is important to have a finer capacitance step and a C_{step} of 20-40 fF is recommended for 1.5-2.5 GHz applications.

The measured insertion loss and filter response did not change for an input power

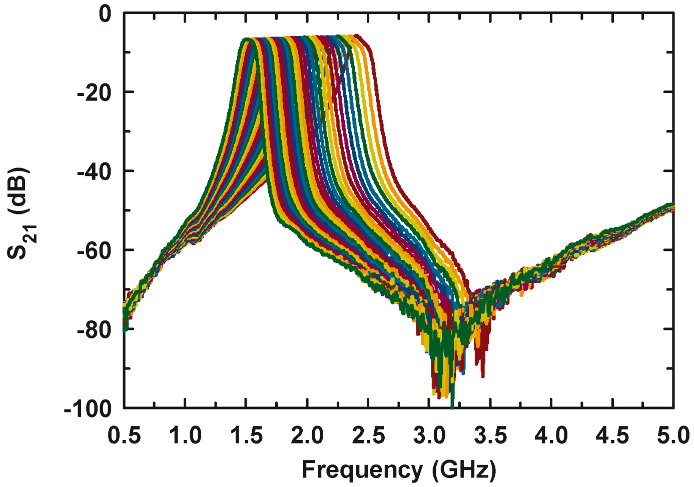

(a)

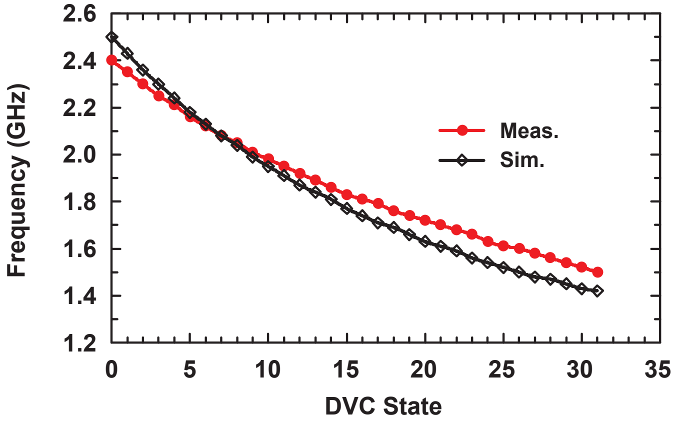

(b)

Figure 3.7: (a) Measured frequency response for 32 capacitance steps, and (b) measured and simulated center frequency of the 4-pole symmetric tunable combline filter.

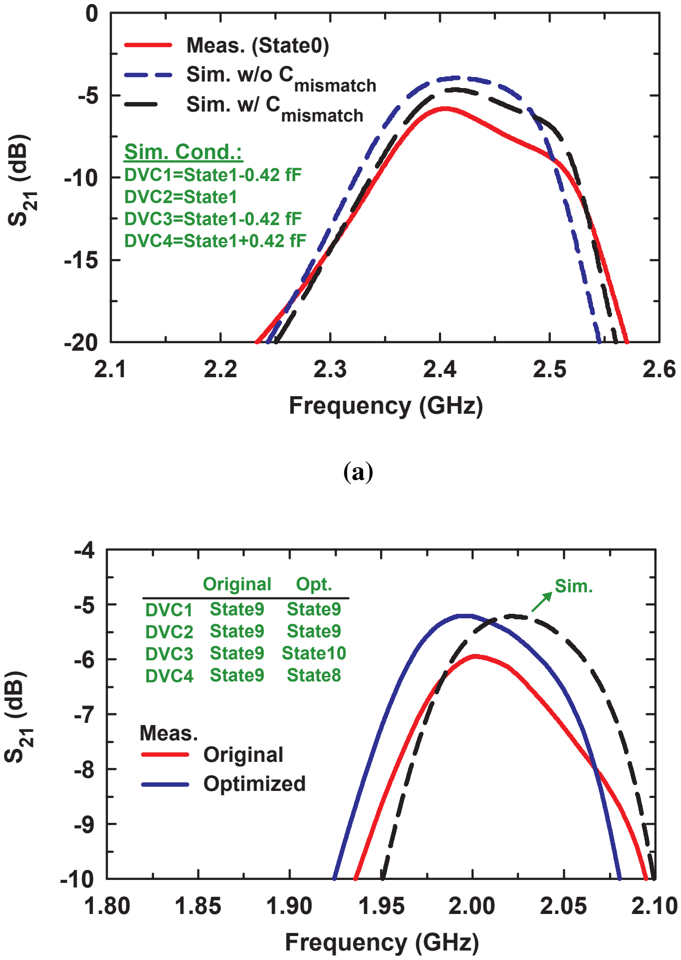

(a)

(b)

Figure 3.8: (a) The effect of $C_{mismatch}$ on the passband response, and (b) optimizing results by toggling the DVCs in measurements. Simulation done with $Q_{microstrip}$ = 120, the CK device model and the additional 0.3 Ω bump resistance.

of 0-20 dBm, which is much higher than Schottky diode filters which can only handle ∼10 dBm, even when using back-to-back diodes [54]. The measured second and third harmonic components were extremely low due to the great device linearity and filter attenuation at the upper frequencies. Fig. 3.9 shows the measured harmonic responses at 1.9 GHz (State 12) and at 17-dBm input power, the $2f_0$ and $3f_0$ components are -108 dBm and -125 dBm, resulting in -125 dBc and -142 dBc harmonic levels. The measured IP2 is basically infinite since the filter is capacitively coupled and the low-frequency components are blocked from leaving the filter. This is ideal for direct conversion systems which suffer from IP2 effects in the front-end. The measured IP3 is shown in Fig. 3.10 and is ∼33-35 dBm at all settings which is also very high for filters.

3.2.3 Design of Asymmetric Tunable Filter

The conventional tunable design resulted in a non-flat passband, and this is due to the filter parameters (Chebychev or elliptical response) being designed at one operating frequency. The frequency variation of the coupling coefficient, M, and external Q (Q_e) are shown in Fig. 3.11, and it is seen that M is constant v.s. frequency while Q_e changes from 15.5 to 10 at 1.7-2.4 GHz. For the same fractional bandwidth, M and Q_e should remain constant within the tuning range, and using fixed series matching capacitors at the input and output ports reduces the Q_e variation and improves the impedance matching over frequencies. With a gap of g = 8 mils in the input coupling structure, C_m = 4.7 pF reduces Q_e and results in less variation versus frequency (Fig. 3.12), which is better for a tunable bandpass filter with a constant fractional bandwidth. However, the input and output port capacitors result in a wide bandpass filter response and degrade the filter passband around the edges of the tuning range. This is shown in Fig. 3.13, where the S_{21} slope is steeper when using two matching capacitors instead of one and becomes larger versus frequency. This results in a non-ideal filter response, especially at the higher edge of the tuning range. A design with variable series matching capacitors does not suffer from this problem, but these capacitors are not available yet in RF MEMS technology.

In order to solve this, an asymmetric structure for the 4-pole tunable combline filter is proposed (Fig. 3.14). A single and fixed matching capacitor is used at the in-

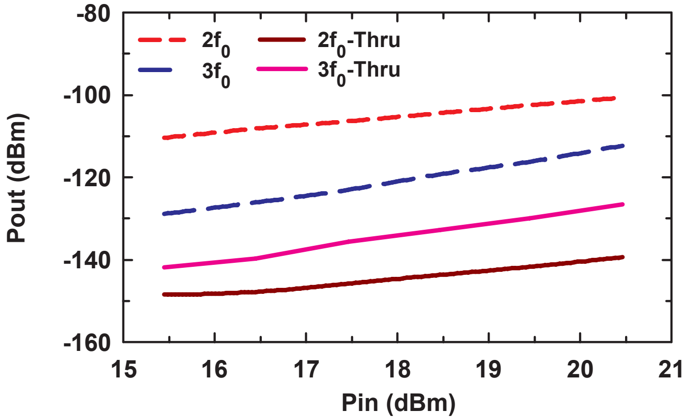

Figure 3.9: Measured second and third harmonic responses vs. power at 1.9 GHz (DVC: state 12).

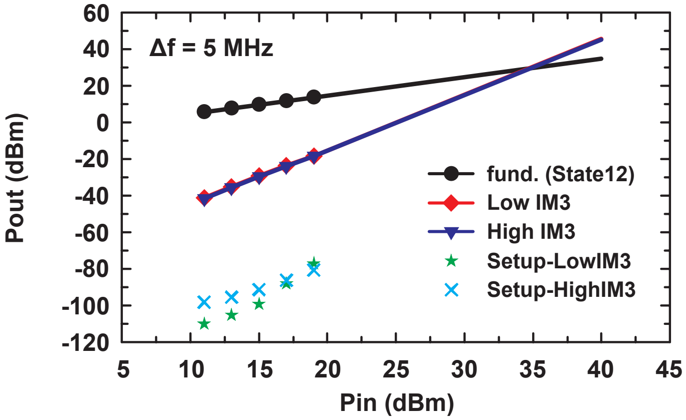

Figure 3.10: Measured IP3 at 1.9 GHz (DVC: state 12) with Δf = 5 MHz.

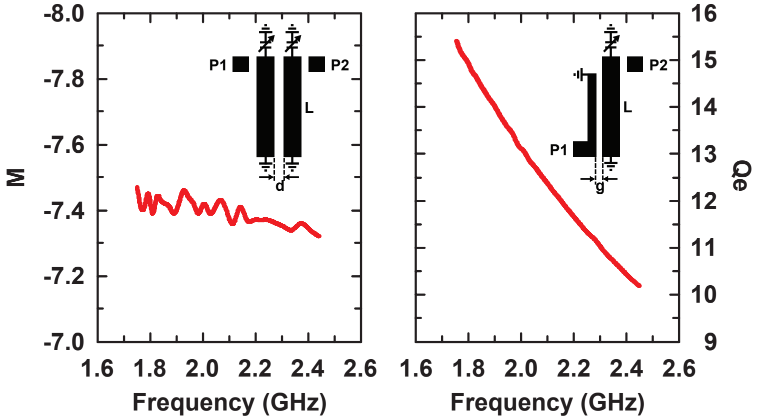

Figure 3.11: Variations of coupling coefficient and external quality factor versus tuning frequencies.

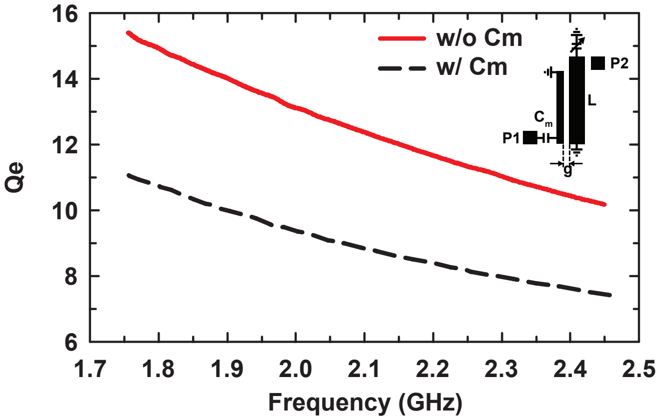

Figure 3.12: Effect of a matching capacitor on the external Q ($C_m = 4.7$ pF).

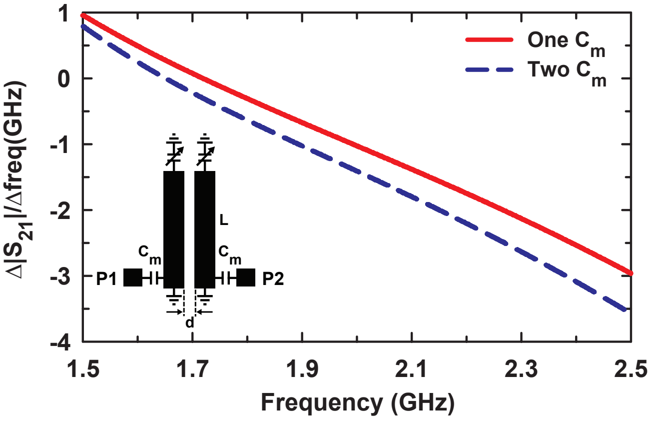

Figure 3.13: Comparison of the S_{21} slope between one and two matching capacitors.

Table 3.1: Structure Parameters of the Proposed Asymmetric 4-Pole Tunable Filter

L	W	S_1	S_2	S_3	L_e	W_e	g	C_m
290	32	56	68	52	290	16	8	4.7 pF

*Length Unit : mil

put port, and the spacing between resonators 1 and 2 is different from that between resonators 3 and 4 so as to compensate for the Q_e asymmetry and achieve impedance matching over the tuning range. It is well known that

$$Q_e = \frac{g_0 g_1}{FBW} \tag{3.2}$$

and from (3.2), the fractional bandwidth increases when Q_e decreases. Therefore, without a matching capacitor at the output port, the output Q_e cannot support the resulting wider fractional bandwidth as the input port does. One can reduce the gap in the output coupling structure to lower Q_e but this results in a non-feasible gap dimension. Also, the smaller the gap, the more sensitive Q_e is to the fabrication inaccuracies. One way to compensate for the fixed input capacitor is to optimize the spacing between each resonator. Since the structure needs to support a wider fractional bandwidth as it is tuned to higher frequencies, the coupling between resonators 3 and 4 should be increased by reducing the resonator spacing. Due to the frequency variation of Q_e, the reflection poles merge together and a relatively large reflection occurs in the passband while create degradation in the filter responses. This is shown in Fig. 3.15 for a 4-pole filter tuned far away from its center frequency, and only 2 reflection poles appear in the passband. However, if an asymmetric resonator spacing is applied and adjusted using Sonnet [1], the third pole appears and this improves the passband response. While this is not ideal for a 4-pole responses (as achieved with tunable series matching capacitors), it is much better than a two-pole response and results in an acceptable passband flatness over the tuning range. Therefore, in the asymmetric design, Q_e is compensated, and good frequency response is achieved over a wide frequency tuning range. Details of the proposed filter are in Table 3.1. The asymmetric 4-pole tunable filter is fabricated on 25-mil Rogers RT6010 (ε_r = 10.2, tanδ = 0.002) with 31-mil bare FR4 as support and ENIG as finish (Fig. 3.16).

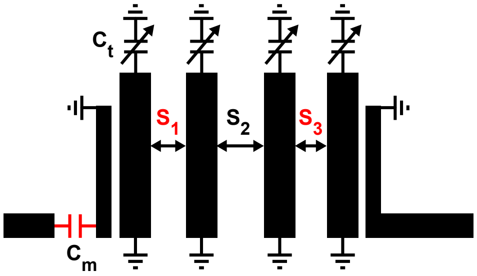

Figure 3.14: The proposed asymmetric tunable 4-pole combline filter.

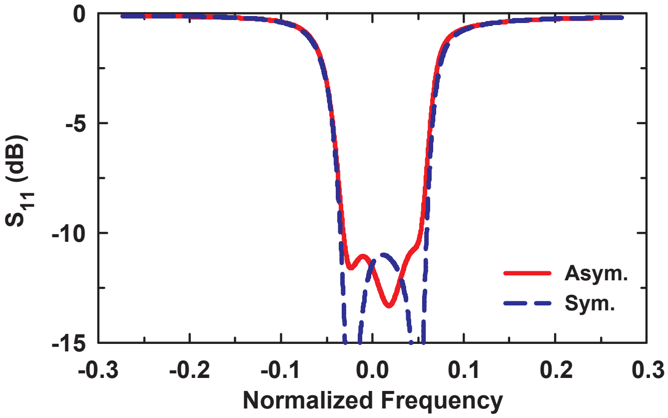

Figure 3.15: Pole placement between the asymmetric and symmetric structures.

3.3 Effect of Electroless Nickel Immersion Gold

Electroless nickel immersion gold (ENIG) is a metal finish on top of the copper trace to prevent from copper oxidization and is a requirement for wire-bonding and flip-chip process (Fig. 3.17(a)). The thickness of nickel and gold vary between PCB vendors, and is 3-6 μm for electroless nickel and a minimum of 0.05 μm for immersion gold [55]. At RF frequencies, the skin depth concentrates most of the current on the edges of metal lines, and this results in a large portion of the RF current passing through the nickel whose conductivity, σ, is less than one fourth of copper, 1.43x10^7 S/m. This increases the surface resistivity and decreases the transmission-line Q.

An experiment was done with the ENIG plated on the entire resonator (Cu+ENIG), or plated only on the tip of the resonator, just where the flip-chip device needs to be connected (Cu only). Fig. 3.17(b) presents the comparison of the measured unloaded resonator Q with and without ENIG. The Qu without ENIG is 193 at 3.92 GHz and 189 at 3.35 GHz and agrees well with simulations. However, the Qu drops to 117 at 3.3 GHz and 103 at 3.86 GHz for the case with ENIG. Also, the resonator frequency decreases because the effective dielectric constant increases slightly due to the ENIG coating. The resonator Qu decreases from 190 to 120, causing an additional 0.8-1 dB loss for a 4-pole filter with a FBW of 8%.

In reality, copper cannot be exposed to air and requires a surface finish to prevent oxidization. However, any kind of metal finish such as ENIG or HASL (Hot Air Solder Leveling) lowers the transmission line Q. As a result, in order to fabricate low-loss tunable filters, it is best to use a regular solder mask on the RF transmission lines before processing a metal finish, which is referred as Solder Mask On Bare Copper (SMOBC). The measured difference in filter loss between copper with and without a solder mask is $< \sim$0.1 dB at 1.5-2.5 GHz and there is almost no frequency shift.

3.4 Measurement

Fig. 3.18 presents the measured S-parameters for the proposed asymmetric tunable filter. The CK devices with tuning range of 0.6-2 pF and 44 fF step-size were controlled using the SPI interface and 32 different S-parameters were taken. The tuning

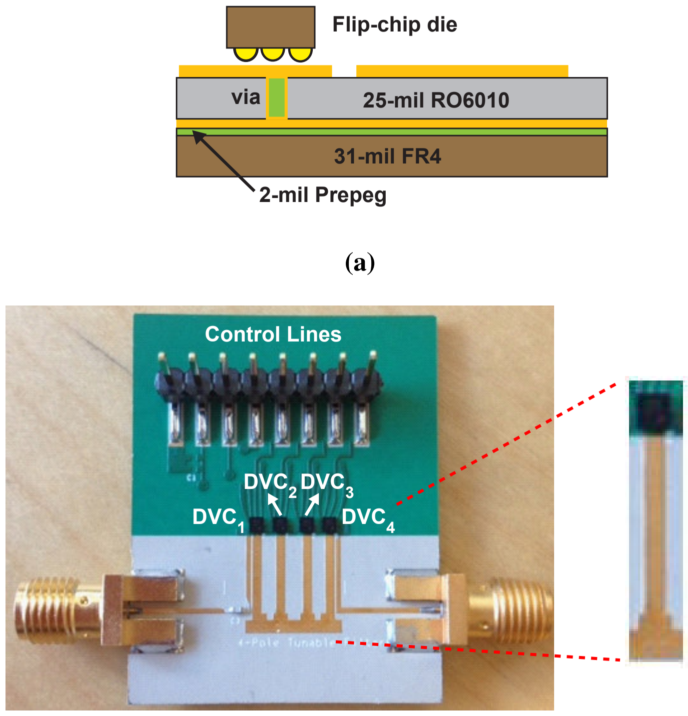

(a)

(b)

Figure 3.16: (a) Stack-up of circuit assembly and (b) Photo of the asymmetric 4-pole tunable filter.

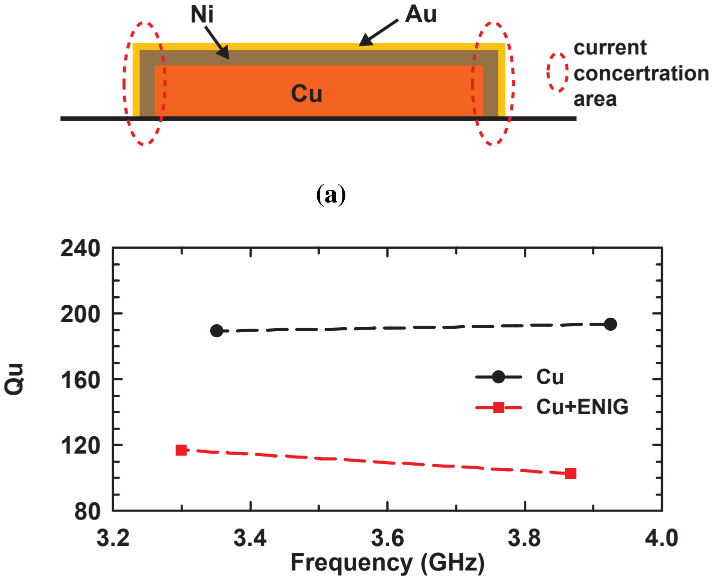

(a)

(b)

Figure 3.17: (a) Cross section of a copper transmission line with ENIG finish and (b) comparison of measured Qu with and without ENIG.

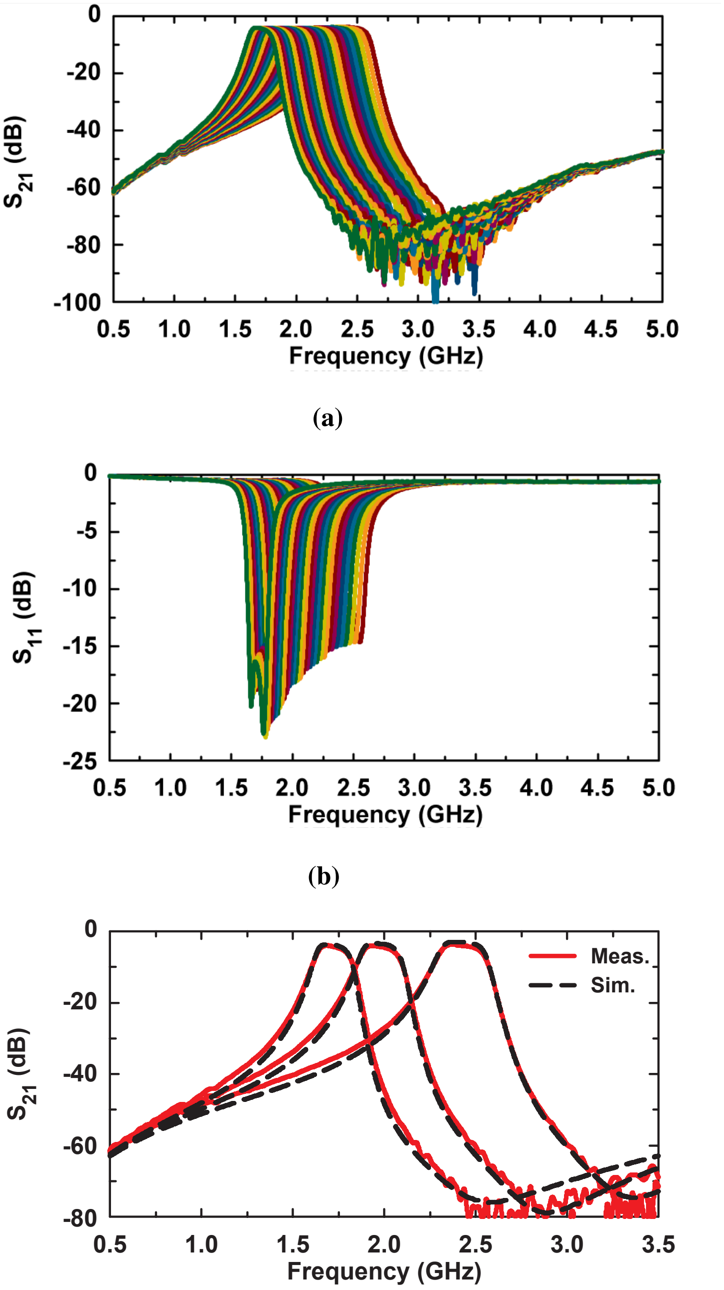

(a)

(b)

(c)

Figure 3.18: Measured (a) S_{11}, (b) S_{21}, and (c) comparison between measurements and simulations.

range is 1.7-2.45 GHz with insertion loss of 3.7-3.3 dB (with ENIG on it) and a 1-dB FBW of ~8%. The measured S_{11} is $<$ -10 dB for all states and the stopband rejection is $>$ 50 dB up to 5 GHz. Measurements agree very well with simulations (Fig. 3.18(c)), and the flatness of the measured passband is much better than the conventional symmetric design presented in Section 3.2.2(Fig. 3.19). This is due to the improved asymmetric structure and to the 42 fF capacitance step which reduces the mismatch between the different devices and alleviates the requirement of tweaking the states between the four CK DVCs to optimize the loss (Section 3.2.2).

Additional measurements are shown in Fig. 3.20. The measured tuning range with bare copper agrees well with the simulations while that of the case with ENIG shifts a bit lower due to the increase in the effective dielectric constant. The difference between the 1-dB fractional bandwidth is $< 0.5\%$, which is due to component and assembly variations. The insertion loss can be predicted using the standard formula [52]:

$$IL(dB) = 4.343 \sum_{i=1}^{n} \frac{g_i}{\Delta Q_{ui}} \tag{3.3}$$

where Δ and Q_{ui} are the fractional bandwidth and unloaded resonator Q. At 2 GHz, the loaded transmission-line resonator has Q of ~84 ($Q_{\text{t-line}}$ = 190 and Q_{DUT} = 150), which introduces ~2.5 dB insertion loss for a 4-pole filter with FBW of 8%. However, the measured loss is approximately 1 dB higher than the predicted value due to ENIG finish. Fig. 3.20(c) presents the effect of ENIG on the asymmetric tunable 4-pole filter. The loss is improved by 1 dB at 2.4 GHz (lower capacitive states, higher device Q) and 0.7 dB at 1.75 GHz (higher capacitive states, lower device Q) with the removal of the ENIG layer above the resonator. The average loss improvement is 0.8 dB, and the measured loss without ENIG agrees well with simulations.

The measured filter gain versus input power is shown in Fig. 3.21, at low and high capacitive loading. Only two states are presented here since they can describe the best and worse cases. However, the 1-dB compression point cannot be seen up to 28 dBm. The small gain variation of $<$ 0.1 dB is due to the accuracy of the power meter. The measured second and third harmonic components are extremely low due to the high-linearity devices and filter attenuation at the upper frequencies (Fig. 3.22). In fact, with an input power of 20 dBm, for f_0 = 1.7 GHz (state 31), the $2f_0$ and $3f_0$ components

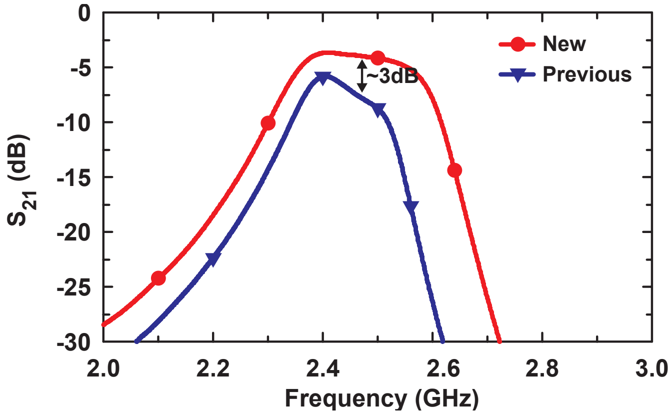

Figure 3.19: Passband comparison between the asymmetric and the conventional symmetric filters.

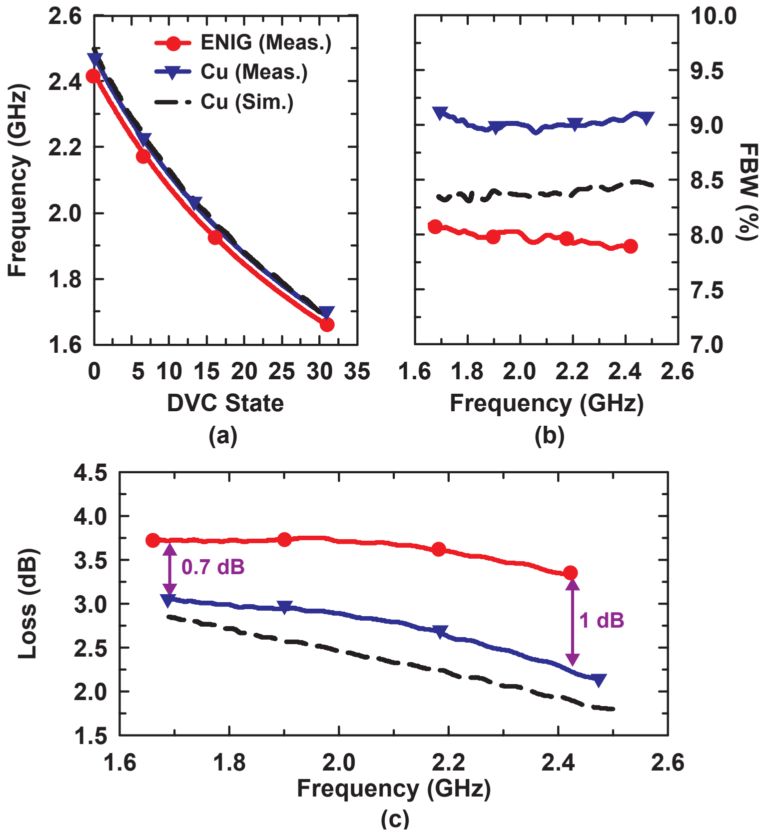

Figure 3.20: Comparison between measurements and simulations: (a) tuning range, (b) 1-dB fractional bandwidth and (c) loss at 32 capacitance steps.

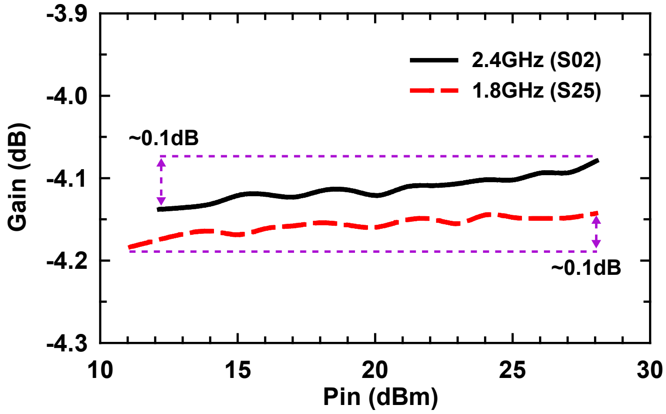

Figure 3.21: Measured input P1dB at 1.8 GHz and 2.4 GHz.

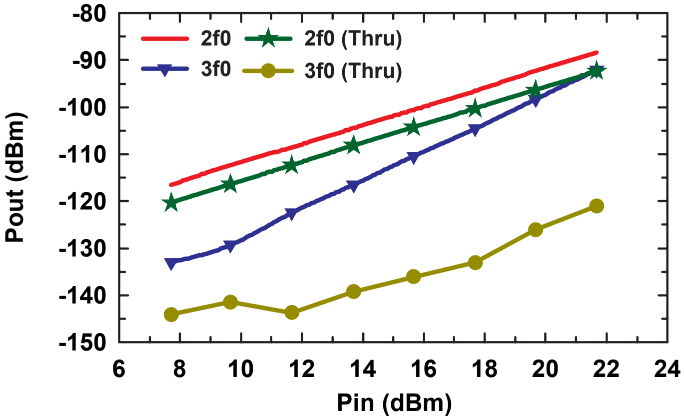

(a)

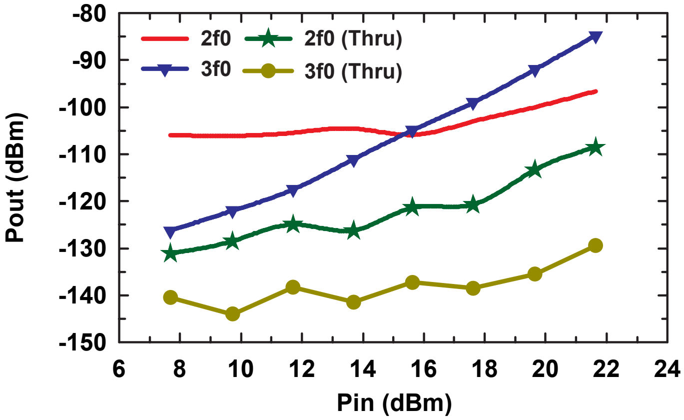

(b)

Figure 3.22: Measured 2nd and 3rd harmonic components at (a) 1.7 GHz and (b) 2.5 GHz.

are -92 dBm and -98 dBm, resulting in -112 dBc and -118 dBc harmonic levels, respectively, and for f_0 = 2.5 GHz (state 0), the $2f_0$ and $3f_0$ components are -100 dBm and -92 dBm, resulting in -120 dBc and -112 dBc harmonic levels. The measurement of second harmonic components was actually limited by the setup (RBW = 1 Hz, att. = 10 dB and avg. = 10). The filter provides high rejection level at $2f_0$ (3.4-5 GHz), and hence the measured power level of the second harmonic component is close to the setup limit. There was no problem in measuring the third harmonic component.

The measured IP2 is basically infinite since the filter is capacitively coupled and the low-frequency components are blocked from leaving the filter. This is ideal for direct conversion systems which suffer from IP2 effects in the front-end. The measured IP3 is shown in Fig. 3.23. If the two-tone separation is larger than the filter bandwdith, the IP3 is very high since one or two fundamental signals are rejected at the filter input. Therefore, a frequency separation of 10 MHz is used, which results in both signals and the intermodulation signals in the passband and is the worst-case situation for linearity measurements. The IIP3 is 46 dBm at 1.7 GHz (state 31) and is 61 dBm at 2.5 GHz (state 0), which is very high for a tunable filter and at least 20 dB higher than using varactor diodes. At 1.7 GHz, the IP3 is worse due to the higher filter loading. The effect of frequency of separation is shown in Fig. 3.23(c). When the separation is larger, the IP3 is improved.

The measured filter IP3 is lower than the device specification, which is 65-67 dBm in a 50-Ω setup. Fig. 3.24(a) presents the simulated voltage distribution at the four MEMS capacitor terminals in the asymmetric 4-pole tunable filter. When the input power is 25 dBm, which is 4 V_{rms} at the input of the filter, the *rms* voltage across the DVC is 9.2-14.5 V, which is at least twice of the input voltage. This voltage amplification is typical in filters, resulting in a lower IP3. Fig. 3.24(b) presents the mechanism that effectively amplifies the input voltage to a higher voltage on the device. The inverters between two resonators can be simplified for the analysis as a load with an inverter. For a lossless system, and $P_{in} = P_L$,

$$P_{in} = |V_{in}|^2 \, |Y_{in}| = |V_L|^2 \, |Y_L| = P_L \tag{3.4}$$

$$Y_{in} = \frac{J^2}{Y_L} \tag{3.5}$$

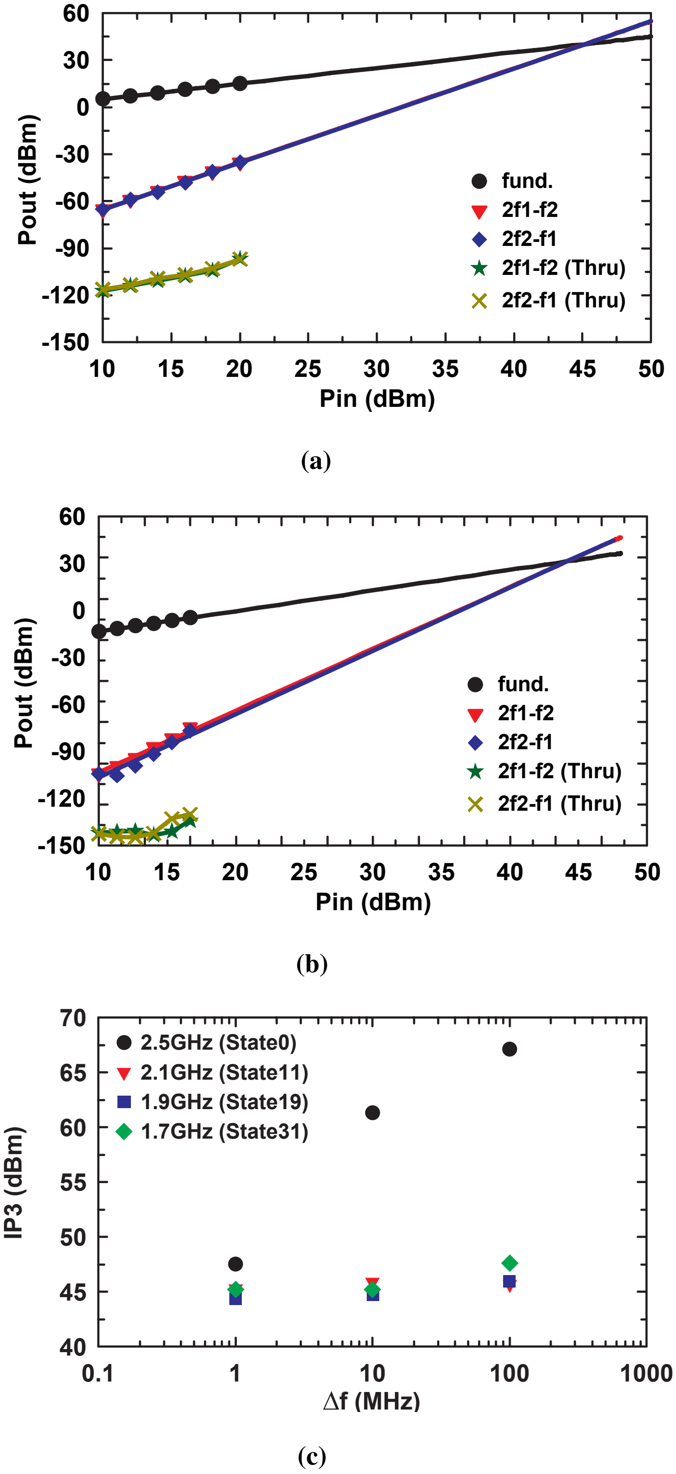

Figure 3.23: Measured IP3 with a frequency separation of 10 MHz at (a) 1.7 GHz, (b) 2.5 GHz and (c) IP3 versus Δf.

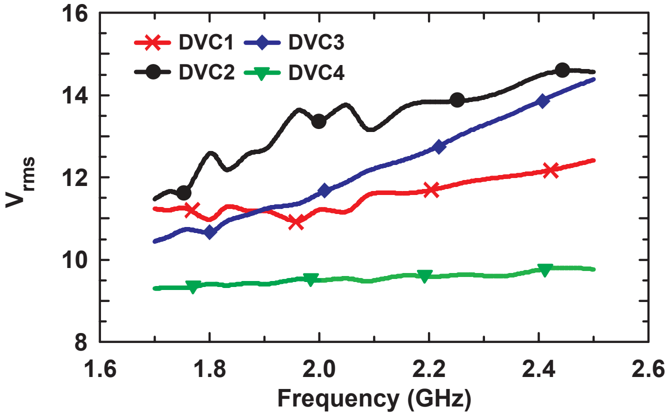

(a)

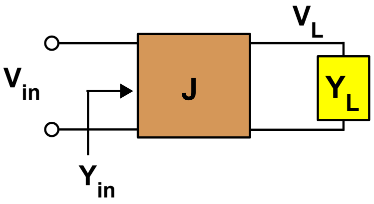

(b)

Figure 3.24: (a) Simulated *rms* voltage across the DVC terminals vs. different state setting (or filter frequencies) for an input power of 25 dBm. (b) Explanation of voltage amplification due to the inverter.

Therefore,

$$V_L = \sqrt{\frac{|Y_{in}|}{|Y_L|}}\,|V_{in}| = \frac{J}{|Y_L|}\,|V_{in}| \tag{3.6}$$

At resonance, $|Y_L| = G_L$.

$$|V_L| = \frac{J}{G_L}\,|V_{in}| \tag{3.7}$$

If $\mathrm{Q_L}$ is relatively high, $\mathrm{J} > \mathrm{G_L}$ and therefore $|\mathrm{V_L}| > |\mathrm{V_{in}}|$, which means the voltage at the load is amplified by $\mathrm{J/G_L}$.

A better way to show the effect of the filter non-linearity is to measure the spectral regrowth for a complex signal such as a 5-MHz wideband CDMA waveform (Fig. 3.25). It is seen that the ACPR is $\sim$54 dB for an input power of 25 dBm at 1.7 GHz (state 31), and non-measurable for 2.5 GHz (state 0) (in this case, the spectral regrowth is all due to the power amplifier). In general, for W-CDMA signals, GaAs or CMOS cell phone power amplifiers have an ACPR of 36-40 dB, and therefore, the tunable filter will not contribute any additional distortion.

The linearity measurements show that RF MEMS tunable filters can meet the very tough linearity specifications which are present in modern-day communication systems.

3.5 Conclusion

This chapter has demonstrated a 1.7-2.5 GHz asymmetric 4-pole tunable filter with high linearity and high power handling using the Cavendish Kinetics RF MEMS capacitors. The filter can meet the linearity, ACPR and harmonic specifications of modern multi-band wireless front-ends. The asymmetric structure improves the passband flatness of a tunable filter. In addition, a RF MEMS varactor with capacitance step of 20-40 fF is recommended for 1.5-2.5 GHz tunable filter application. Finally, the effect of ENIG is explained and demonstrated and using solder mask to prevent additional loss from metal finish is also suggested.

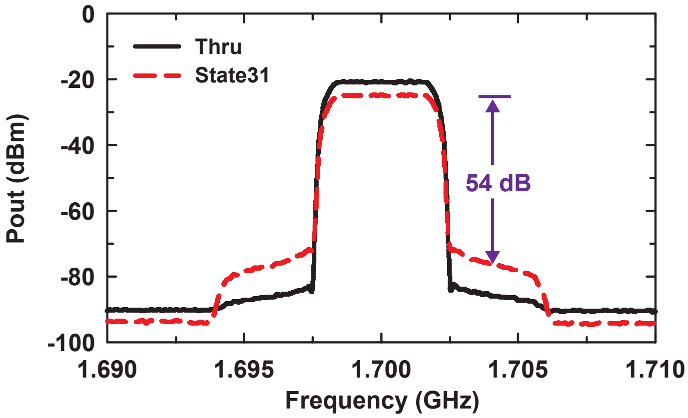

(a)

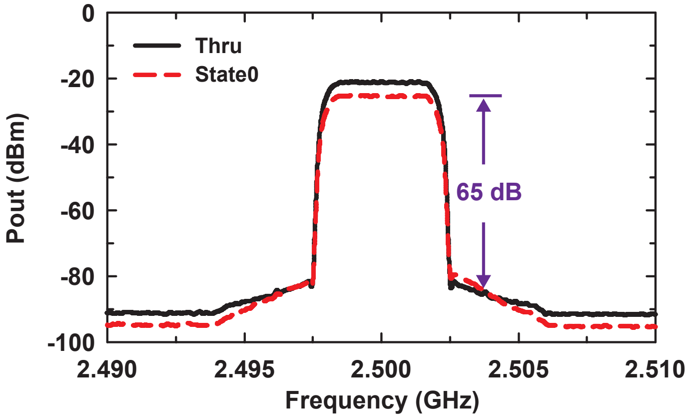

(b)

Figure 3.25: Measured spectral regrowth at 25 dBm for a 5-MHz WCDMA signal at f_0 = (a) 1.7 GHz and (b) 2.5 GHz.

3.6 Acknowledgements

The authors thank Rogers Corporation for providing the substrates. The authors thank Cavendish Kinetics for providing RF MEMS DVCs and its electrical model.

Chapter 3 is based on and mostly a reprint of the following papers: CH. Ko, K. M.J. Ho, R. Gaddi and G. M. Rebeiz, "A 1.7-2.5 GHz Tunable 4-Pole Filter with Asymmetric Structure and Using Commercial 5-Bit RF MEMS Capacitors," submitted for publication in *IEEE Trans. Microw. Theory Tech.*, Jun. 2014.

Chapter 4

A 1.4-2.3 GHz Tunable Diplexer Based on Reconfigurable Matching Networks

4.1 Introduction

communication systems have been growing at a fast rate, and several additional frequency bands are being considered. In order to serve all the frequencies, an antenna-switch-module is used and connects a large number (n = 6-12) filters and diplexers to the antenna [56–58]. However, this occupies a large amount of circuit area, especially if the filters are not BAW or SAW type. Recently, RF tunable circuits have progressed at a fast rate and tunable solutions are now considered due to their potential of reducing the system size and complexity. There are numerous papers about tunable filters and tunable antennas using different tuner technology [59–63], but very few are related to tunable diplexers (Fig. 4.1). For frequency-domain duplexing communication systems, a diplexer is a key component to separate the transmitting and receiving signals from the antenna [64]. A tunable diplexer is proposed in [65], and is based on two bandpass filters and additional lowpass and highpass filters but its tuning range is very narrow. A tunable transmission line is also employed for realizing a tunable diplexer as shown in [66]. However, in this structure, the tuning range is limited by number of transmission lines, which occupies large circuit area. Dual-mode filters were also used in tunable diplexers but the tuning range was very small [67]. Common-resonator method was used in [68] for a tuanble diplexer. However, the two bandpass frequencies were required to be relatively far apart which is not compatible with many wireless communication standards.

In this chapter, reconfigurable matching networks are used to achieve a tunable diplexer. A tunable diplexer with two tunable 3-pole combline filters and a reconfigurable pi-model matching networks is demonstrated. Both filters can be tuned independently, and by using the reconfigurable matching networks, the passband responses can be placed very close to each other without deterioration. Analysis and design information is presented, together with measurements.

4.2 Design Principle of a Tunable Diplexer

Fig. 4.2(a) presents the schematic of a 3-pole combline filter [52], which is used in a tunable diplexer. The equivalent values of lumped elements are

$$C = \frac{Q_e}{\omega_0 Z_0} \tag{4.1}$$

$$L = \frac{Z_0}{\omega_0 Q_e} \tag{4.2}$$

$$J_{i,i+1} = \frac{Z_0}{Q_e M_{i,i+1}} \tag{4.3}$$

where Q_e is the external quality factor at input and output and $M_{n,n+1}$ are the coupling coefficient between resonators, defined as:

$$Q_e = \frac{g_0 g_1}{FBW} \tag{4.4}$$

$$M_{i,i+1} = \frac{FBW}{\sqrt{g_i g_{i+1}}} \tag{4.5}$$

for i = 1 to n-1, where g_i are the standard lowpass-filter parameters and FBW is the 3-dB fractional bandwidth. Usually, filter design takes into account only the input impedance around the passband frequencies. However, in order to combine two filters into a diplexer without affecting each other, the input impedance out of band frequencies is critical. As shown in Fig. 4.2(b), the input impedance is close to a short circuit at the stopband frequencies, which means two such filters cannot be combined together without a specific matching network.

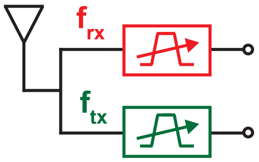

Figure 4.1: A tunable diplexer using two different tunable filters.

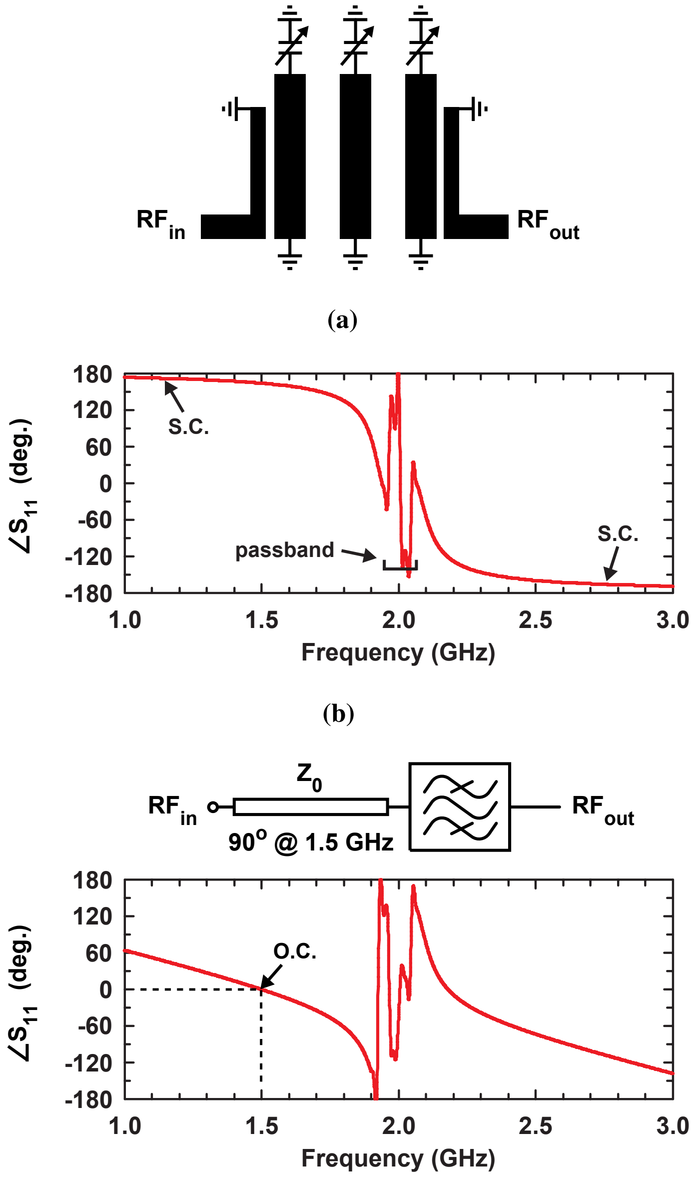

(a)

(b)

(c)

Figure 4.2: (a) Schematic of a 3-pole combline filter, (b) phase response of a 2 GHz 3-pole filter and (c) Effect of a 90^o transmission line in front of a filter.

The simplest way to combine two bandpass filters into a diplexer is to design a bandpass filter with an open circuit impedance profile at the rejection band. For a combline design, the input impedance can be transformed into an open circuit, using a 90^o transmission line as shown in Fig. 4.2(c). In this case, the input impedance becomes open circuited at the rejection frequencies, while the passband response is unchanged. Based on this idea, the simulated response of a diplexer is shown in Fig. 4.3 with two 90^o transmission lines added at 1.5 GHz and 2 GHz to the receive and the transmit filter, respectively. There is almost no difference in the frequency response between the diplexer and the two stand-alone filters.

For a tunable diplexer, the two bandpass filters and also the 90^o transmission line should be tunable, and a lumped-element implement of the 90^o line is used. The equivalent L and C can be calculated as [69]:

$$L = \frac{Z_0}{\omega_0} \tag{4.6}$$

$$C = \frac{1}{Z_0 \omega_0} \tag{4.7}$$

A comparison between a 50-Ω 90^o transmission line and its equivalent circuit (L = 4.42 nH, C = 1.1-2.5 pF) at different center frequencies is shown in Fig. 4.4. By changing the capacitance value, a tunable 90^o phase delay can be achieved, and will transform the short circuit into an open circuit over a wide frequency range. The equivalent circuit is a third-order lowpass filter, and therefore it limits operating bandwidth at the high frequency side. As a result, if the separation between the two operating frequencies in the diplexer is large, the passband at the higher frequency will encounter additional loss due to this lowpass effect.

4.3 Analysis of a Tunable Diplexer with Tunable Matching Networks

A tunable diplexer with two bandpass filters cascaded with tunable matching networks is shown in Fig. 4.5. The scattering matrix of a bandpass filter cascaded with a tunable matching network (S^{RX} or S^{TX}) is obtained from the scattering matrices of the

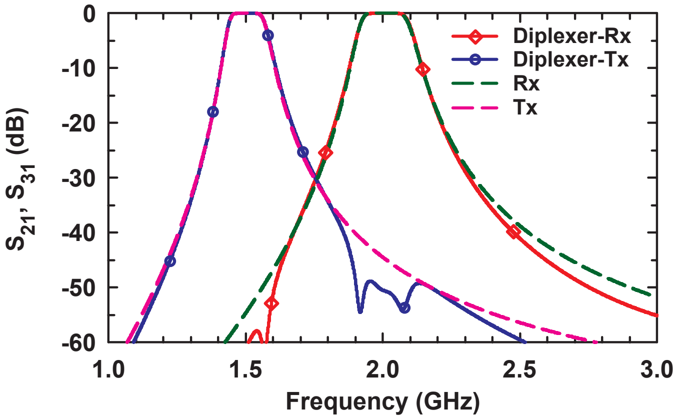

Figure 4.3: Response comparison between a diplexer and two individual bandpass filters.

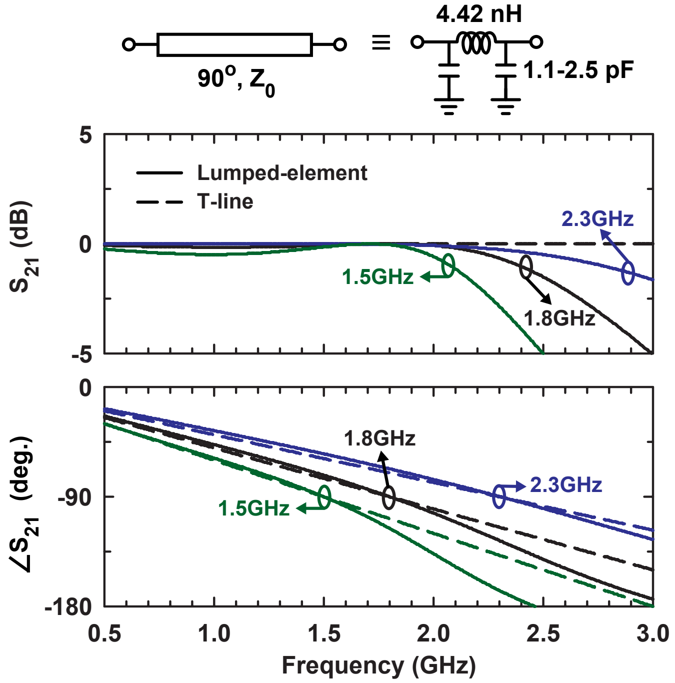

Figure 4.4: Lumped-element equivalent circuit of a quarter-wave microstrip line and simulated amplitude and phase versus frequency.

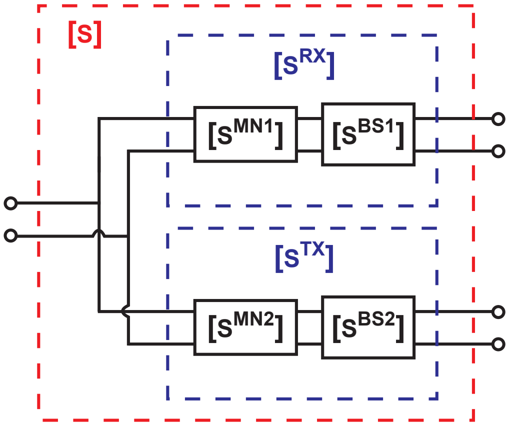

Figure 4.5: S-parameter model for the tunable diplexer.

separated matching network ($\mathrm{S^{MN}}$) and bandpass filter ($\mathrm{S^{BP}}$) [70].

$$\left[S^{RX}\right] = \begin{bmatrix} S_{11}^{RX} & S_{12}^{RX} \\ S_{21}^{RX} & S_{22}^{RX} \end{bmatrix}$$

$$= \begin{bmatrix} S_{11}^{MN1} + \frac{S_{12}^{MN1} S_{21}^{MN1} S_{11}^{BP1}}{1 - S_{22}^{MN1} S_{11}^{BP1}} & \frac{S_{12}^{MN1} S_{12}^{BP1}}{1 - S_{22}^{MN1} S_{11}^{BP1}} \\ \\ \frac{S_{21}^{MN1} S_{21}^{BP1}}{1 - S_{22}^{MN1} S_{11}^{BP1}} & S_{22}^{BP1} + \frac{S_{12}^{BP1} S_{21}^{BP1} S_{22}^{MN1}}{1 - S_{22}^{MN1} S_{11}^{BP1}} \end{bmatrix} \tag{4.8}$$

where

$$\left[S^{MN1}\right] = \begin{bmatrix} S_{11}^{MN1} & S_{12}^{MN1} \\ S_{21}^{MN1} & S_{22}^{MN1} \end{bmatrix} \text{ and } \left[S^{BP1}\right] = \begin{bmatrix} S_{11}^{BP1} & S_{12}^{BP1} \\ S_{21}^{BP1} & S_{22}^{BP1} \end{bmatrix}$$

$\mathrm{S^{TX}}$ can be derived by replacing $\mathrm{S^{MN1}}$ and $\mathrm{S^{BP1}}$ with $\mathrm{S^{MN2}}$ and $\mathrm{S^{BP2}}$, respectively. Considering the ideal case at the receiver branch ($\mathrm{S^{RX}}$), for a matched 90$^{\mathrm{o}}$ transmission line at $\mathrm{f_{tx}}$, $\mathrm{S_{11}^{MN1}}$ = $\mathrm{S_{22}^{MN1}}$ = 0 at all frequencies and $\mathrm{S_{21}^{MN1}}$ = $\mathrm{S_{12}^{MN1}}$ = -j at $\mathrm{f_{tx}}$. From (4.8), at the passband, $\mathrm{S_{11}^{BP1}}$ = 0, $\mathrm{S_{11}^{RX}}$ = 0, and the filter response is not affected by the matching network. At the rejection frequency of $\mathrm{f_{tx}}$, $\mathrm{S_{11}^{BP1}}$ = -1, $\mathrm{S_{11}^{RX}}$ = 1. The matching network transforms a short circuit to an open circuit at $\mathrm{f_{tx}}$. The transmission coefficient, $\mathrm{S_{21}^{RX}}$, can be understood easily in dB as:

$$S_{21dB}^{RX} = S_{21dB}^{MN1} + S_{21dB}^{BP1} - 20\log(|1 - S_{22}^{MN1} S_{11}^{BP1}|) \tag{4.9}$$

This shows that, as expected, the overall filter insertion loss is affected by the matching network transmission coefficients even if the filter is well-matched ($\mathrm{S_{11}^{BP1}}$ = 0).

The overall diplexer scattering matrix can be calculated as a parallel circuit comprised of [$\mathrm{S^{RX}}$] and [$\mathrm{S^{TX}}$]:

$$S_{11} = \frac{2S_{11}^{RX}(1 + S_{11}^{TX}) - (1 - S_{11}^{TX})(1 + S_{11}^{RX})}{2(1 + S_{11}^{TX}) + (1 - S_{11}^{TX})(1 + S_{11}^{RX})} \tag{4.10}$$

$$S_{21} = \frac{2(1 + S_{11}^{TX})}{2(1 + S_{11}^{TX}) + (1 - S_{11}^{TX})(1 + S_{11}^{RX})} S_{21}^{RX} \tag{4.11}$$

$$S_{31} = \frac{2(1+S_{11}^{RX})}{2(1+S_{11}^{TX})+(1-S_{11}^{TX})(1+S_{11}^{RX})} S_{21}^{TX} \tag{4.12}$$

and is dominated by the input impedance of each branch. Without the matching network, $\mathrm{S}_{11}^{\mathrm{RX}}$ = -1 at f_{tx} and $\mathrm{S}_{11}^{\mathrm{TX}}$ = -1 at f_{rx}, and as a result, S_{11} = -1 and S_{21} = S_{31} = 0 at both frequencies.

Fig. 4.6 presents the equivalent circuit of the proposed tunable diplexer. The filter design values are found using (4.1)-(4.3) by substituting f_{rx} and f_{tx}. In practice, only capacitors can be tuned, and $\mathrm{L}_{\mathrm{trx}}$ and $\mathrm{L}_{\mathrm{ttx}}$ are fixed. The effect of tunable matching network will be investigated by calculating the diplexer response a) with tunable matching networks and b) with fixed matching networks. The case without any matching networks is not investigated since $\mathrm{S}_{11} \sim$ -1 for the combline filter (at out of band). The third-order bandpass filters are designed to operate from 1.4 GHz to 2.3 GHz and have 5% fractional bandwidth with passband ripple of 0.01 dB and an unloaded quality factor of 1000. This high value of Q_{u} is selected so as to clearly see the effect of the matching network on the diplexer insertion loss. The component quality factor is set to be 1000 at 1 GHz for both capacitors and inductors in matching networks.

The closet frequency separation of a diplexer is defined at the -3-dB intercept points of the two filters. At this frequency, each filter input impedance is rapidly changing and therefore is difficult (and not practical) to use matching networks to match the two filters simultaneously. Fig. 4.7 presents the tunable diplexer operating at f_{rx} = 2.3 GHz and f_{tx} = 2.1 GHz with matching networks at 2.3 GHz and 2.1 GHz, respectively (see Table 4.1 for component values). With the C-L-C matching networks, the diplexer is well-matched at both passbands and the responses are very close to individual filters even when two operating frequencies are close to each other. The insertion loss difference between the diplexer and stand-alone filters is $<$ 0.05 dB. If the same matching networks are used when f_{tx} changes to 1.4 GHz, the frequency response at 1.4 GHz is greatly degraded, as shown in Fig. 4.7(b). At 1.4 GHz and for $\mathrm{S}_{11}^{\mathrm{TX}}$ = 0, from (4.10) and (4.12),

$$S_{11} = \frac{S_{11}^{RX}-1}{S_{11}^{RX}+3} \tag{4.13}$$

$$S_{31} = \frac{2(1+S_{11}^{RX})}{S_{11}^{RX}+3} S_{21}^{TX} \tag{4.14}$$

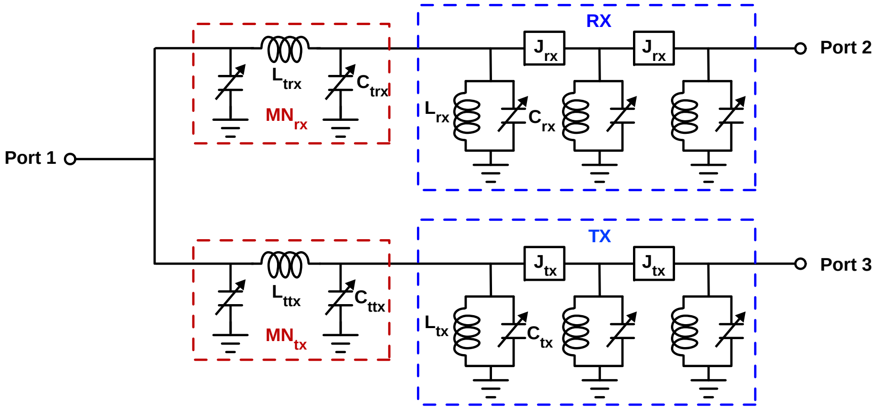

Figure 4.6: Equivalent circuit of a tunable diplexer with tunable matching networks.

Table 4.1: Component Values of Matching Networks of Fig. 4.7

	L_{trx}	C_{trx}	L_{ttx}	C_{ttx}
f_{rx} = 2.3 GHz f_{tx} = 2.1 GHz	2.91 nH	0.88 pF	3.81 nH	1.72 pF
f_{rx} = 2.3 GHz f_{tx} = 1.4 GHz	2.91 nH	2.65 pF	3.81 nH	1.4 pF

Table 4.2: Component Values of Matching Networks of Fig. 4.8

	L_{trx}	C_{trx}	L_{ttx}	C_{ttx}
f_{rx} = 1.98 GHz f_{tx} = 1.8 GHz	3.41 nH	1.08 pF	4.41 nH	2.12 pF
f_{rx} = 2.3 GHz f_{tx} = 1.4 GHz	3.41 nH	2.04 pF	4.41 nH	1.25 pF

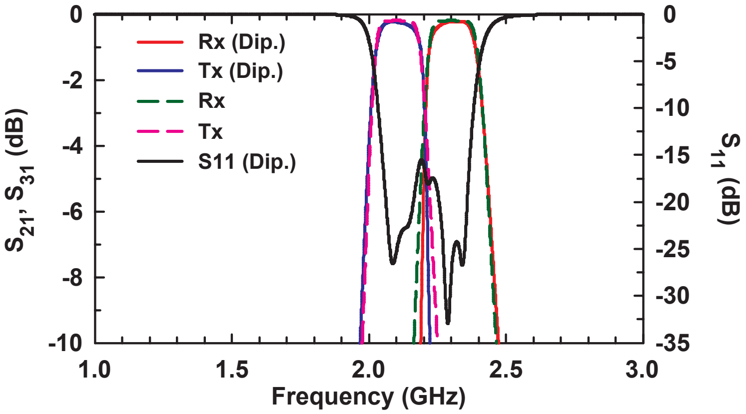

(a)

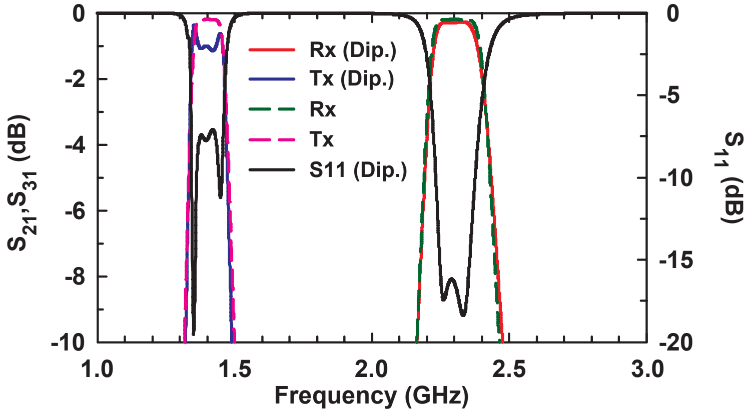

(b)

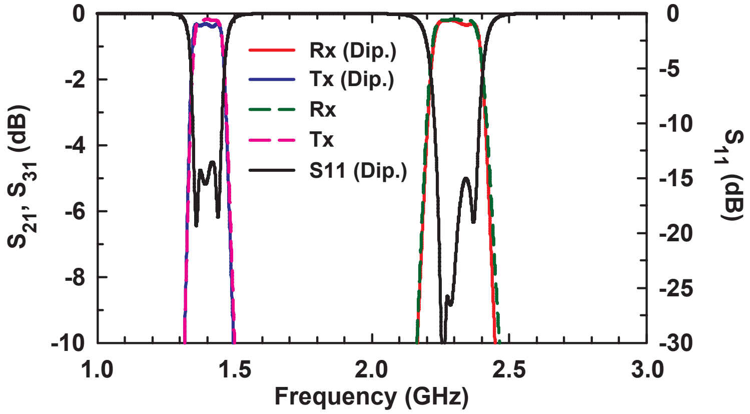

(c)

Figure 4.7: Diplexer performance at (a) f_{rx} = 2.3 GHz and f_{tx} = 2.1 GHz with matching networks at the same frequencies (b) f_{rx} = 2.3 GHz and f_{tx} = 1.4 GHz with matching networks at 2.3 GHz and 2.1 GHz (b) f_{rx} = 2.3 GHz and f_{tx} = 1.4 GHz with matching networks at the same frequencies.

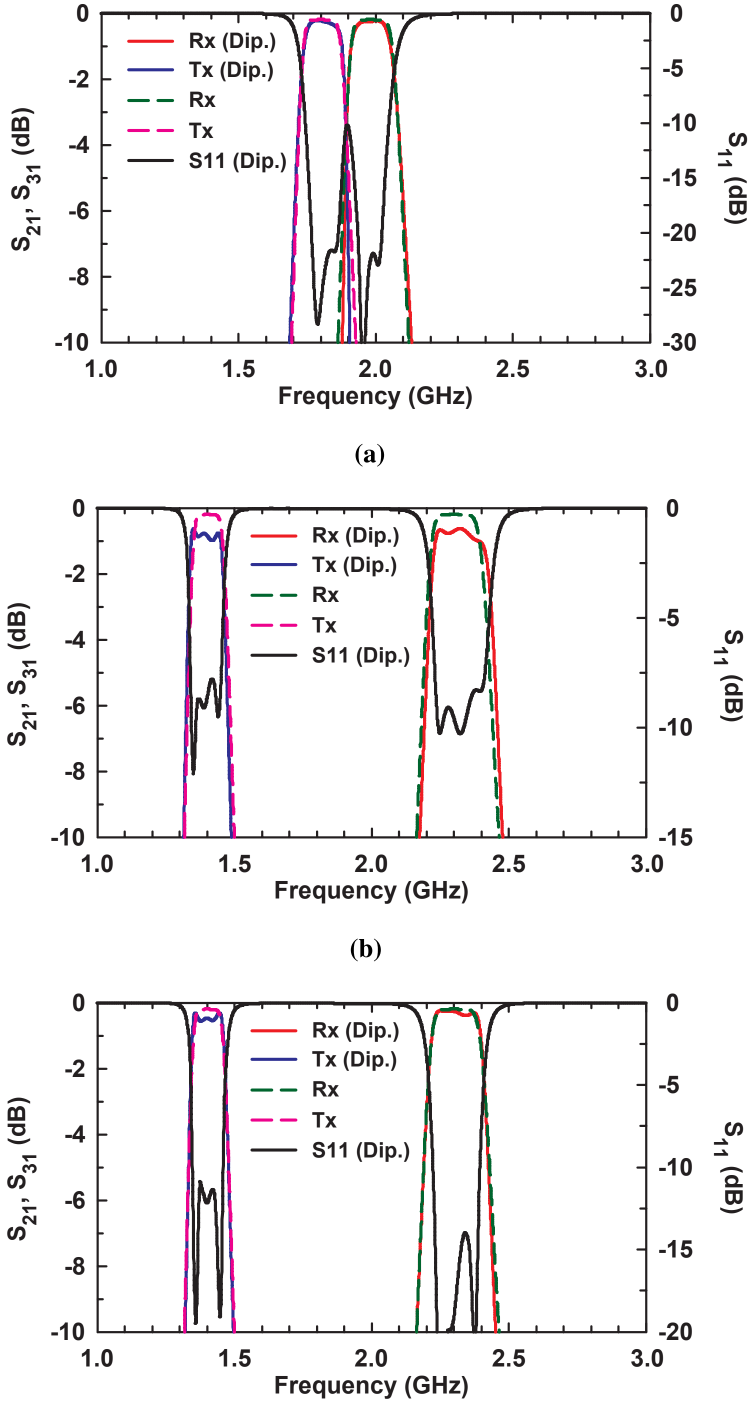

(a)

(b)

(c)

Figure 4.8: Diplexer performance at (a) f_{rx} = 1.98 GHz and f_{tx} = 1.8 GHz with matching networks at the same frequencies (b) f_{rx} = 2.3 GHz and f_{tx} = 1.4 GHz with matching networks at 2.3 GHz and 2.1 GHz (b) f_{rx} = 2.3 GHz and f_{tx} = 1.4 GHz with matching networks at the same frequencies

$S_{11}^{RX} \neq 1$ and therefore, $|S_{11}| > 0$ (not matched) and $S_{31} < S_{21}^{TX}$. Therefore, S_{11} increases to -7.5 dB and the loss increases to 0.8 dB at 1.4 GHz. Fig. 4.7(c) presents the simulations when the matching network is changed to become nearly 90^o at 1.4 GHz using capacitor tuning. The diplexer response is greatly improved with $S_{11} <$ -10 dB at both frequencies. Also, at 1.4 GHz, the loss difference between the diplexer and stand-alone filters is now improved to $<$ 0.14 dB. Since the inductance is not changed in the C-L-C matching network, the phase is not exactly represented by a 90^o line and therefore small degradation can still be seen. However, this degradation is not present when the resonator quality factor are relatively low (Q$\sim$100).

Fig. 4.8 presents the case when the matching networks are chosen at f_{rx} = 1.98 GHz and f_{tx} = 1.8 GHz (see Table 4.2). The diplexer is well-matched at both frequencies and S_{21} is close to two individual filters. The filters are now tuned to f_{rx} = 2.3 GHz and f_{tx} = 1.4 GHz without changing the matching networks, which results in a degraded response (Fig. 4.8(b)). By tuning the capacitors in the matching networks, the diplexer frequency response is improved and is similar to the individual filter response.

It is important to note that more wideband tuning can be achieved using higher-order matching networks, such as C-L-C-L-C networks. However, in practice and due to the limited inductor Q and matching network loss, it is best to use a simple C-L-C π-network.

4.4 Design and Measurement of A Tunable Diplxer

Fig. 4.9 presents the tunable diplexer. The combline filters are conventional Chevyshev filters with fractional bandwidth of 5% and passband ripple of 0.01 dB. The diplexer is fabricated on 25-mil Rogers RT6010 with ε_r = 10.2 and tanδ = 0.0023. The unloaded resonator Q is 157-224 at 1.5-2.5 GHz. Two varactors in the matching networks are combined into C_{com}. Skyworks varactor diodes [71] are used as tuning elements: SMV1405 (0.63-2.67 pF) is used for C_{rx} and C_{tx} and SMV2019 (0.3-2.2 pF) is used for C_{com}, C_{trx} and C_{ttx}. The Q of SMV1405 and SMV2019 is $\sim$40 at 2 GHz for midband capacitance values, which results in a filter loss of $\sim$5 dB and a matching network loss of 0.1 dB. Coilcraft air-core inductors [72] are used in the matching

Table 4.3: Dimesions and Component Values of the Proposed Tunable Diplexer

Filter Dimensions (unit: mm)			
L	S	d	g
6.1	1.93	5.94	0.25

Component Values				
C_{blk}	L_{trx}	L_{ttx}	$C_{com}(C_{trx},C_{ttx})$	$C_{rx}(C_{tx})$
10 pF	2.55 nH	3.85 nH	SMV2019	SMV1405

*L: Coilcraft air-core inductor, C_{blk}: ATC capacitor, C: Skyworks diode

networks, and the ATC high-Q capacitors ($Q > 100$ at 1 GHz) [73] are used as C_{blk} as DC blocks. In addition, due to requirement on small capacitance values in the matching networks, the ground plane underneath the component pads are removed to reduce the layout parasitic capacitance. Detailed dimensions and component values are shown in Table 4.3. The fabricated tunable diplexer is shown in Fig. 4.9(b) with an overall size is $\sim$1.0 x 2.2 cm^2.

The 3-pole tunable combline stand-alone filter tunes from 1.415 GHz to 2.31 GHz with 1-dB fractional bandwidth of $\sim$4.5% and an insertion loss of 7.8-5.1 dB. With reconfigurable matching networks, the tunable diplexer can be tuned in any manner and three tuning scenarios will be shown in Figs. 4.10-4.12.

Fig. 4.10 presents the case when f_{tx} is tuned from 1.425 GHz to 2.07 GHz and f_{rx} is fixed at the highest frequency, 2.27 GHz. With the tunable matching networks, the filter responses at f_{rx} is almost unchaged while f_{tx} moves. The insertion loss at f_{rx} is 5 dB for all states and that at f_{tx} is 7.7-6 dB over the tuning range. In addition, the 1-dB fractional bandwidth at both frequencies is $\sim$4.8%. Comparing to an individual filter, the responses of the diplexer and an individual filter are very similar to each other. As expected, the reconfigurable matching networks restore the diplexer passband responses versus frequency tuning without a loss penalty in loss. Note that even if one filter is tuned, the capacitors for both reconfigurable matching networks are tuned since they share C_{com}.

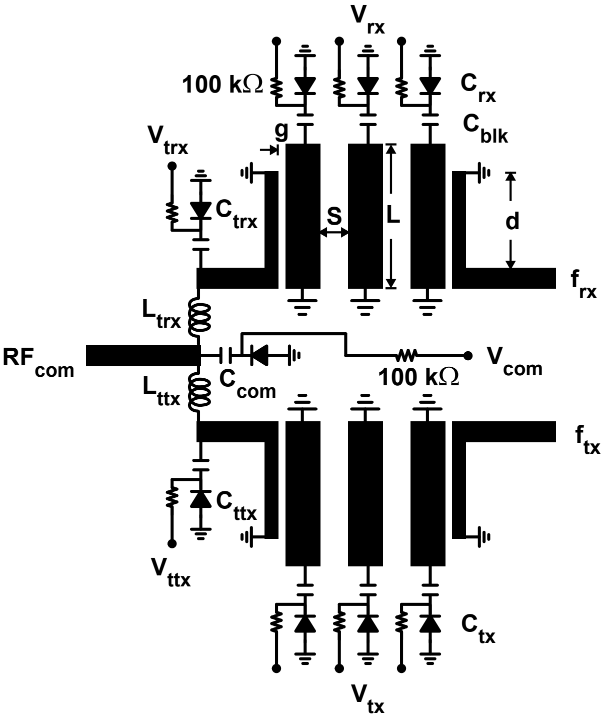

(a)

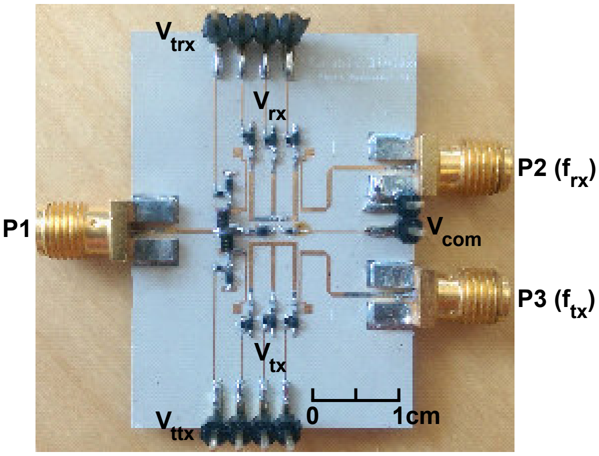

(b)

Figure 4.9: Tunable diplexer composed of two 3-pole tunable bandpass filters and tunable π matching networks : (a) schematics and (b) photo.

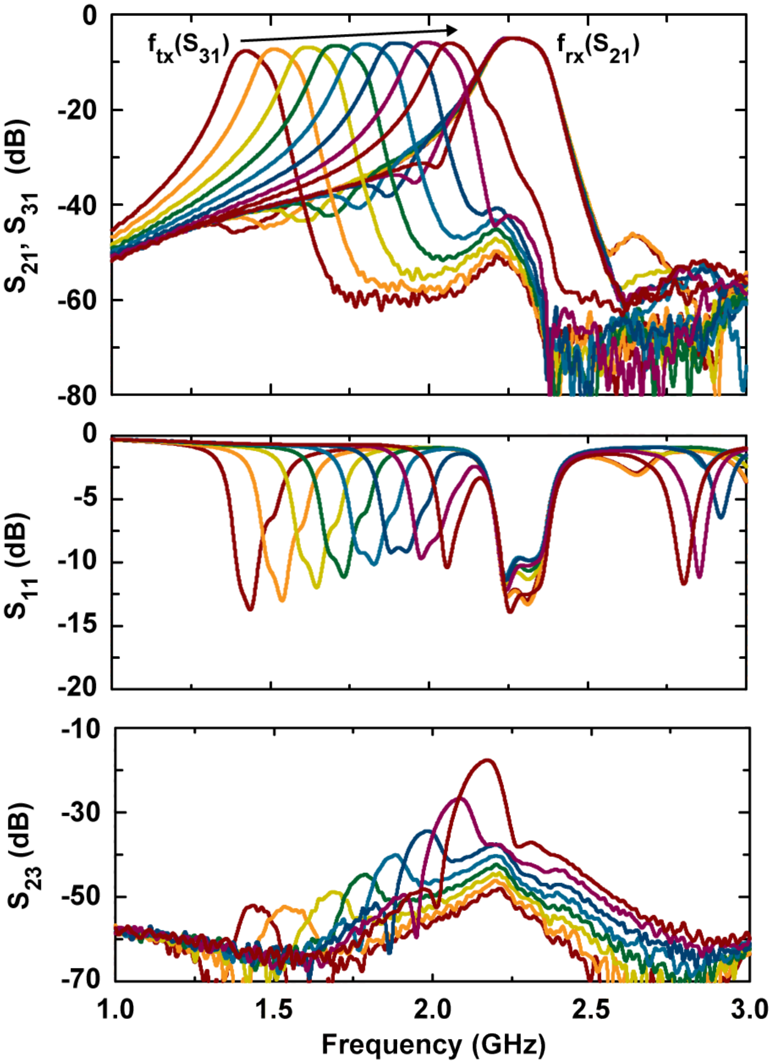

Figure 4.10: Measured S-parameters when f_{rx} is fixed and f_{tx} is tuned.

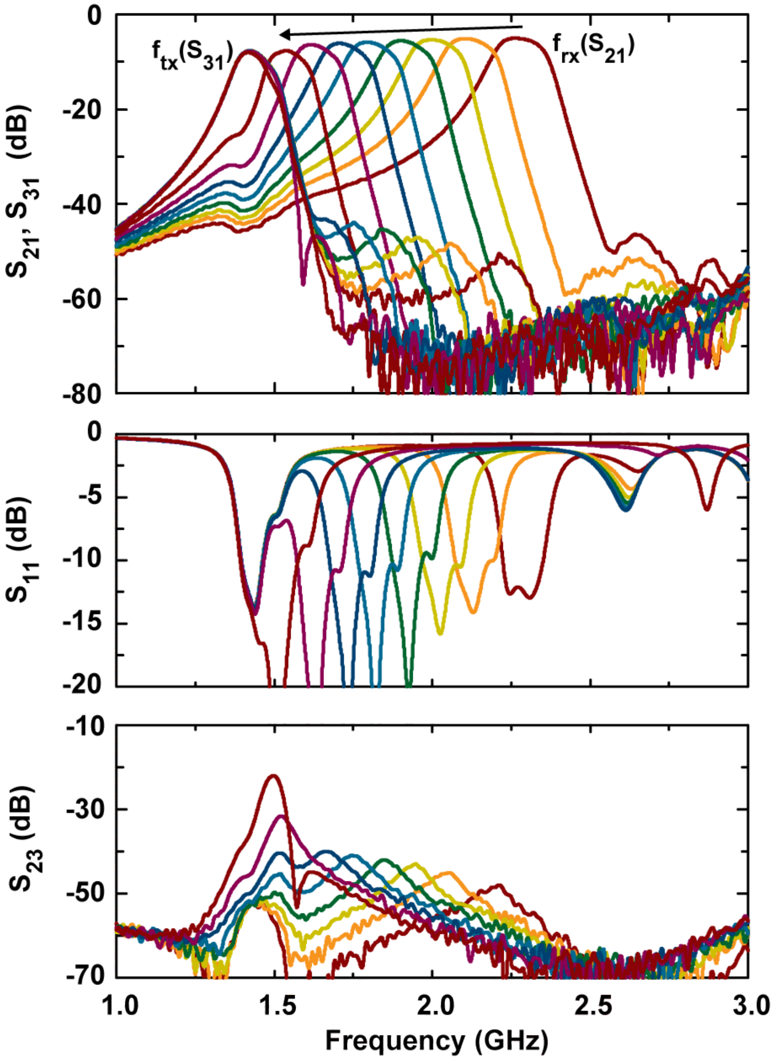

Figure 4.11: Measured S-parameters when f_{tx} is fixed and f_{rx} is tuned.

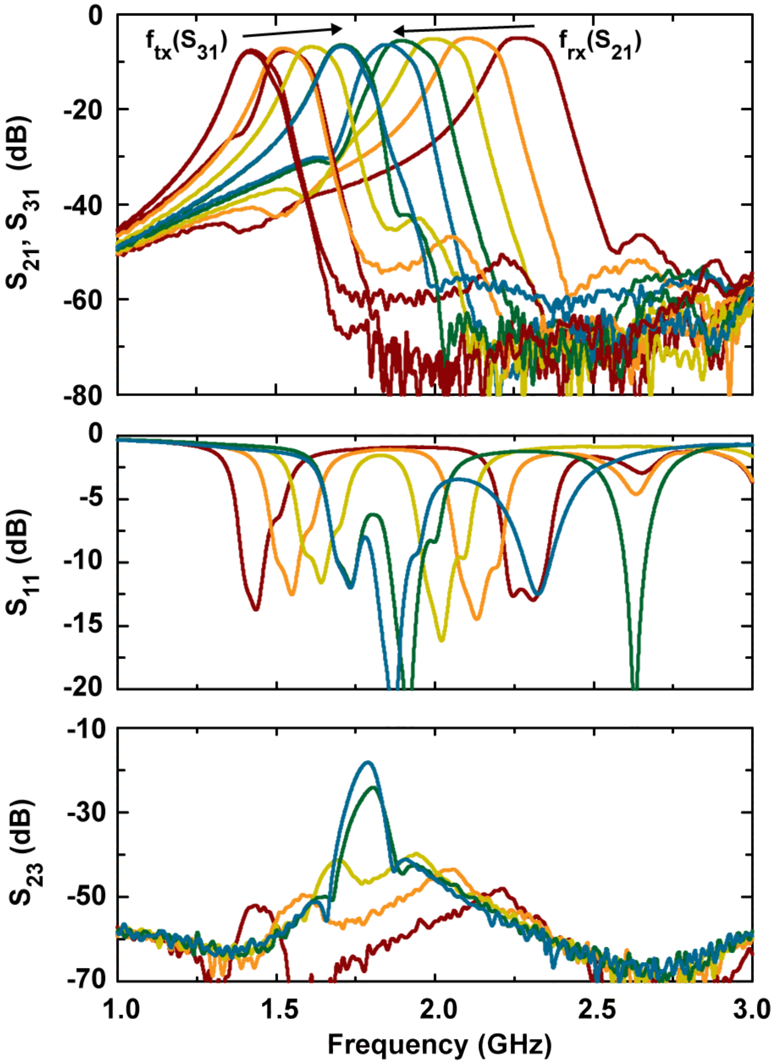

Figure 4.12: Measured S-parameters when both f_{tx} and f_{rx} are tuned toward the middle of tuning range.

Fig. 4.11 presents the case when f_{rx} is tuned from 2.27 GHz to 1.535 GHz and f_{tx} is fixed at 1.425 GHz. The frequency separation is 110 MHz, which is the smallest separation for this tunable diplxer. The insertion loss at f_{tx} is 7.7 dB for all states and that at f_{rx} is 5-7.68 dB, all dominated by the varactor Q. Again, the reconfigurable matching networks ensure that the diplexer response is not distorted versus frequency tuning.

Fig. 4.12 presents the case where both filters are tuned toward the middle of the tuning range. In this case, f_{rx} is tuned from 2.27-1.85 GHz and f_{tx} is tuned from 1.425-1.71 GHz. The closest frequency separation is 140 MHz. The insertion loss is 5-6.43 dB for f_{rx} and 7.7-6.6 dB for f_{tx}. Again, the reconfigurable matching networks ensure that the diplexer response is not distorted.

The closest frequency separation is different for these three cases. The reason is that the designed 3-pole bandpass filters have a fixed fractional bandwidth, and therefore, a wider absolute 3-dB bandwidth at higher frequencies. As a result, the absolute frequency separation changes when operating at different frequencies. Also, due to the low-Q components, the filter roll-off is relatively slow (compared to high-Q components) and this also results in a wider separation. These problems can be solved by using high-Q tuners (for example, RF MEMS varactors [14]) and placing transmission zeroes at both sides of filter passband. The performance of the proposed tunable diplexer is summarized in Table 4.4.

Fig. 4.13 presents a comparison of the measured responses between the tunable diplexer and a stand-alone tunable 3-pole filter. The results with the widest frequency separation, f_{rx} = 2.27 GHz and f_{tx} = 1.425 GHz, is shown in Fig. 4.13(a) and the small difference at 1.425 GHz is due to tolerance of components. In Fig. 4.13(b), the closet frequency separation, f_{rx} = 1.535 GHz and f_{tx} = 1.425 GHz, is shown, and they match with each other up to at least -3-dB point. The deviation at 1.425 GHz is due to the tuning limitation resulting from parasitic effects of the varactor diodes.

Fig. 4.14 presents the measured degraded filter response when fixed matching networks are used. f_{rx} = 2.27 GHz and f_{tx} = 2.07 GHz for the matching networks and the TX filter is tuned to 1.425 GHz. In this case, the insertion loss increases by $\sim$1 dB at 2.27 GHz and the FBW decreases. This is because the matching network at TX side does not provide a proper open circuit termination at 2.27 GHz. There is no difference

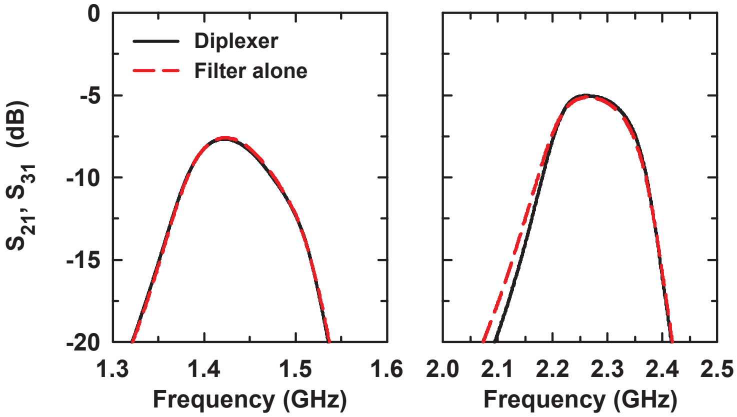

(a)

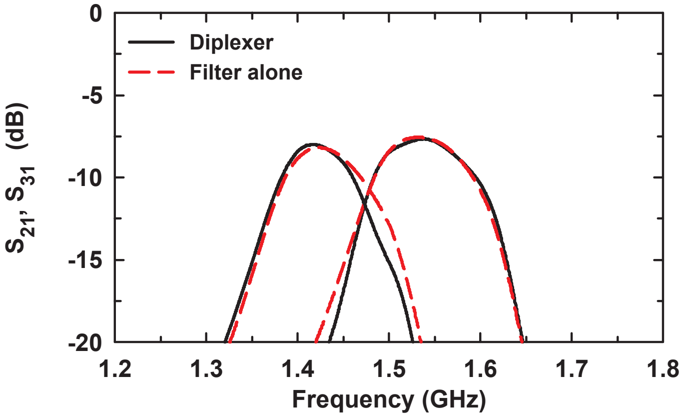

(b)

Figure 4.13: Comparison of measured responses between the tunable diplexer and the tunable filter alone: (a) the furthest separation: f_{rx} = 2.27 GHz and f_{tx} = 1.425 GHz (b) the closest separation: f_{rx} = 1.535 GHz and f_{tx} = 1.425 GHz

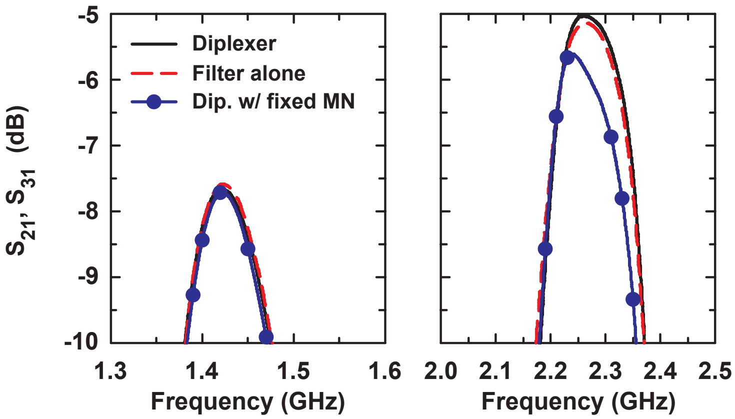

Figure 4.14: Comparison of measured responses with fixed matching networks designed at 2.27 GHz and 2.07 GHz.

Table 4.4: Performance Summary of the Proposed Tunable Diplexer

		Case 1 f_{tx} is tuned	Case 2 f_{rx} is tuned	Case 3 Both are tuned
Rx	Freq.(GHz)	2.27	2.27 - 1.535	2.27 - 1.85
	Loss(dB)	5	5.1 - 7.7	5 - 6.43
	FBW(%)	4.8	4.8	4.8
Tx	Freq.(GHz)	1.425 - 2.07	1.425	1.425 - 1.71
	Loss(dB)	7.7 - 6	7.7	7.7 - 6.6
	FBW(%)	4.8	4.8	4.8

at 1.425 GHz due to low resonator Q and the parasitics from the components. This experiment, while affected by the low resonator Q and high filter loss, still shows that tunable matching networks can restore the filter properties in a tunable diplexer.

4.5 Conclusion

A tunable diplexer with reconfigurable matching networks is investigated and demonstrated. In this design, the filter out of band impedance can be transformed from a short circuit into an open circuit. This leads to a tunable diplexer without any complicated design process. In addition, by using high-Q components, such as RF MEMS varactors and placing transmission zeroes at both side of a filter, the frequency separation and isolation between the two bands can be further improved.

4.6 Acknowledgements

The authors would like to thank Coilcraft Inc. for inductor samples and Rogers Corporation for providing the substrates.

Chapter 4 is based on and mostly a reprint of the following paper: CH. Ko and G. M. Rebeiz, "A 1.4-2.3 GHz Tunable Diplexer Based on Reconfigurable Matching

Networks," submitted for publication in *IEEE Trans. Microw. Theory Tech.*, Aug. 2014.

Chapter 5

Tunable 500-1200 MHz Dual-band and Wide Bandwidth Notch Filters with RF Transformers

5.1 Introduction

Microwave tunable bandstop filters have become essential in the modern communication systems due to the availability of large interferers such as TV broadcast stations. In order to reduce the system complexity, a tunable bandstop filter can be used to reduce the interferer level before the LNA, thereby relaxing the system linearity and power consumption. Recently, several tunable bandstop filters using varactor diodes [74–78] and RF MEMS varactors [79–84] have been demonstrates. However, these design can only generate a single rejection band, which is not enough for advanced communication systems.

Dual- or multi-band bandstop filters are starting to attract attention because they can reject multiple unwanted signals, which is essential for crowded environments. Fixed-frequency dual-band bandstop filters can be designed by metamaterial [85], dual-mode resonators [86], stepped-impedance resonators (SIR) [87, 88] and multiple single-resonant-frequency resonators [89, 90]. However, some of above design methods are very difficult to use in tunable filters. The multiple resonator technique can be used in tunable dual-band bandstop filters [91] but it requires a large circuit area.

This paper presents a novel method to implement tunable dual-band bandstop filters. By using the coupled properties of an RF transformer, two coupled resonant frequencies are generated within one resonator and by sharing the same inverters, a tunable dual-band bandstop filter is realized. This results in a small size (about half of the size of two independent notch filters) and lower loss. In this method, the filter component values are calculated using the standard Chebyshev or Butterworth parameters, resulting in a straightforward design.

The progression of the paper is as follows: First, a dual-band resonator implemented using an RF transformer is analyzed and the design procedure is introduced. Then, based on the different coupling values obtained using PCB and air-coil RF transformers, two different 2-pole tunable bandstop filters are demonstrated: a) a tunable dual-band bandstop filter and b) a tunable bandstop filter with wide rejection bandwidth. The paper concludes with a demonstration of a dual-band bandstop filter with tunable frequency separation.

5.2 Analysis of a Resonator implemented by a Transformer

5.2.1 Transformers with Fixed Coupling

Fig. 5.1 presents a RF transformer where $\mathrm{L_p}$ and $\mathrm{L_s}$ are the primary and the secondary inductance, and M is the mutual inductance determined by

$$M = K_{xfmr}\sqrt{L_p L_s} \tag{5.1}$$

where $\mathrm{K_{xfmr}}$ is the transformer coupling coefficient. Adding capacitors ($\mathrm{C_1}$ and $\mathrm{C_2}$) at the transformer sides forms two LC resonators, but due to the coupling between the two inductors, the two uncoupled frequencies split apart and form two new coupled frequencies. The relationship between the two coupled frequencies can be derived as follows.

The Z matrix for a transformer is

$$\begin{bmatrix} V_1 \\ V_2 \end{bmatrix} = \begin{bmatrix} j\omega L_p & j\omega M \\ j\omega M & j\omega L_s \end{bmatrix} \begin{bmatrix} I_1 \\ I_2 \end{bmatrix} \tag{5.2}$$

The relationship between V_2 and I_2 is

$$V_2 = -\frac{1}{j\omega C_2} I_2 \tag{5.3}$$

Through (5.1)-(5.3), Z_1 can be derived as

$$Z_1 = j\frac{\omega L_p + \omega^3 (K_{xfmr}^2 - 1) L_p L_s C_2}{1 - \omega^2 L_s C_2} \tag{5.4}$$

Then, the input admittance of the dual-band resonator, Y_{in}, is

$$Y_{in} = j\frac{\omega^4 (K_{xfmr}^2 - 1) L_p L_s C_1 C_2 + \omega^2 (L_p C_1 + L_s C_2) - 1}{\omega^3 (K_{xfmr}^2 - 1) L_p L_s C_2 + \omega L_p} \tag{5.5}$$

At the resonance, $Y_{in} = 0$, and

$$\omega^4 (K_{xfmr}^2 - 1) L_p L_s C_1 C_2 + \omega^2 (L_p C_1 + L_s C_2) - 1 = 0 \tag{5.6}$$

The two coupled resonant frequencies, ω_1 and ω_2, can now be solved. Assuming $\omega_2 > \omega_1$, the effective coupling between the two resonators, $K_{resonator}$, is

$$K_{resonator} = \frac{{\omega_2}^2 - {\omega_1}^2}{{\omega_2}^2 + {\omega_1}^2} = \frac{2K_{xfmr}\sqrt{L_p L_s C_1 C_2}}{L_p C_1 + L_s C_2} \tag{5.7}$$

From (5.7), the coupled resonant frequencies depend not only on the values of L_p, L_s, C_1 and C_2 but also the coupling coefficient, K_{xfmr}. If $K_{xfmr} = 0$ (no coupling between the primary and secondary inductors), then $K_{resonator} = 0$, and the two resonators are independent to each other, as expected. However, if the two uncoupled resonant frequencies are chosen to be the same, $L_pC_1 = L_sC_2$, then $K_{resonator} = K_{xfmr}$. In this case, the separation between the two coupled frequencies can be uniquely determined by the transformer coupling coefficient.

Another important property about a resonator is its 3-dB bandwidth, which is calculated from the susceptance slope. Assuming $L_pC_1 = L_sC_2 = A$,

$$\begin{aligned} \frac{\vartheta B}{\vartheta \omega} &= \frac{\vartheta Y_{in}}{\vartheta \omega} \\ &= \frac{m^2 A^3 \omega^6 + m A^2 \omega^4 + (3m+2) A \omega^2 + 1}{m^2 A^2 \omega^6 + 2mA\omega^4 + \omega^2} \\ &, where\ m = {K_{xfmr}}^2 - 1 \end{aligned} \tag{5.8}$$

Table 5.1: Component Values for Fig. 5.2

	K_{xfmr}	L_p	L_s	C_1	C_2
Case 1	0.332	3.71	7.58	11.4	5.59
Case 2	0.15	5.55	5.55	7.5	7.5

L: nH, C: pF

From (5.7),

$$\omega^2 = \frac{1}{(K_{xfmr}+1)A} \, or \, \frac{1}{(1-K_{xfmr})A} = {\omega_1}^2 \, or \, {\omega_2}^2 \tag{5.9}$$

and

$$\Delta\omega_{3dB} = \frac{\omega_0}{2}\frac{Y_0}{b} = \frac{\omega_0}{2}\frac{Y_0}{\frac{\omega_0}{2}\frac{\vartheta B}{\vartheta\omega}} = Y_0\left(\frac{\vartheta B}{\vartheta\omega}\right)^{-1} \tag{5.10}$$

The 3-dB bandwidth of the proposed dual-band resonator can then be derived as:

$$\Delta\omega_{3dB,\omega_1} = \Delta\omega_{3dB,\omega_2} = \frac{Y_0}{4A} \tag{5.11}$$

This indicates that as long as the uncoupled resonant frequencies are chosen to be the same, the 3-dB bandwidths for both coupled resonant frequencies will be the same and depend on the chosen uncoupled resonant frequency values.

Fig. 5.2 presents an ideal dual-band resonator with values shown in Table 5.1. In this simulation, $L_pC_1 = L_sC_2$ in order to verify the derivation above. For Case 1, the two coupled resonant frequencies are 670 MHz and 946 MHz, respectively, resulting in $K_{resonator} = 0.33$, which equals K_{xfmr}. The 3-dB bandwidths are both 17.4 MHz. For Case 2, the two coupled frequencies are 728 MHz and 848 MHz ($K_{resonator} = 0.151$) with 3-dB bandwidth of ~26.3 MHz. As can be seen, there is excellent agreement between Agilent ADS [45] simulations and the theoretical model.

5.2.2 Transformers with Tunable Coupling

It is clear from the derivation above that if the transformer coupling can be tuned, then the notch frequencies can also be tuned. This can be done by the addition of electric coupling between the primary and secondary inductors. The best way to implement

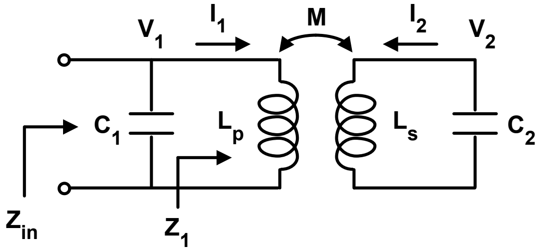

Figure 5.1: The proposed dual-band resonator with a transformer.

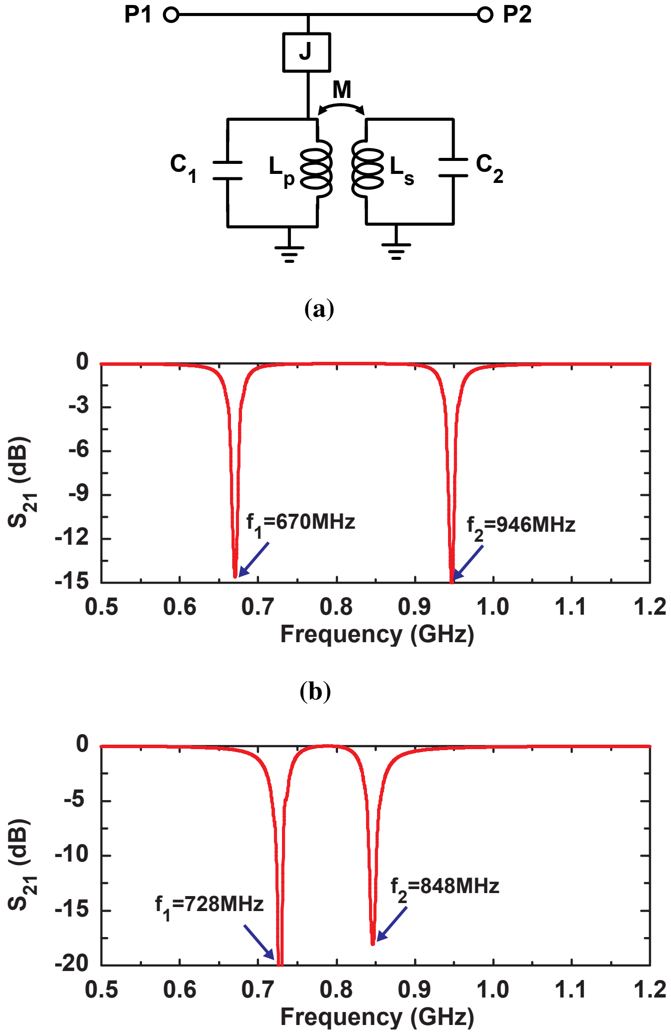

(a)

(b)

(c)

Figure 5.2: (a) Schematic of an ideal dual-band resonator and its frequency responses when (b) $K_{xfmr} = 0.332$ and (c) $K_{xfmr} = 0.15$.

wideband electric coupling is using J-inverters. However, this requires a -C shunt to ground, which is not feasible. Another way is using a series capacitor (Fig. 5.3(a)) and this is analyzed by the even-odd method [52].

The coupling between two inductors can be represented by equivalent T-model between two planes, T_1 and T_2. For the odd mode, the symmetry plane T is replaced by an electric wall (short-circuit), as shown in Fig. 5.3(b), and the resultant frequency is

$$f_o = \frac{1}{2\pi\sqrt{(L - \frac{L_m}{1+2\omega^2 C_m L_m})C_1}} \tag{5.12}$$

It is seen that the series capacitor reduces the coupling between the two inductors and increases the odd-mode resonant frequency.

For the even mode, a magnetic wall (open-circuit) replaces the symmetry plane, as shown in Fig. 5.3(c), the resultant frequency is

$$f_e = \frac{1}{2\pi\sqrt{(L+L_m)C_1}} \tag{5.13}$$

In this case, the series capacitor has no effect on the even-mode resonant frequency. (5.12)-(5.13) indicate that using a tunable capacitor for C_m will result in one fixed notch frequency (even mode) and one tunable notch frequency (odd mode), thereby having a tunable separation between the two notches.

The simulated dual-band resonator with tunable frequency separation is shown in Fig. 5.4. The component values are the same as the case 1 in Fig. 5.2(b) except with the addition of C_m. When C_m varies from 0 pF to 1 pF, only the higher resonant frequency shifts from 960 MHz to 844 MHz while the lower one is fixed at 670 MHz. Effectively, $K_{resonator}$ (or K_{xfmr}) varies from 0.332 to 0.23 using C_m.

5.3 Transformer Measurements

.

5.3.1 Air-Coil Lumped Transformer

If two air-coil inductors are placed adjacent to each other on a printed circuit board, then HFSS [47] simulations show a K_{xfmr} = 0.05-0.08 (Fig. 5.5). These sim-

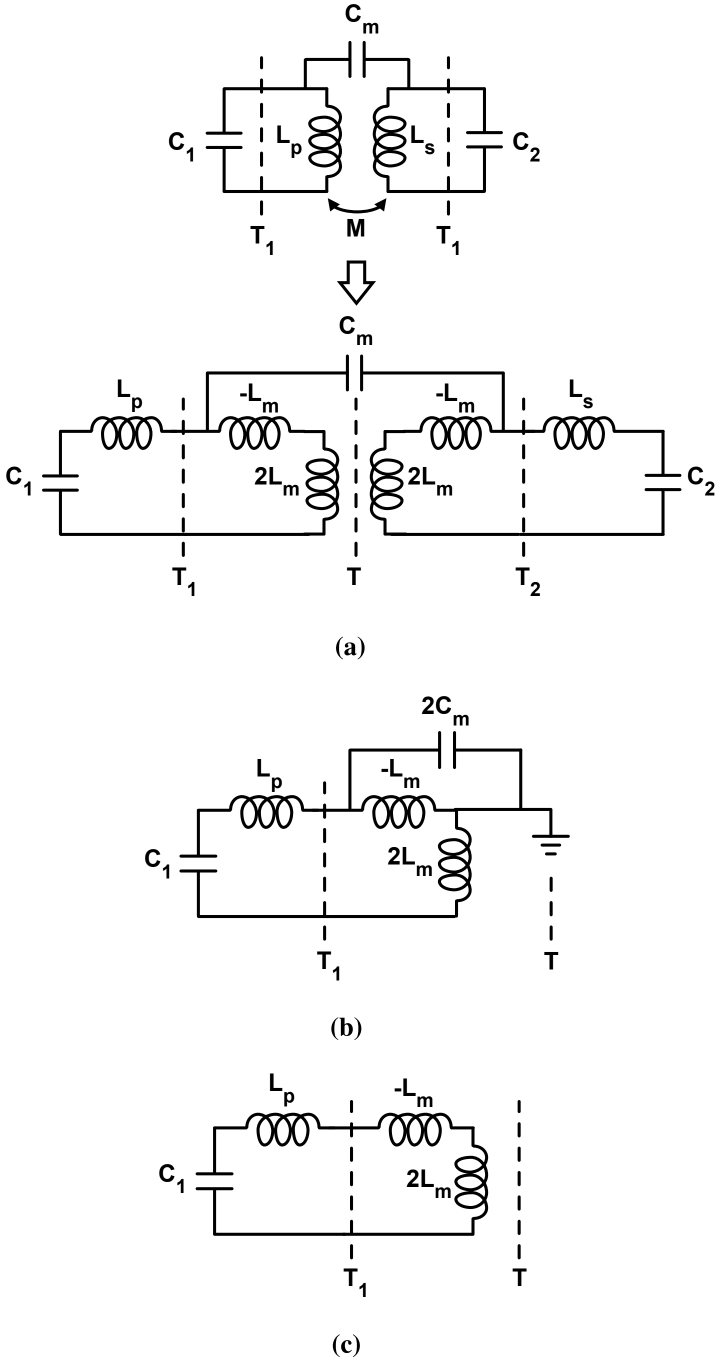

(a)

(b)

(c)

Figure 5.3: (a) Equivalent T-model for a dual-band resonator with a transformer and a series capacitor, and its (b) odd-mode and (c) even-mode analysis.

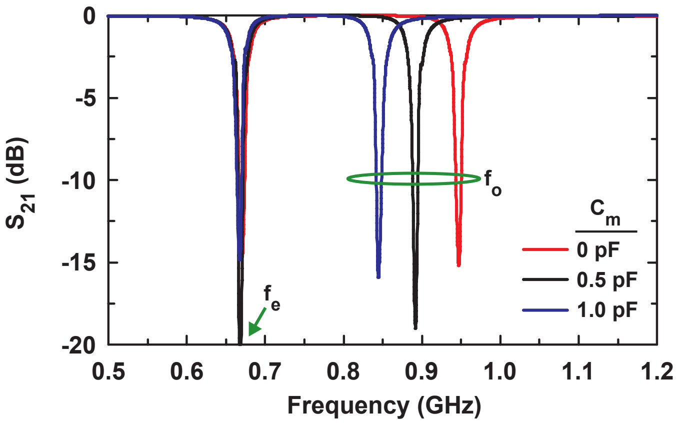

Figure 5.4: Dual-band notch filter simulations v.s. C_m (same filter as Fig. 5.2(a) but with C_m).

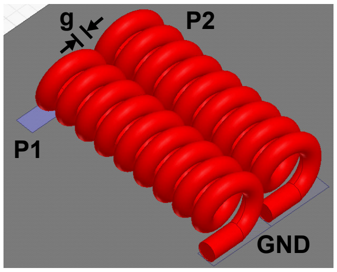

(a)

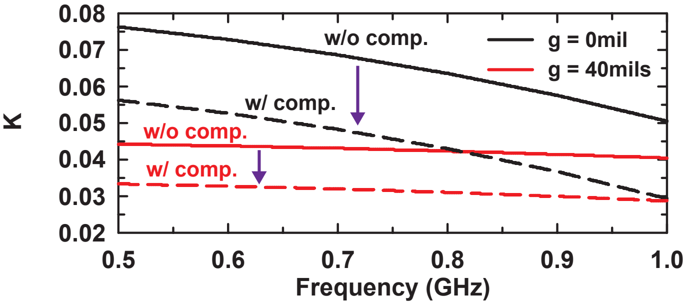

(b)

Figure 5.5: (a) HFSS model of an air-coil transformer. (b) Simulations at different gaps without and with components around the inductors.

ulations are done with dimensions as: n = 9, D_{turn} = 39 mils, length = 165 mils and D_{wire} = 15 mils. The simulated inductance is about 11 nH with Q of 120 at 800 MHz and K_{xfmr} = 0.064 when g = 0 mils (very close to each other but no contact) and 0.043 when g = 40 mils. However, when there are some components around the transformer, K_{xfmr} drops to 0.03-0.04, as shown in Fig.5.5(b). Fig. 5.6 presents the effect of the surrounding components. The magnetic filed concentrates less when metal blocks are present around the inductors, and therefore, K_{xfmr} decreases.

Measurements on air-coil transformers are shown in Fig. 5.7. Coilcraft [72] Microsrping inductors were used and TRL calibration was applied to de-embed the extra transmission line and connectors. At 800 MHz, for 7.15 nH (1606-7GL), the measured inductance is $\sim$10 nH with Q>200 with K_{xfmr} is 0.058. For 9.85 nH (1606-9GL), the measured inductance is $\sim$13.4 nH with Q of 190, and K_{xfmr} is 0.025. The extra inductance is due to the soldering pads and ground vias. The transformer with low K_{xfmr} can be used to design a notch filter with a wide rejection bandwidth resulting from the small pole-splitting effect (see Section 5.4.2).

5.3.2 Printed-Circuit Board (PCB) Transformer

Another way to make a transformer at 600-1000 MHz is using a two-layer planar transformer (Fig. 5.8). The PCB stack-up is shown in Fig. 5.8(b) and is composed of a 16.7-mil RO4003 layer (ε_r = 3.55, tanδ = 0.0029), with a 4-mil RO4450B prepreg layer (ε_r = 3.54, tanδ = 0.004) and another 32.7-mil RO4003 layer. The Rogers 4000 series LoPro substrate has lower copper surface roughness (0.5 μm for 0.5-Oz copper and 0.6 μm for 1-Oz copper) than standard substrates and results in a larger inductor Q.

The separation between the two inductors is chosen to be $\sim$16 mils to achieve a K_{xfmr} = 0.35 for filter applications. The primary inductor is defined on M2 and the secondary inductor is on M1. Both inductors share the same center via connection to the bottom metal, which is the common ground for the filter circuit. In order to reduce the ground current (which reduces the effective inductance), a 32.7-mil substrate between M2 and the ground plane is chosen.

Measurements on several PCB transformers with different inductances are presented in Fig. 5.9. TRL calibration was used to eliminate the connectors and transmis-

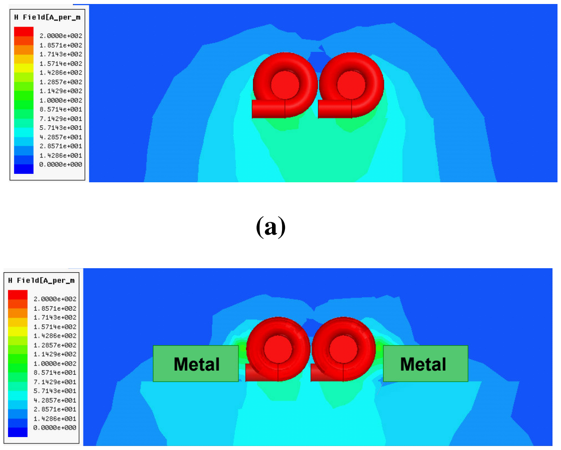

(a)

(b)

Figure 5.6: Simulated H-field (a) without and (b) with components around the air-coil inductors.

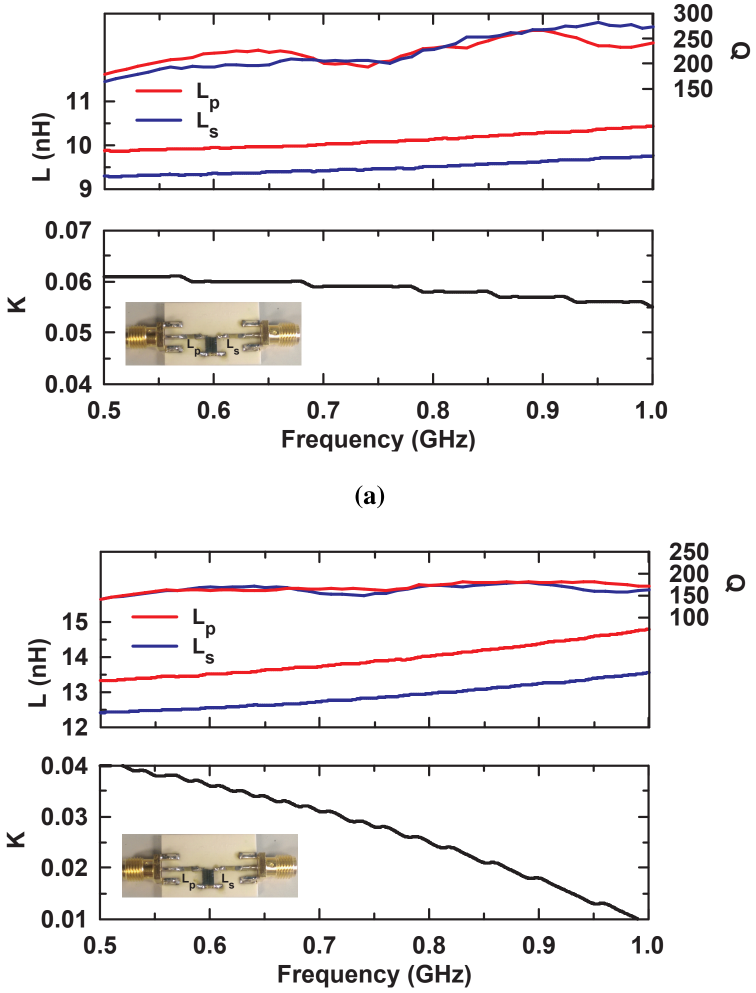

(a)

(b)

Figure 5.7: Measured results of Coilcraft air-coil transformers : (a) L = 7.15 nH and (b) L = 9.85 nH.

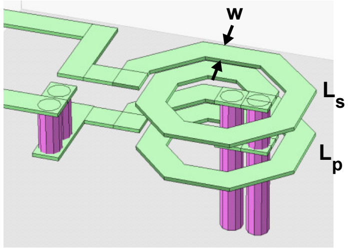

(a)

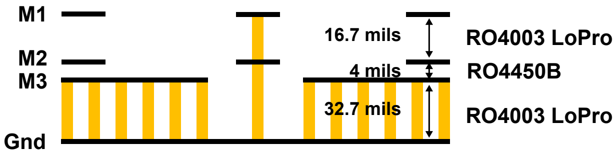

(b)

Figure 5.8: (a) Sonnet [1] model for a two-layer PCB transformer and (b) its stack-up.

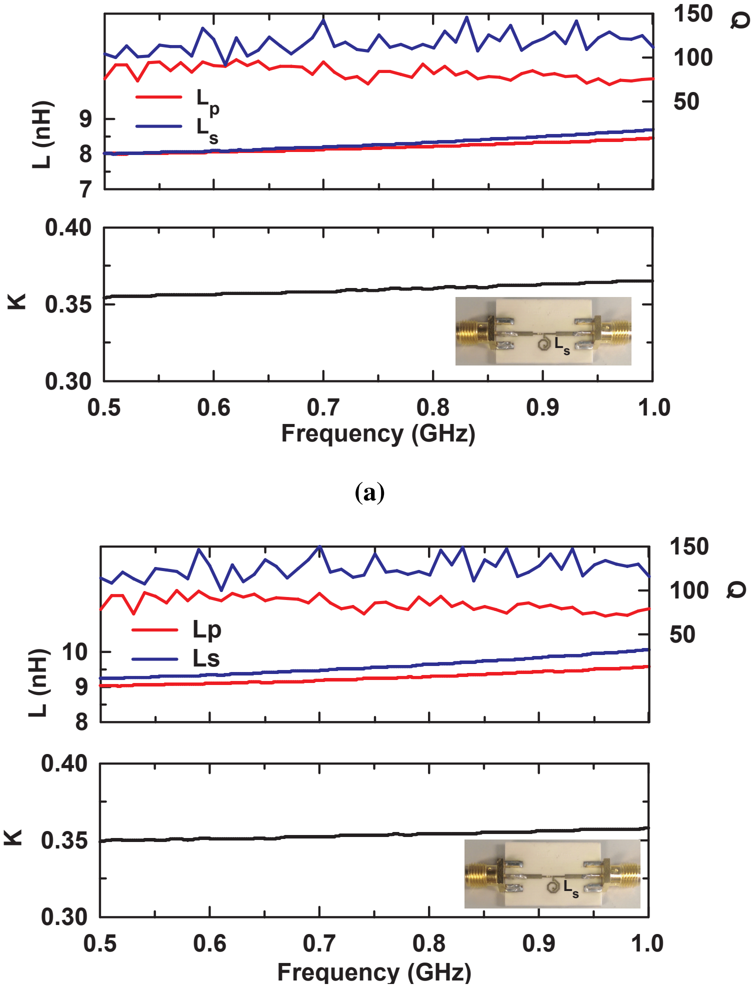

(a)

(b)

Figure 5.9: Measured results of two-layer PCB transformers : (a) W = 20 mils and (b) W = 15 mils.

sion lines in front of the inductors. At 800 MHz, with a trace width of 20 mils, gap of 5 mils and 1.5 turns, the measured primary inductance, L_p (at M2), is 8.2 nH with Q of 82 and the secondary inductance, L_s (at M1), is 8.3 nH with Q of 111. For a trace width of 15 mils, gap of 10 mils and 1.5 turns, L_p is 9.3 nH with Q of 83 and L_s is 9.6 nH with Q of 118. Due to the ground current effect, the inductance and Q for L_p (at M2) are lower than those of L_s (at M1). Both designs result in K_{xfmr} ∼0.35, which is large enough to be implemented in the dual-band notch filter.

5.4 Tunable Dual-band Notch Filters

5.4.1 Design Procedure

The design procedure for *n*th-order dual-band notch filters with transformers (shown in Fig. 5.10) is based on work done in [75] and is:

a) Start with standard lowpass parameters, g.

b) Choose appropriate inductance, L, for resonators.

c) Choose the center frequency, f_0, and then $C_r = \frac{1}{L(2\pi f_0)^2}$

d) Choose the 3-dB fraction bandwidth, Δ, and Z_0, and then

$$\begin{cases} C_{si} = \sqrt{\frac{\Delta g_i}{L Z_0 {\omega_0}^3}}, \; i = odd \\ C_{si} = \sqrt{\frac{\Delta g_i g_{n+1}}{L Z_0 {\omega_0}^3}}, \; i = even \end{cases}$$

e) Then

$$C_{ai} = C_r - C_{si}$$

$$C_{bi} = C_r$$

f) The component values for the inverters can be calculated as:

$$L_{inv} = \frac{Z_0}{\omega_0 \sqrt{g_0 g_{n+1}}}$$

$$\begin{cases} C_{invi} = \frac{\sqrt{g_0 g_{n+1}}}{Z_0 \omega_0} - C_{si}, \; i = 1, n \\ C_{invi} = 2\frac{\sqrt{g_0 g_{n+1}}}{Z_0 \omega_0} - C_{si}, \; i \neq 1, n \end{cases}$$

In this paper, three types of tunable two-pole dual-band notch filters are demonstrated:

Table 5.2: Component values for inter-stage inverters

	w/ PCB xfmrs	w/ air-coil xfmrs
L_{inv}	2.55 nH	7.15 nH
C_{inv}	0.3 pF	2.4 pF

a) a dual-notch filter with PCB transformers, b) a notch filter with air-coil transformers having wide rejection bandwidth and c) a notch filter with PCB transformers and frequency separation tuning.

5.4.2 Notch Filters with PCB and Air-Coil Transformers

The 2-pole notch filter with PCB and air-coil transformers is shown in Fig. 5.11(a). Skyworks schottky varactor diodes [71] are used in the transformer resonator and the J-inverters are implemented using back-to-back varactor diodes [75]. ATC capacitors are used for all fixed high-Q capacitors [73], and L_{inv} is implemented using a high-Q Coilcraft inductors. A 100-pF capacitor is used in series with a varactor diode for DC block. Also, 100-kΩ resistors are used for biasing. The component values for the inverter between resonators are optimized for required tuning range, as shown in Table 5.2.

For the PCB transformer implementation (Fig. 5.11(b)), w = 20 mils is used for the two-layer transformer, and Skyworks SMV1234-079LF varactors with a capacitance of 1.32-9.63 pF are used for D_1-D_3. The varactor Q is $\sim$75 for 5 pF at 900 MHz. The lower frequency, f_1, tunes from 845-513 MHz and the higher frequency, f_2, tunes from 1171-715 MHz (Fig. 5.12). The measured $K_{resonator}$ is 0.3-0.35 in the tuning range, which is a little less than K_{xfmr} due to the surrounding components. The notch level is $>$ 16 dB over the tuning range. A rapid S_{21} roll-off occurs above 1100 MHz for the lowest frequency setting due to the self-resonance of the 100-pF dc-block capacitor. This can be solved using RF MEMS varactors, which have no requirement for dc-block capacitors (or smaller dc-block capacitors). As shown in Fig. 5.13, measurements agree well with simulations before the self-resonance of the dc-block capacitor occurs.

A Coilcraft Microspring inductor of 7.15 nH (1606-7GL) is chosen for the air-coil transformer implementation (Fig. 5.11(c)). The same Skyworks SMV1234-079LF

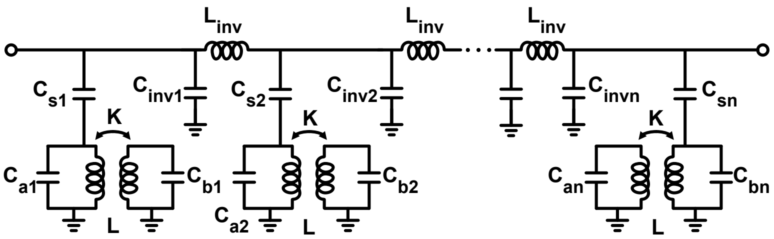

Figure 5.10: Schematic of the dual-band notch filter

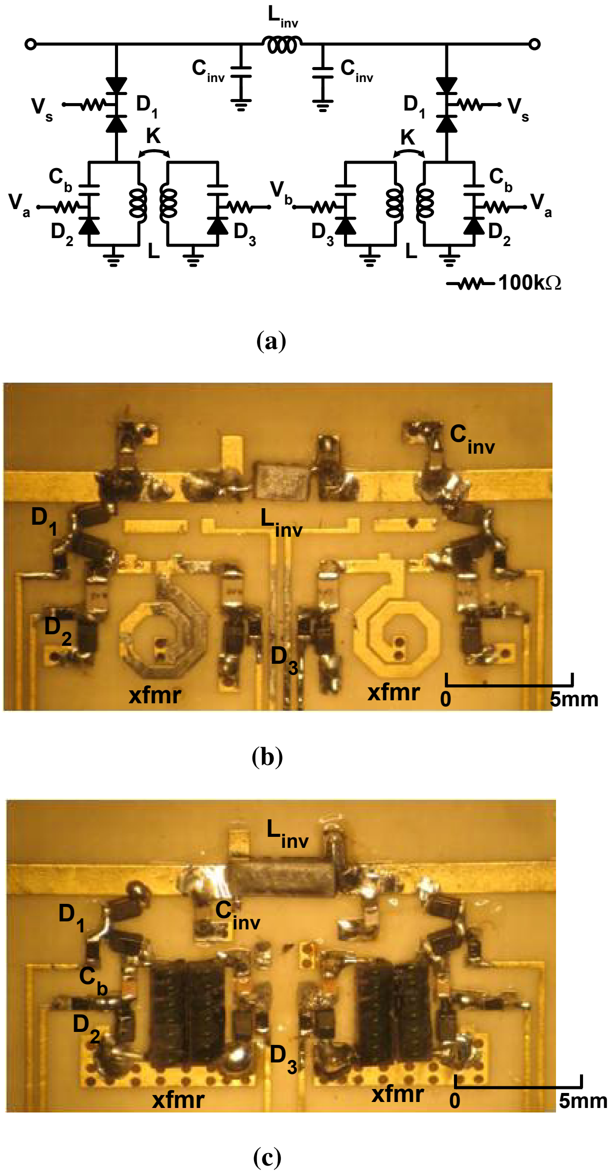

Figure 5.11: (a) Tunable two-pole dual-band notch filter and photos of the proposed dual-band notch filters: (b) with PCB transformers and (c) with Coilcraft air-coil transformers.

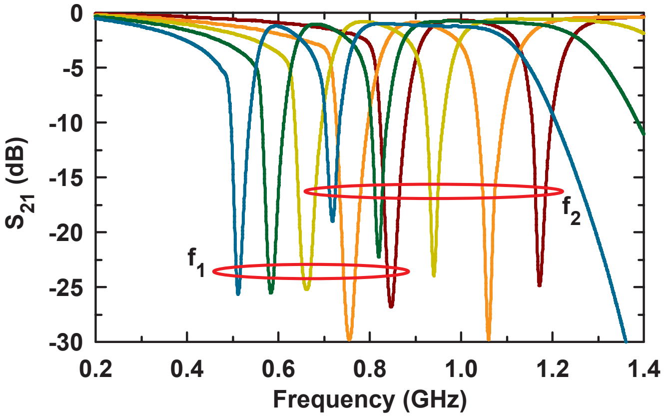

(a)

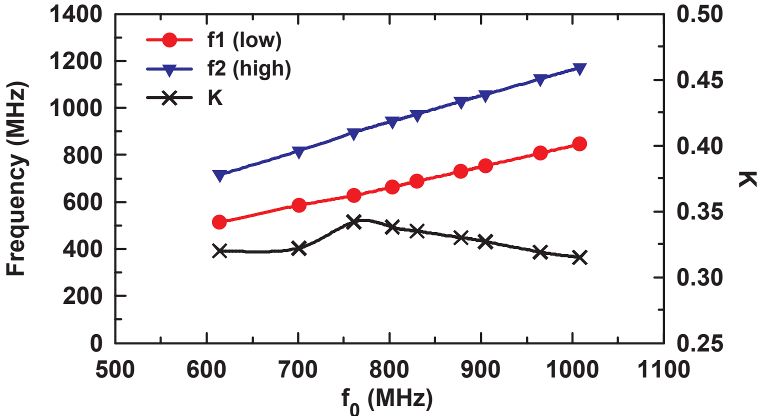

(b)

Figure 5.12: (a) Measured S_{21} and (b) f_1, f_2 and K v.s. f_0 of the tunable two-pole dual-band notch filter with PCB transformers.

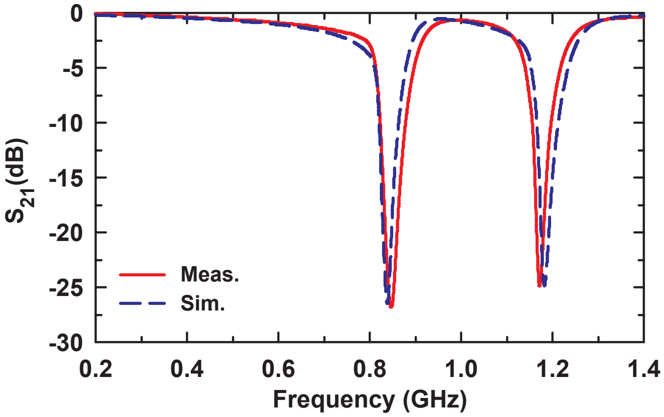

(a)

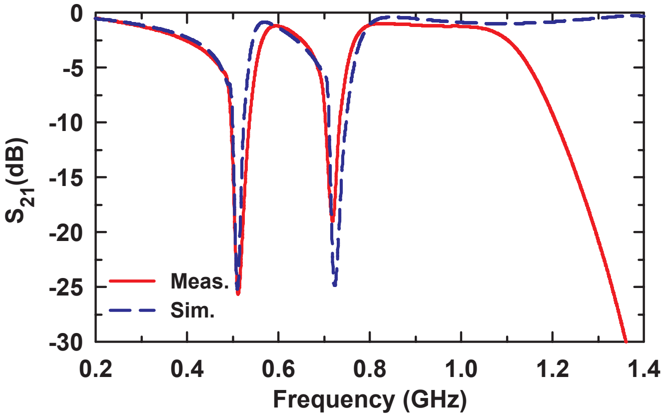

(b)

Figure 5.13: Comparison between measurement and simulation at (a) higher frequency range and (b) lower frequency range. See text for details.

varactors are used for D_1-D_3. In this case, and due to the very low K_{xfmr}, the two notches are very close to each other resulting a wideband bandstop filter. As shown in Fig. 5.14, the notch frequency is tuned from 982-604 MHz with a 20-dB rejection bandwidth of 27-45 MHz and a 15-dB rejection bandwidth of 40-58 MHz. Two coupled resonant frequencies can still be seen, and the effective $K_{resonator}$ is 0.015-0.04 in the tuning range. Comparing with Fig. 5.7(a), $K_{resonator}$ is less than K_{xfmr} due to the surrounding lumped components.

5.4.3 Notch Filters with Frequency Separation Tuning

The two-pole dual-band notch filter with frequency separation tuning is shown in Fig. 5.15. The design is built using PCB transformers with K_{xfmr} = 0.35. Skyworks SMV1405-079LF varactors (C = 0.63-2.67 pF from 30-0 V) are used for C_m (D_4), and a back-to-back configuration is applied for ease of biasing. Measurements are shown in Fig. 5.16. When f_1 is at 830 MHz, f_2 can be tuned from 1121-1031 MHz. In this case, only the bias for D_4 is changed. Effectively, $K_{resonator}$ = 0.29-0.22 as C_m is varied. Also, when f_1 = 600 MHz, f_2 can be tuned from 701-674 MHz and $K_{resonator}$ = 0.28-0.22. As expected, C_m only affects the upper (odd-mode) frequency and the lower (even-mode) frequency remains fixed. The notch rejection level is not as deep when C_m increases due to the fixed inverter used between resonators. This can be remedied with the use of a variable inverter.

5.5 Conclusion

This paper presents a tunable dual-band bandstop filter with RF transformers. Based on different coupling of a transformer, tunable dual-band notch filters or tunable single-band notch filters with wide rejection bandwidth can be achieved. The design procedure is also provided. In the future, using RF MEMS devices, the better frequency responses and higher linearity and power handling can be achieved.

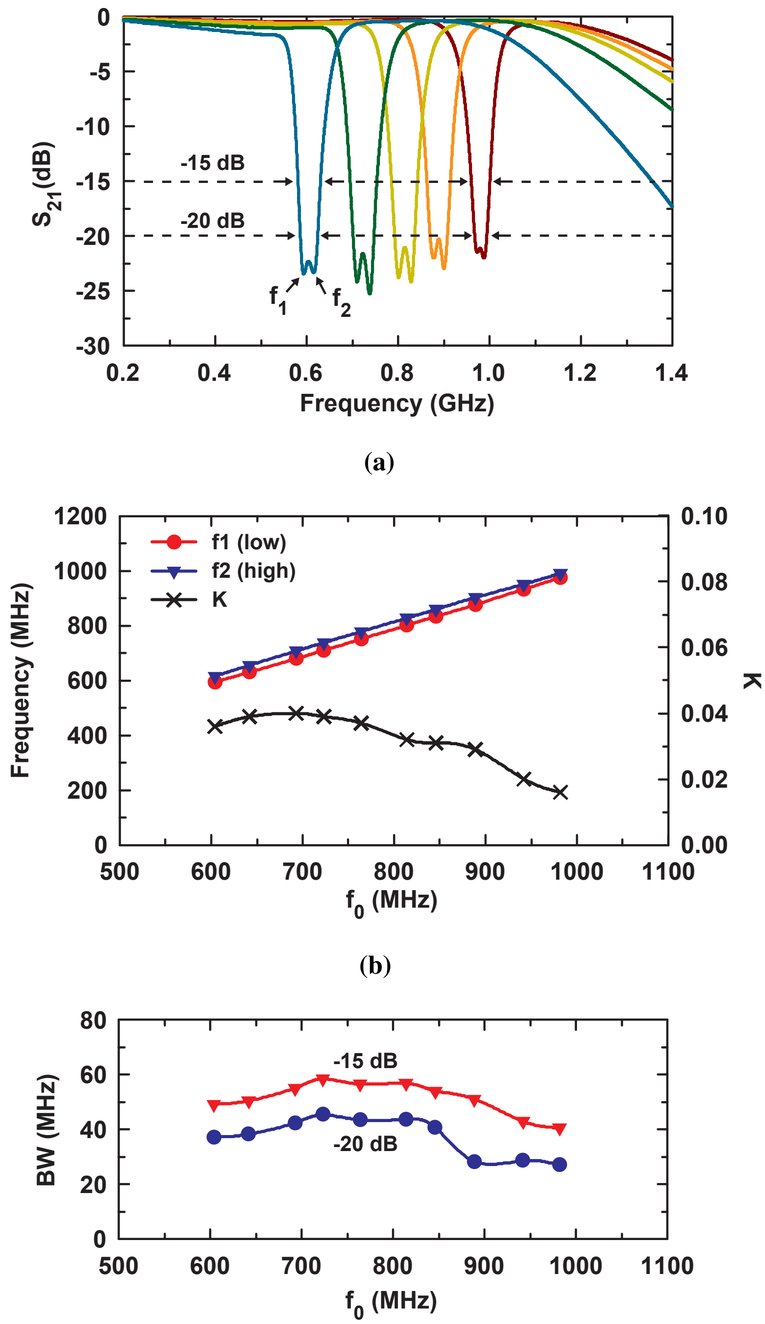

(a)

(b)

(c)

Figure 5.14: (a) Measured S_{21}, (b) f_1, f_2 and K v.s. f_0 and (c) 15-dB and 20-dB rejection bandwidth vs f_0 of the tunable two-pole dual-band notch filter with air-coil transformers.

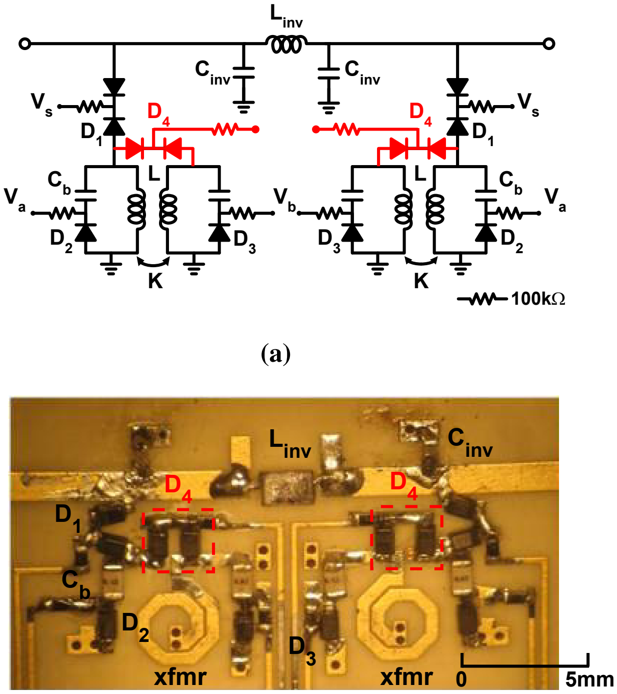

(a)

(b)

Figure 5.15: (a) Tunable two-pole dual-band notch filter with frequency separation tuning and (b) photo of the completed PCB filter.

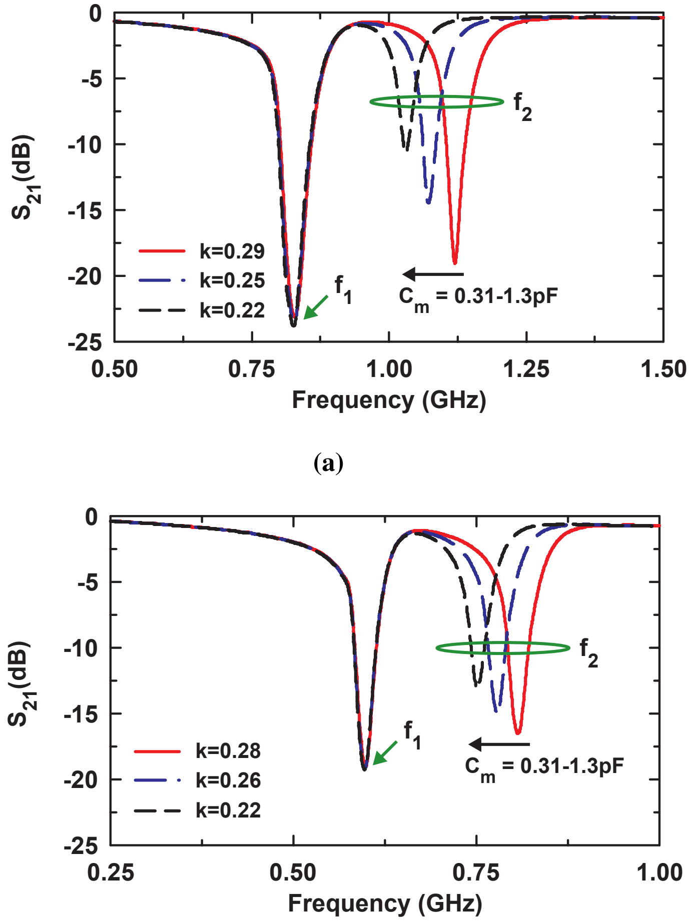

(a)

(b)

Figure 5.16: Measured frequency separation tuning : (a) f_1 = 830 MHz and (b) f_1 = 600 MHz.

5.6 Acknowledgment

The authors would like to thank Coilcraft Inc. for inductor samples and Rogers Corporation for providing the substrates.

Chapter 5 is based on and mostly a reprint of the following paper: CH. Ko, A. Tran, and G. M. Rebeiz, "Tunable 500-1200 MHz Dual-band and Wide Bandwidth Notch Filters with RF Transformers," submitted for publication in *IEEE Trans. Microw. Theory Tech.*, Aug. 2014.

Chapter 6

Conclusion

6.1 Summary of Work

This thesis presents a 4-element phase array implemented with reflective phase shifters using commercially packaged RF MEMS switches, an asymmetric 4-pole tunable filter using commercial RF MEMS varactors, the idea of reconfigurable matching networks for tunable diplexers, and tunable duanband bandstop filters with RF transformers.

Chapter 2 presents a passive-scanned linear phased array, using commercially available packaged RF MEMS switches for the tuning element. The presented measurements of high reliability, high power handling capabilities, and low loss properties insure that this design is an ideal candidate for base-station implementations in commercial and defense communications systems.

Chapter 3 has demonstrated a 1.7-2.5 GHz asymmetric 4-pole tunable filter with high linearity and high power handling using the Cavendish Kinetics RF MEMS capacitors. The filter can meet the linearity, ACPR and harmonic specifications of modern multi-band wireless front-ends. The asymmetric structure improves the passband flatness of a tunable filter. In addition, a RF MEMS varactor with capacitance step of 20-40 fF is recommended for 1.5-2.5 GHz tunable filter application. Finally, the effect of ENIG is explained and demonstrated and using a solder mask to prevent additional loss from metal finish is suggested.

Chapter 4 investigates and demonstrates the idea of a tunable diplexer with reconfigurable matching networks. In this design, the filter out of band impedance can be transformed from a short circuit into an open circuit. This leads to a tunable diplexer without any complicated design process. In addition, by using high-Q components, such as RF MEMS varactors and placing transmission zeroes at both side of a filter, the frequency separation and isolation between the two bands can be further improved.

Chapter 5 presents a tunable dual-band bandstop filter with RF transformers. Based on different coupling of a transformer, tunable dual-band notch filters or tunable single-band notch filters with wide rejection bandwidth can be achieved. The design procedure is also provided. In the future, using RF MEMS devices, the better frequency responses and higher linearity and power handling can be achieved.

6.2 Future Work

For the reflective phase shifters, the RF MEMS switches have a little bit higher parasitics so that the phase can not shift more after 123°. With better and smaller MEMS switches, the performance of the phase shifter can be further improved and provide wider scan angle for the phase array.

After the series RF MEMS varactors are commercially available, the bandpass filters can have much better performance. The filters can be designed to have fixed absolute bandwidth across the tuning range and tunable transmission zeros with series RF MEMS varactors while keeping low loss, high linearity and good power handling.

The reconfigurable matching networks and dualband bandstop filters can achieve higher performance by using RF MEMS varactors. The reconfigurable matching networks can also be applied for other applications, such as the input matching for low-noise amplifiers (LNAs) and the output matching for power amplifiers (PAs). The idea of using RF transformers to generate two coupled resonant frequencies can be used for bandpass filters too. In addition, these two ideas can be implemented into integrated circuits (ICs) to be combined with RF active circuits to enhance the performance while keeping overall circuit area small.

Bibliography

[1] Sonnet Software, North Syracuse, NY.

[2] 3GPP, http://www.3gpp.org/.

[3] A. Tombak, J. P. Maria, F. T. Ayguavives, J. Zhang, G. T. Stauf, A. I. Kingon, and A. Mortazawi, “Voltage-controlled rf filters employing thin-film bariumąvstrontiumąvtitanate tunable capacitors,” *IEEE Trans. Microw. Theory Tech.*, vol. 51, no. 2, pp. 462–467, Feb. 2003.

[4] C. Lugo and J. R. J. Papapolymerou, “Six-state reconfigurable filter structure for antenna based system,” *IEEE Trans. Antennas Propag.*, vol. 54, no. 2, pp. 479–483, Feb. 2006.

[5] Q. F. Q. X. X. Huang, L. Zhu and D. Jia, “Tunable bandpass filter with independently controllable dual passbands,” *IEEE Trans. Microw. Theory Tech.*, vol. 61, no. 9, pp. 3200–3208, Sep. 2013.

[6] Y. Cho and G. M. Rebeiz, “0.73-1.03-ghz tunable bandpass filter with a reconfigurable 2/3/4-pole response,” *IEEE Trans. Microw. Theory Tech.*, vol. 62, no. 2, pp. 290–296, Feb. 2014.

[7] H. Lee and G. M. Rebeiz, “A 640-1030 mhz four-pole tunable filter with improved stopband rejection and controllable bandwidth and transmission zeros,” in *IEEE MTT-S International Microwave Symposium*, Seattle, WA, Jun. 2013.

[8] Y. Chiou and G. M. Rebeiz, “Tuanble 1.55-2.1 ghz 4-pole elliptic bandpass filter with bandwidth control and $>$ 50 db rejection for wireless systems,” *IEEE Trans. Microw. Theory Tech.*, vol. 61, no. 1, pp. 117–124, Jan. 2013.

[9] Y. J. G. Chaudhary and J. Lim, “Dual-band bandpass filter with independently tunable center frequencies and bandwidths,” *IEEE Trans. Microw. Theory Tech.*, vol. 61, no. 1, pp. 107–116, Jan. 2013.

[10] J. Ni and J. Hong, “Compact varactor-tuned microstrip high-pass filter with a quasi-elliptic function response,” *IEEE Trans. Microw. Theory Tech.*, vol. 61, no. 11, pp. 3853–3859, Nov. 2013.

[11] M. Sanchez-Renedo, “High-selectivity tunable planar combline filter with source/load-multiresonators coupling,” *IEEE Microw. Wireless Compon. Lett.*, vol. 17, no. 7, pp. 513–515, Jul. 2007.

[12] J. Sun, N. Kaneda, Y. Baeyens, T. Itoh, and Y. Chen, “Multilayer planar tunable filter with very wide tuning bandwidth,” *IEEE Trans. Microw. Theory Tech.*, vol. 59, no. 11, pp. 2864–2871, Nov. 2011.

[13] Q. Xiang, Q. Feng, X. Huang, and D. Jia, “Electrical tuanble microstrip lc bandpass filters with constant bandwidth,” *IEEE Trans. Microw. Theory Tech.*, vol. 61, no. 3, pp. 1124–1130, Mar. 2013.

[14] G. M. R. *et al.*, “Tuning in to RF MEMS,” *IEEE Microw. Mag.*, vol. 10, no. 5, pp. 55–71, Oct. 2009.

[15] C. C. Cheng and G. M. Rebeiz, “High-q 4-6-ghz suspended stripline RF MEMS tunable filter with bandwidth control,” *IEEE Trans. Microw. Theory Tech.*, vol. 59, no. 10, pp. 2469–2476, Oct. 2011.

[16] M. A. El-Tanani and G. M. Rebeiz, “High performance 1.5-2.5-ghz RF MEMS tunable filters for wireless applications,” *IEEE Trans. Microw. Theory Tech.*, vol. 58, no. 6, pp. 1629–1637, Jun. 2010.

[17] S. J. Park, I. Reines, C. Patel, and G. M. Rebeiz, “High-Q RF-MEMS 4-6-ghz tunable evanescent-mode cavity filter,” *IEEE Trans. Microw. Theory Tech.*, vol. 58, no. 2, pp. 381–389, Feb. 2010.

[18] X. Liu, L. P. B. Katehi, W. J. Chappell, and D. Peroulis, “High-Q tunable microwave cavity resonators and filters using SOI-based RF MEMS tuners,” *J. Microelectromech. Syst.*, vol. 19, no. 4, pp. 774–784, Aug. 2010.

[19] S. Fouladi, F. Huang, W. D. Yan, and R. R. Mansour, “High-Q narrowband tunable combline bandpass filters using MEMS capacitor banks and piezomotors,” *IEEE Trans. Microw. Theory Tech.*, vol. 61, no. 1, pp. 2399–2405, Jan. 2013.

[20] W. Yan and R. R. Mansour, “Tunable dielectric resonator bandpass filter with embedded MEMS tuning elements,” *IEEE Trans. Microw. Theory Tech.*, vol. 55, no. 1, pp. 154–160, Jan. 2007.

[21] J. Small, M. S. Arif, A. Fruehling, and D. Peroulis, “A tunable miniatureized RF MEMS resonator with simultaneous high q (500-735) and fast response speed ($<$ 10-60 μs),” *J. Microelectromech. Syst.*, vol. 22, no. 2, pp. 395–405, Apr. 2013.

[22] Y. Shim, Z. Wu, and M. Rais-Zadeh, “A high-performance continuously tunable MEMS bandpass filter at 1 ghz,” *IEEE Trans. Microw. Theory Tech.*, vol. 60, no. 8, pp. 2439–2447, Aug. 2012.

[23] Omron Corp., Kyoto, Japan.

[24] Radant MEMS, Stow, MA.

[25] wiSpry Inc., Irvine, CA.

[26] Cavendish Kinetics Inc., San Jose, CA.

[27] G. M. Rebeiz, G. L. Tan, and J. S. Hayden, “RF MEMS phase shifters: design and applications,” *IEEE Microw. Mag.*, vol. 3, no. 2, pp. 72–81, Jun. 2002.

[28] A. Malczewski, S. Eshelman, B. Pillans, J. Ehmke, and C. L. Goldsmith, “X-band RF MEMS phase shifters for phased array applications,” *IEEE Microw. Guided Wave Lett.*, vol. 9, no. 12, pp. 517–519, Dec. 1999.

[29] B. Pillans, L. Coryell, A. Malczewski, C. Moody, F. Morris, and A. Brown, “Advances in RF MEMS phase shifters from 15 GHz to 35 GHz,” in *IEEE MTT-S International Microwave Symposium*, Montreal, Canada, Jun. 2012.

[30] C. C. Cheng, C. H. Ko, A. Morris, and G. M. Rebeiz, “A very low loss 1.9-2.1 GHz RF MEMS phase shifter,” in *IEEE MTT-S International Microwave Symposium*, Montreal, Canada, Jun. 2012.

[31] J. B. Rizk and G. M. Rebeiz, “W-band CPW RF MEMS circuits on quartz substrates,” *IEEE Trans. Microw. Theory Tech.*, vol. 51, no. 7, pp. 1857–1862, Jul. 2003.

[32] G. L. Tan, R. E. Mihailovich, M. Kim, J. F. DeNatale, and G. M. Rebeiz, “A very-low-loss 2-bit X-band RF MEMS phase shifters based on SP4T switches,” in *IEEE MTT-S International Microwave Symposium*, Seattle, WA, Jun. 2002, pp. 333–335.

[33] J. Lampen, S. Majumder, C. Ji, and J. Maciel, “Low-loss, MEMS based, broadband phase shifters,” in *IEEE International Symp. on Phased Array Systems and Technology*, Oct. 2010, pp. 219–227.

[34] G. L. Tan, R. E. Mihailovich, J. B. Hacker, J. F. DeNatale, and G. M. Rebeiz, “Low-loss 2- and 4-bit TTD MEMS phase shifters based on SP4T switches,” *IEEE Trans. Microw. Theory Tech.(Special Issue on RF MEMS)*, vol. 51, no. 1, pp. 297–304, Jan. 2003.

[35] C. D. Nordquist, C. W. Dyck, G. M. Kraus, I. C. Reines, C. L. Goldsmith, W. D. Cowan, T. A. Plut, F. Austin IV, P. S. Finnegan, M. H. Ballance, and C. T. Sullivan, “A DC to 10-GHz 6-b RF MEMS time delay circuit,” *IEEE Microw. Wireless Compon. Lett.*, vol. 16, no. 5, pp. 305–307, May 2006.

[36] B. Pillans, S. Eshelman, A. Malczewski, J. Ehmke, and C. Goldsmith, “Ka-band RF MEMS phase shifters,” *IEEE Microw. Guided Wave Lett.*, vol. 9, no. 12, pp. 520–522, Dec. 1999.

[37] N. S. Barker and G. M. Rebeiz, "Optimization of distributed MEMS transmission-line phase shifters U-band and W-band designs," *IEEE Trans. Microw. Theory Tech.*, vol. 48, no. 11, pp. 1957–1966, Nov. 2000.

[38] J. J. Hung, L. Dussopt, and G. M. Rebeiz, "2-bit and 3-bit W-band RF MEMS phase shifters," *IEEE Trans. Microw. Theory Tech.*, vol. 52, no. 2, pp. 600–606, Feb. 2004.

[39] N. Somjit, G. Stemme, and J. Oberhammer, "Binary-coded 4.25-bit W-band monocrystalline-silicon MEMS multistage dielectric-block phase shifters," *IEEE Trans. Microw. Theory Tech.*, vol. 57, no. 11, pp. 2834–2840, Nov. 2009.

[40] G. McFeetors and M. Okoniewski, "Distributed MEMS analog phase shifter with enhanced tuning," *IEEE Microw. Wireless Compon. Lett.*, vol. 16, no. 1, pp. 34–36, Jan. 2006.

[41] Atm microwave phase shifter. [Online]. Available: http://www.atmmicrowave.com/coax-phase.html

[42] Aeroflex phase shifter. [Online]. Available: http://www.aeroflex.com/ams/weinschel/micro-weinschel-prods-MPS.cfm

[43] M. El-Tanani and G. M. Rebeiz, "C-band low-loss $> 360^o$ phase shifter for WLAN applications," in *European Microwave Conference*, Oct. 2007, pp. 1503–1506.

[44] Modelithics, Tampa, FL.

[45] Agilent Technologies, Santa Clara, CA.

[46] R. A. Alhalabi and G. M. Rebeiz, "High-efficiency angled-dipole antennas for millimeter-wave phased array applications," *IEEE Trans. Antennas Propag.*, vol. 52, no. 10, pp. 3136–3142, Oct. 2008.

[47] Ansoft Corp., Pittsburgh, PA.

[48] K. J. Koh and G. M. Rebeiz, "0.13-μm cmos phase shifters for x-, ku-, and k-band phased arrays," *IEEE J. Solid-State Circuits*, vol. 42, no. 11, pp. 2535–2546, Nov. 2007.

[49] SATIMO Corp., France.

[50] G. M. Rebeiz, *RF MEMS Theory, Design, and Technology*. New York: Wiley, 2003.

[51] V. J. *et al.*, "MEMS solutions in RF applications," in *IEEE SOI-3D-Subthreshold Microelectronics Technology Unified Conference (S3S)*, Monterey, CA, Oct. 2013.

[52] J. Hong and M. J. Lancaster, *Microstrip Filters for RF/Microwave Applications*. New York: John Wiley & Sons, 2001.

[53] Y. Chiou and G. M. Rebeiz, "A quasi-elliptic function 1.75-2.25 ghz 3-pole bandpass filter with bandwidth control," *IEEE Trans. Microw. Theory Tech.*, vol. 60, no. 2, pp. 244–249, Feb. 2012.

[54] M. A. El-Tanani and G. M. Rebeiz, "A two-pole two-zero tunable filter with improved linearity," *IEEE Trans. Microw. Theory Tech.*, vol. 57, no. 4, pp. 830–839, Apr. 2009.

[55] IPC-4452 standard, (http://www.ipc.org/TOC/IPC-4552.pdf).

[56] C. S. Yoo, J. K. Lee, D. Kim, S. E. Park, K. H. Won, N. K. Kaung, K. S. Seo, and W. S. Lee, "Rf front-end passive circuit implementation including antenna for zigbee applications," *IEEE Trans. Microw. Theory Tech.*, vol. 55, no. 5, pp. 906–915, May 2007.

[57] X. C. Hong, H. L. Peng, and J. F. Mao, "An antenna switch module for gsm application using ltcc technology," in *Int. Conf. Micro. mm-Wave Techn.*, Chengdu, China, May 2010, pp. 1457–1460.

[58] Y. S. Dai, S. L. Xiao, S. B. Chen, B. Q. Dai, L. J. Wang, C. Z. L. Xu, Q. S. Yu, H. Zhang, J. Yang, and X. Chen, "Design on antenna switch module for dual band phone (GSM/UMTS) using ltcc technology," in *Proc. Signals, Syst. Elec.*, Nanjing, China, Sep. 2010.

[59] K. M. J. Ho and G. M. Rebeiz, "A 0.9-1.5 ghz microstrip antenna with full polarization diversity and frequency agility," *IEEE Trans. Antennas Propag.*, vol. 62, no. 5, pp. 2398–2406, May 2014.

[60] S. Genovesi, A. D. Candia, and A. Monorchio, "Compact and low profile frequency agile antenna for multistandard wireless communication systems," *IEEE Trans. Antennas Propag.*, vol. 62, no. 3, pp. 1019–1026, Mar. 2014.

[61] Y. H. Cho and G. M. Rebeiz, "0.73-1.03-ghz tunable bandpass filter with a reconfigurable $2/3/4$-pole response," *IEEE Trans. Microw. Theory Tech.*, vol. 62, no. 2, pp. 290–296, Feb. 2014.

[62] J. R. Mao, W. W. Choi, K. W. Tam, W. Q. Che, and Q. Xue, "Tunable bandpass filter design based on external quality factor tuning and multiple mode resonators for wideband applications," *IEEE Trans. Microw. Theory Tech.*, vol. 61, no. 7, pp. 2574–2584, Jul. 2013.

[63] L. Gao, X. Y. Zhang, B. J. Hu, and Q. Xue, "Novel multi-stub loaded resonators and their applications to various bandpass filters," *IEEE Trans. Microw. Theory Tech.*, vol. 62, no. 5, pp. 1162–1172, May 2014.

[64] G. Matthaei, L. Young, and E. T. Jones, *Microwave Filters Impedance-Matching Networks, and Coupling Structures*. Norwood, MA: Artech House, 1980.

[65] K. Saitou and K. Kageyama, "Tunable duplexer having multilayer structure using ltcc," in *IEEE MTT-S International Microwave Symposium*, Philadelphia, PA, Jun. 2003, pp. 1763–1766.

[66] K. Kawai, H. Okazaki, and S. Narahashi, "Tunable ring resonator filter for duplexer," in *European Microwave Conference*, Oct. 2008.

[67] E. E. Djoumessi and K. Wu, "Electronically tunable diplexer for frequency-agile transceiver front-end," in *IEEE MTT-S International Microwave Symposium*, Anaheim, CA, Jun. 2010, pp. 1472–1775.

[68] T. Yang and G. M. Gabriel, "Three-pole 1.3-2.4 ghz diplexer and 1.1-2.45 ghz dual-band filter with common resonator topology and flexible tuning capabilities," *IEEE Trans. Microw. Theory Tech.*, vol. 61, no. 10, pp. 3613–3624, Oct. 2013.

[69] D. M. Pozar, *Microwave Engineering*, 4th ed. New York: John Wiley & Sons, 2011.

[70] T. Yang and G. M. Gabriel, "Striplline 3-pole notch filter and tunable 3-pole bandpss/bandstop filters with dynamically tunable bandwidth and notch," *Submitted to IEEE Trans. Microw. Theory Tech.*

[71] Skyworks Solutions Inc., Woburn, MA.

[72] Coilcraft Inc., Cary, IL.

[73] American Technical Ceramic Corp., Huntington Station, NY.

[74] Y. H. Cho and G. M. Rebeiz, "Two- and four-pole tunable 0.7-1.1-ghz bandpass-to-bandstop filters with bandwidth control," *IEEE Trans. Microw. Theory Tech.*, vol. 62, no. 3, pp. 457–463, Mar. 2014.

[75] Y. C. Ou and G. M. Rebeiz, "Lumped-element fully tunable bandstop filters for cognitive radio applications," *IEEE Trans. Microw. Theory Tech.*, vol. 59, no. 10, pp. 2461–2468, Oct. 2011.

[76] D. R. Jachowski, "Octave tunable lumped-element notch filter," in *IEEE MTT-S International Microwave Symposium*, Montreal, QC, Canada, Jun. 2012.

[77] S. Y. Huang and Y. H. Lee, "A compact e-shaped patterned ground structure and its applications to tunable bandstop resonator," *IEEE Trans. Microw. Theory Tech.*, vol. 57, no. 3, pp. 657–666, Mar. 2009.

[78] X. H. Wang, B. Z. Wang, H. Zhang, and K. J. Chen, “A tunable bandstop resonator based on a compact slotted ground structure,” *IEEE Trans. Microw. Theory Tech.*, vol. 55, no. 9, pp. 1912–1918, Sep. 2007.

[79] C. C. Cheng and G. M. Rebeiz, “A three-pole 1.2-2.6-ghz RF MEMS tunable notch filter with 40-db rejection and bandwidth control,” *IEEE Trans. Microw. Theory Tech.*, vol. 60, no. 8, pp. 2431–2438, Aug. 2012.

[80] E. J. Naglich, J. Lee, D. Peroulis, and W. J. Chappell, “Extended passband bandstop filter cascade with continuous 0.85-6.6-ghz coverage,” *IEEE Trans. Microw. Theory Tech.*, vol. 60, no. 1, pp. 21–30, Jan. 2012.

[81] X. Liu, E. Naglich, and D. Peroulis, “Non-linear effects in MEMS tunable bandstop filters,” in *IEEE MTT-S International Microwave Symposium*, Montreal, QC, Canada, Jun. 2012.

[82] I. Reines, S. J. Park, and G. M. Rebeiz, “Compact low-loss tunable x-band bandstop filter with miniature RF-MEMS switches,” *IEEE Trans. Microw. Theory Tech.*, vol. 58, no. 7, pp. 1887–1895, Jul. 2012.

[83] T. Snow, J. Lee, and W. J. Chappell, “Tunable high quality-factor absorptive bandstop filter design,” in *IEEE MTT-S International Microwave Symposium*, Montreal, QC, Canada, Jun. 2012.

[84] E. J. Naglich, J. Lee, and D. Peroulis, “Tunable bandstop filter with a 17-to-1 upper passband,” in *IEEE MTT-S International Microwave Symposium*, Montreal, QC, Canada, Jun. 2012.

[85] C. H. Tseng and T. Itoh, “Dual-band bandpass and bandstop filters using composite right/left-handed metamaterial transmission lines,” in *IEEE MTT-S International Microwave Symposium*, San Francisco, CA, Jun. 2006, pp. 931–934.

[86] S. Saxena, S. Porwal, K. Soni, P. Chhawchharia, and S. K. Koul, “Analysis and design of bandstop filter using e-shaped dual mode resonator,” in *Proc. of Micro. Comm. Ant. and Elec. Sys. Conference*, Nov. 2009.

[87] A. B. Guntupalli and S. Sanyal, “Compact high performance microstrip dual-band bandstop filters for GSM mobile bands,” in *Proc. of Elect. Interferenc & Compatibility Conference*, Nov. 2008.

[88] A. B. Guntupalli, V. K. Velidi, and S. Sanyal, “Compact dual wide bandstop filter,” in *Proc. of Applied Electromagnetics Conference*, Dec. 2009.

[89] Z. Ma, K. Kikuchi, Y. Kobayashi, T. Anada, and G. Hagiwara, “Novel microstrip dual-band bandstop filter with controllable dual-stopband response,” in *Proc. of Asia-Pacific Microwave Conference*, Dec. 2006, pp. 1174–1177.

[90] Y. Luo and Q. Chu, “A compact high selectivity dual-band bandstop filter using bent l-resonators,” in *European Microwave Conference*, Oct. 2013, pp. 25–28.

[91] Y. Y. Wang, F. Wei, H. Xu, B. Liu, and X. W. Shi, “A tunable dual-stop-band filter using spurlines,” in *Proc. of the Micro. mm-Wave Tech. Conference*, Shenzhen, May 2012.